OPTIMIZATION AND CHARACTERIZATION OF POLYSILICON FABRICATED BY E-BEAM EVAPORATION FOR PASSIVATING CONTACT SILICON (TOPCON) SOLAR CELLS

A THESIS SUBMITTED TO
THE GRADUATE SCHOOL OF NATURAL AND APPLIED SCIENCES
OF
MIDDLE EAST TECHNICAL UNIVERSITY

BY

SALAR HABIBPUR SEDANI

IN PARTIAL FULFILLMENT OF THE REQUIREMENTS
FOR
THE DEGREE OF DOCTOR OF PHILOSOPHY
IN
MICRO AND NANOTECHNOLOGY

SEPTEMBER 2022

Approval of the thesis:

OPTIMIZATION AND CHARACTERIZATION OF POLYSILICON FABRICATED BY E-BEAM EVAPORATION FOR PASSIVATING CONTACT SILICON (TOPCON) SOLAR CELLS

submitted by **SALAR HABIBPUR SEDANI** in partial fulfillment of the requirements for the degree of **Doctor of Philosophy** i**n Micro and Nanotechnology, Middle East Technical University** by,

Prof. Dr. Halil Kalıpçılar
Dean, Graduate School of **Natural and Applied Sciences**

Prof. Dr. Deniz Üner
Head of the Department, **Micro and Nanotechnology**

Prof. Dr. Raşit Turan
Supervisor, **Micro and Nanotechnology, METU**

Prof. Dr. Hüsnü Emrah Ünalan
Co-Supervisor, **Metallurgical & Materials Eng, METU**

Examining Committee Members:

Prof. Dr. Mehmet Parlak
Physics Dep., METU

Prof. Dr. Raşit Turan
Micro and Nanotechnology, METU

Assoc. Prof. Dr. Mustafa Kulakci
Physics Dep., Eskişehir Tech. Uni.

Assoc. Prof. Dr. Selçuk Yerci
Electric and Electronic Eng., METU

Assoc. Prof. Emre Erdem
Materials Science and Nano Eng., Sabancı Uni.

Date: 05.09.2022

I hereby declare that all information in this document has been obtained and presented in accordance with academic rules and ethical conduct. I also declare that, as required by these rules and conduct, I have fully cited and referenced all material and results that are not original to this work.

Name Last name : Salar Habibpur Sedani

Signature :

ABSTRACT

OPTIMIZATION AND CHARACTERIZATION OF POLYSILICON FABRICATED BY E-BEAM EVAPORATION FOR PASSIVATING CONTACT SILICON (TOPCON) SOLAR CELLS

Sedani, Salar Habibpur
Doctor of Philosophy, Micro and Nanotechnology
Supervisor : Prof. Dr. Raşit Turan
Co-Supervisor: Prof. Dr. Hüsnü Emrah Ünalan

September 2022, 132 pages

Carrier selective passivating contacts have permitted higher conversion efficiencies by decreasing minority carrier recombination velocities at c-Si/metal contact surfaces. Pioneers of photovoltaics (PV) are investigating the remarkable passivation properties of doped polysilicon (poly-Si) layers over silicon oxide (SiO_x). Photovoltaic industry experts are predicting a bright future for poly-Si/SiO_x structures (TOPCon), as the future of the PV industry. It is possible to minimize the cost of poly-Si layer deposition by using e-beam evaporation equipped with effusion cells (e-Beam EC), even if Chemical Vapor Deposition (CVD) methods such as plasma-enhanced chemical vapor deposition (PECVD) and low-pressure chemical vapor deposition (LPCVD) are available. The e-beam EC technology also eliminates the use of hazardous process gases, such as PH_3 and B_2H_6, from the manufacturing process.

Passivating contact applications were investigated using e-beam-deposited p-type a-Si layers, while low temperature PECVD was used to deposit the n-type a-Si layer on the opposite side. We investigate the impact of boron and phosphorous dopant crystallization temperatures on doping activation. This layer of p-a-Si, which is non-hydrogenated, is ideal for low temperature activation of boron doping in the absence of boron-hydrogen complexes. Ultimately, blister-free p-poly and n-poly layers develop concurrently on both sides of the cell. Additional hydrogenation steps and ITO deposition heal the defects of the non-hydrogenated passivating contacts. As a result of this study, we fabricate bifacial TOPCon cells which reach an efficiency of 17.7% on the p-poly side and 20.2% on the n-poly side.

Keywords: Passivating Contact Solar Cells (TOPCon), e-Beam Evaporation with Effusion Cell (e-Beam EC), PECVD, Polysilicon Defects, Crystallization

ÖZ

PASİFLEŞTİREN KONTAKLI SİLİSYUM TABANLI GÜNEŞ HÜCRESİ (TOPCON) UYGULAMALARI İÇİN ELEKTRON DEMETİ İLE ÜRETİLMİŞ POLİSİLİSYUM YAPILARIN OPTİMİZASYONU VE KARAKTERİZASYONU

Sedani, Salar Habibpur
Doktora, Mikro ve Nanoteknoloji
Tez Yöneticisi: Prof. Dr. Raşit Turan
Ortak Tez Yöneticisi: Prof. Dr. Hüsnü Emrah Ünalan

Eylül 2022, 132 sayfa

Taşıyıcı seçici pasifleştirme kontakları, c-Si/metal temas yüzeylerinde azınlık taşıyıcı rekombinasyon hızlarını azaltarak daha yüksek dönüşüm verimliliğine izin vermmektedir. Fotovoltaik öncüleri, katkılı polisilikon (poli-Si) katmanların silikon oksit (SiO_x) üzerindeki olağanüstü pasifleştirme özelliklerini araştırıyorlar. Fotovoltaik endüstrisi uzmanları, PV endüstrisinin geleceği olarak poli-Si/SiO_x yapıları (TOPCon) için parlak bir gelecek öngörüyor plasma-enhanced chemical vapor deposition (PECVD) ve low-pressure chemical vapor deposition (LPCVD) gibi CVD yöntemleri mevcut olsa bile, efüzyon hücreleri ile donatılmış elektron demet buharlaştırma (e-Beam EC) sistemini kullanarak poli-Si tabaka üretimi yanı sıra üretim maliyetini en aza indirmek mümkündür. E-demet teknolojisi, üretim sürecinden PH_3 ve B_2H_6 gibi tehlikeli proses gazlarının kullanımını da ortadan kaldırır. Pasifleştirme temas uygulamaları, e-Beam EC üretilmiş p-tipi a-Si katmanları kullanılarak araştırılırken, n-tipi a-Si katmanını hücrenin diğer tarafında büyütmek için düşük sıcaklıkta PECVD kullanıldı. Bor ve fosfor katkılı kristalizasyon sıcaklıklarının doping aktivasyonu üzerindeki etkisini araştırılmıştır.

Fazladan Hidrojene eklenmeyen bu p-a-Si tabakası, boron-hidrojen komplekslerinin yokluğunda boron katkılamanın düşük sıcaklıkta aktivasyonu için idealdir. Sonuçta, hücrenin her iki tarafında aynı anda döküntüsüz p-poli ve n-poli katmanları geliştirilmiştir. Ek hidrojenlendirme adımları ve ITO büyütme, hidrojenlendirilmeyen pasifleştirici kontakların kusurlarını iyileştirir. Bu çalışma sonucunda p-poly tarafında %17.7, n-poly tarafında %20.2 verimliliğe ulaşan çift taraflı TOPCon hücreleri üretilmiştir.

Anahtar Kelimeler: Pasifleştiren Kontakli Güneş Hücresi (TOPCon), Efüzyon Hücre destekli e-Demeti Buharlaştırma (e-Beam EC), PECVD, Polisilisyum Kusurları, Kristallendirme

Dedicated to Yunes, Faeqe, Homayoon, Mahsa,
Fatma Sultan & Alireza, and to whom believe in Great Expectations

ACKNOWLEDGMENTS

The author wishes to express his deepest gratitude to his supervisor Prof. Dr. Raşit Turan and co-supervisor Prof. Dr. Hüsnü Emrah Ünalan for their guidance, advice, criticism, encouragements and insight throughout the research.

The author would also like to thank Assoc. Prof. Dr. Selçuk Yerci and Assoc. Prof. Dr. Mustafa Kulakcı as my Thesis Monitoring Committee for their guidance through this investigation. Also, I should thank Prof. Dr. Mehmet Parlak and Assist. Prof. Dr. Emre Erdem for his suggestions, comments and helps though my graduate studies.

The scientific assistance of Dr. E. Hande Çiftpınar, Dr. Ergi Dönerçark, Dr. İlker Yıldız, Dr. Mehmet Karaman, Assist. Prof. Özlen F. Yaşar, Assist. Prof. Özge Tüzün Özmen, Prof. Dr. Atilla Aydınlı, Assoc. Prof. Dr. Alpan Bek and Prof. Dr. Christiane Beker are gratefully acknowledged.

The non-stop motivation and support of Dr. Mona Borra and Dr. Behzad Hosseini are appreciated, heartfully. Furthermore, I would thank Dr. Hisham Nasser, Seda Kılıçkaya, Duygu Kuzyaka and Dr. Mustafa Ünal.

This work is partially funded by Center for Solar Energy Research and Application (ODTÜ-GÜNAM).

TABLE OF CONTENTS

CHAPTERS

LIST OF TABLES

TABLES

LIST OF FIGURES

FIGURES

LIST OF ABBREVIATIONS

Al BSF (Back Surface Field)

HIT (Heterojunction with Intrinsic Thin Layer)

IBC (Interdigitated Back Contact)

PERC (Passivated Emitter and Rear Contact)

TOPCon (Tunnel Oxide Passivated Contact)

POLO (Polysilicon on Oxide)

Polysilicon (poly-Si)

Heterojunction Back Contact (HBC)

Solar Energy Research in Hamelin (ISFH)

POLO junctions for both polarities (POLO)^2

capital expenditure (CAPEX)

Silicon heterojunction (SHJ)

International Technology Roadmap for Photovoltaic (ITRPV)

Chemical Vapor Deposition (CVD)

Low-Pressure Chemical Vapor Deposition (LPCVD)

Plasma-Enhanced Chemical Vapor Deposition (PECVD)

PhysicalVapor Deposition (PVD)

Standard Test Conditions (STC)

Light-Induced Degradation (LID)

Light and elevated temperature-induced degradation (LeTID)

Levelized cost of energy (LCOE)

Atomic layer deposition (ALD)

Anti-reflection coating (ARC)

Maximum power point (MPP)

Open-circuit (OC)

Double-layer anti-reflection coatings (DARC)

Free energy loss analysis (FELA)

Electron beam evaporation (e-beam)

Electron beam evaporator equipped with effusion cells (e-Beam EC)

Transparent conductive oxide (TCO)

LIST OF SYMBOLS

Silicon oxide (SiO_x)

Open-circuit voltage (V_{oc})

Silver (Ag)

Silicon dioxide layer (SiO_2)

Aluminum oxide (Al_2O_3)

Silicon nitride (SiN_x)

Implied open-circuit voltage (iV_{oc})

Recombination current density (J_0)

Fill factor (FF)

Implied fill factor (iFF)

Pseudo-FF (PFF)

Lifetime (τ_{eff})

Zinc oxide (ZNO)

Aluminum doped zinc oxide (AZO)

Indium doped tin oxide (ITO)

CHAPTER 1

INTRODUCTION

One of the most important discoveries in contemporary science is without a doubt the discovery of the solar photovoltaic effect, or the direct conversion of sunlight into energy [1]. Additionally, Bell Labs' successful production of the first genuine solar cell in 1954 was able to significantly support the research efforts for many investigations in the area of solar photovoltaics [2]. As a result, various solar cell structures based on different semiconductor materials have been developed, but standard Al BSF (Back Surface Field) crystalline silicon solar cells have dominated the market share for a longer time due to their many advantages, including their abundance of raw materials, accessibility to simple fabrication technologies, high throughput, minimal maintenance, and low operating costs [3,4]. The efficiency potential of this structure is, however, constrained by two significant drawbacks, notably high back surface recombination velocities at p-p+ interface and low back surface reflectance [4,5]. In light of this, current research on crystalline silicon-based solar cells is solely focused on streamlining the manufacturing processes as well as increasing the power output of other high efficiency crystalline silicon-based solar cells, such as HIT (Heterojunction with Intrinsic Thin Layer) solar cells, IBC (Interdigitated Back Contact) solar cells, PERC (Passivated Emitter and Rear Contact) solar cells, and TOPCon (Tunnel Oxide Passivated Contact) solar The term "TOPCon" may conceptually also be shortened to "POLO" (Polysilicon on Oxide) [6].

Cost reduction in the crystalline silicon wafer production remigrate interests of photovoltaic community to the crystalline silicon-based solar cells. Some researchers used comparable polysilicon (poly-Si) connections to solar cells to boost open-circuit voltage (V_{oc}) after Yablonovitch's 1985 proposal that the ideal solar cell be "built in the shape of a double heterostructure," with the absorber sandwiched between two wide-gap materials with opposing doping [7]. As a result, a team of researchers from Germany [8] adopted Yablonovitch's strategy and developed TOPCon. A silicon layer that has been doped with phosphorus and a very thin tunnel oxide make up TOPCon [9]. It provides a straightforward processing strategy that works with high-temperature processes like diffusion.

Thus, it has been noted that the power conversion efficiency of these different crystalline silicon-based solar cells is constantly increasing. As an example, Kaneka reported about the creation of 25.1 percent HIT solar cells in 2015 [10] based on n-type CZ-Si wafers with an active cell area of 151.9 cm^2 (V_{oc} = 738 mV, J_{sc} = 40.8 mA/cm^2, and FF = 83.5 percent). SunPower, on the other hand, asserted a nearly same result for single junction IBC solar cells made on n-type CZ-Si wafers, with a conversion efficiency of 25.2 percent (V_{oc} = 737 mV, J_{sc} = 41.33 mA/cm^2, and FF = 82.7 percent) [11]. The matching cell was 153.49 cm^2 in size. However, the former displayed greater V_{oc} and FF due to the existence of an amorphous silicon layer that provided high-quality surface passivation, whilst the latter exhibited superior J_{sc} due to the absence of shading effect.

Sharp created the first HBC (Heterojunction Back Contact) solar cells in 2014 with a conversion efficiency of 25.1% [12] by incorporating the idea of interdigitated back contact with HIT solar cells. By using a similar idea, Panasonic created HBC solar cells, which at the time set the record for crystalline silicon-based solar cells with a conversion efficiency of 25.6 percent (V_{oc} = 740 mV, J_{sc} = 41.8 mA/cm^2, and FF = 82.7 %) [13]. The developed cells' active cell area was 143.7 cm^2. The achievement was short-lived, however, since Kaneka revealed in 2016 that 26.3 percent (V_{oc} = 744 mV, J_{sc} = 42.3 mA/cm^2, and FF = 83.8 percent) efficient HBC solar cells with an active cell area of 180.4 cm^2 had been developed [14]. The best cell had a conversion efficiency of 26.6 percent (V_{oc} = 740 mV, J_{sc} = 42.5 mA/cm^2 and FF = 84.6 %) with an active cell area of 179.7 cm^2 shortly after Kaneka further revealed an increase in the conversion efficiency of HBC solar cells [15]. A new record for HJT solar cells based on M6 wafers was just reported by LONGi Solar in October 2021 [16]. Contrarily, traditional PERC and TOPCon solar cells have been discovered to have the highest recorded efficiencies of 24.06 percent and 25.7 percent, respectively [17,18].

The renowned German solar energy research center, Institute for Solar Energy Research in Hamelin (ISFH), claimed in 2018 that it had created 26.1 percent efficient c-Si solar cells by integrating both p^+POLO and n^+POLO structures at the back side of a p-type c-Si wafer in an interdigitated (V_{oc} = 726.6 ± 1.8 mV, J_{sc} = 42.62 ± 0.4 mA/cm^2 and FF = 84.28 ± 0.59 %; active cell area of 4 cm^2) [19]. The passivated contacts, or n^+ and p^+POLO layers, were separated in the manufactured device by an intrinsic poly-Si layer. The important elements to achieving such a high efficiency rating were low parasitic absorption by the doped poly-Si layer owing to the presence of passivated connections at the rear side and no metal-induced shading losses at the front side of the cell. Additionally, they said that a laser ablation approach was utilized for contact opening rather of a photolithography procedure, which may make it easier to adopt a screen printing-based metallization technique throughout the cell construction process. Additionally, according to Peibst et al., simulation analysis with Quokka2.0., the power conversion efficiency of these POLO junctions for both polarities (POLO)^2 IBC solar cells built on conventional p-type, FZ c-Si wafers might reach up to 27.8 percent (without photonic crystals) or even 29.1 percent (with photonic crystals) [20]. However, before IBC solar cells with (POLO)^2 structure at the back are put into mass production, issues like the participation of time-consuming and costly processing processes, low throughput, etc. must be resolved. However, compared to PERC and TOPCon solar cells, which cost around RMB 150–200 million/GW and RMB 250 million/GW, respectively, the capital expenditure (CAPEX) for SHJ (Silicon heterojunction) solar cells is about RMB 400 million/GW [21]. The use of pricey low temperature treated silver paste and higher depreciation costs are additional major barriers to the widespread commercialization of SHJ solar cells.

The solar photovoltaics industry is exclusively controlled by cell designs with diffused and passivated p-n junctions and passivated rear sides (PERC/PERL/PERT/TOPCON), according to the International Technology Roadmap for Photovoltaic

(ITRPV) 2022 study. According to Figure 1.1, the market share of PERC/PERL/PERT/TOPCON in 2021 will be about 85%. This agrees with IHS Markit's predictions [22]. Over the next years, PERC/PERT/PERL/TOPCON will rule the market. After 2024, SHJ cells are anticipated to have a market share of around 10% and close to 20% by 2032.

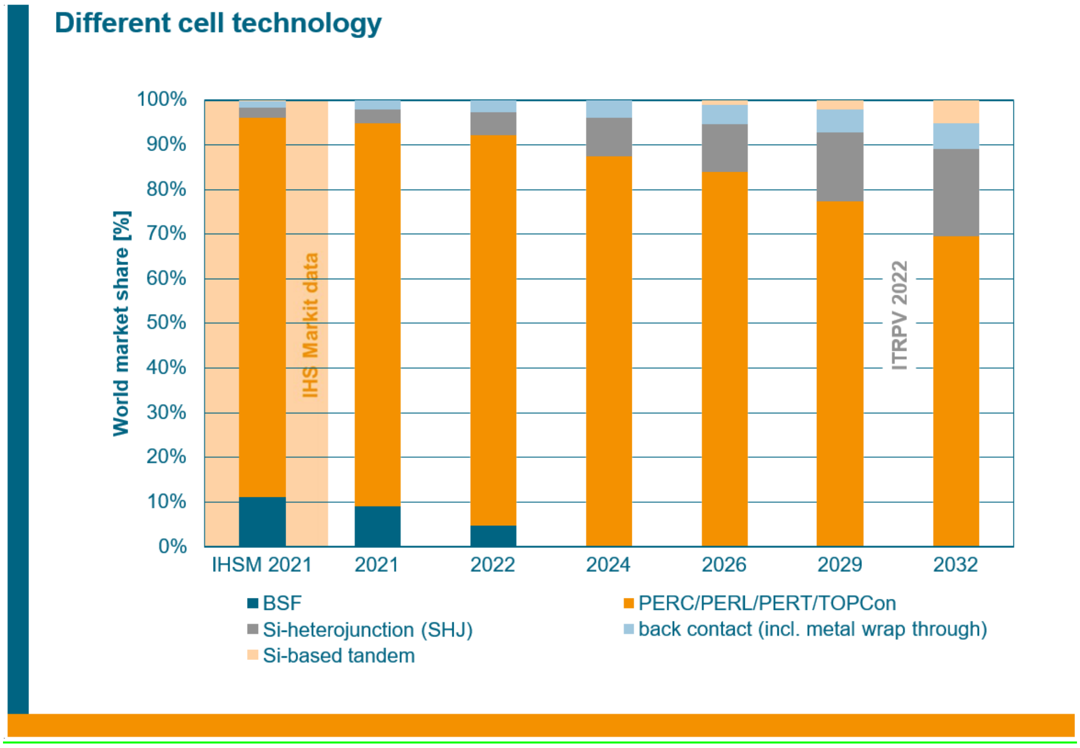

Figure 1.1. Market share estimates for various cell technologies. Data from IHS Markit for 2021 are listed as a source. [22].

The commercial dominance of double-sided contact cell designs is further shown by Figure 1.1. We predict a move from 2% in 2021 to roughly 5% in 10 years, which is not a major change in the market share for rear-side contact cells. Si-based tandem cells are anticipated to enter large production after 2024, which is later than anticipated in the 12th edition.

Trends in cell technologies are shown in Figure 1.2, which has a passivated, diffused pn-junction on the front side and a passivated rear side. Different methods may be used to create these cells. The most developed method employs p-type material with an Al_2O_3 passivation layer and a SiN_x capping layer. With the use of this method, around 10% of PERC cells were created in 2021; 85% of these cells were PERC on p-type mono-Si. In 2022, it is predicted that this proportion will remain at a very comparable level. However, it is anticipated that during the next 10 years, the PERC on the percentage of p-type mono-Si would drop to roughly 40%. Up to 2025, PERC on mc-Si material will likewise be phased out. Within the next ten years, ideas for n- and p-type materials with passivated contacts that use tunnel oxide passivation stacks at the back side will increase in market share from around 10% in 2022 to 58%. For conceptions with passivated contacts, we predict that n-type bulk material will become the norm and that p-type material will only be used in a substantially lesser proportion.

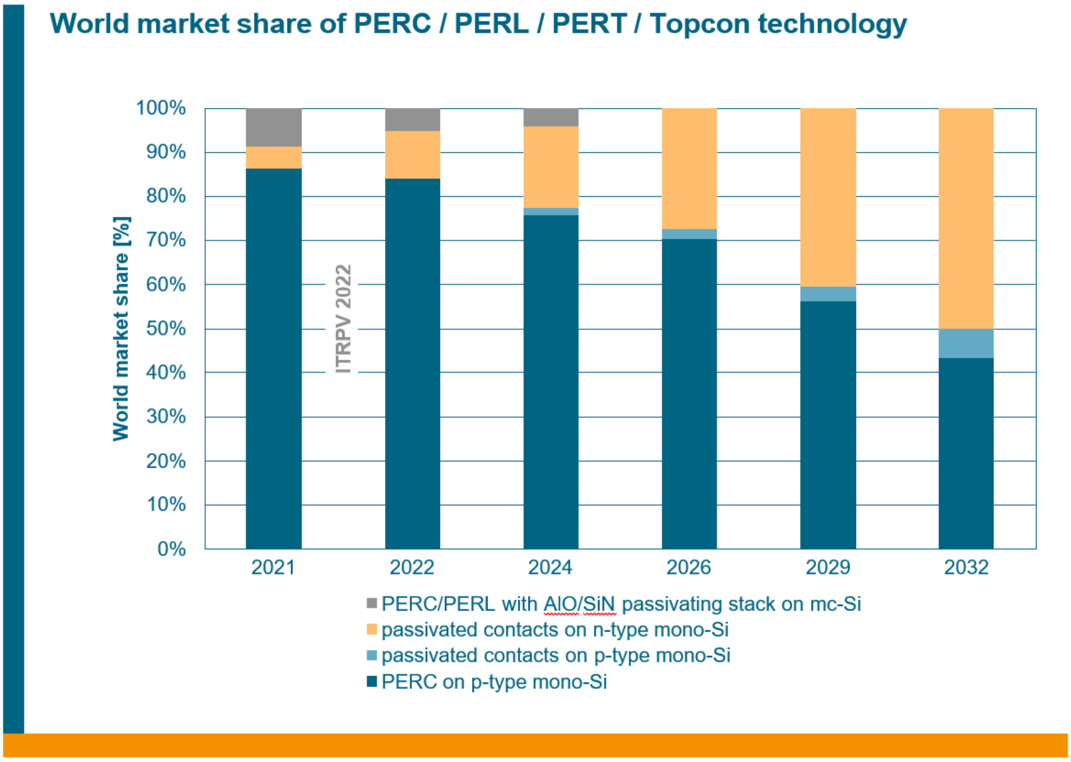

Figure 1.2. Market share for c-Si cell concepts with pn-junction on the front and different rear side passivation Technologies [22].

If the electrical connections are made properly, all cell types outlined in Figure 1.1 as well as SHJ cells may catch light from both the front and the back. Therefore, this cell type is ideal for bifacial light capture. The anticipated market trend for bifacial cells is shown in Figure 1.3. Within the following ten years, the market share, which will be 50 percent in 2021, is anticipated to rise dramatically to 85 percent. Bifacial cells may be utilized in standard monofacial modules or in modules with a transparent back side (bifacial modules).

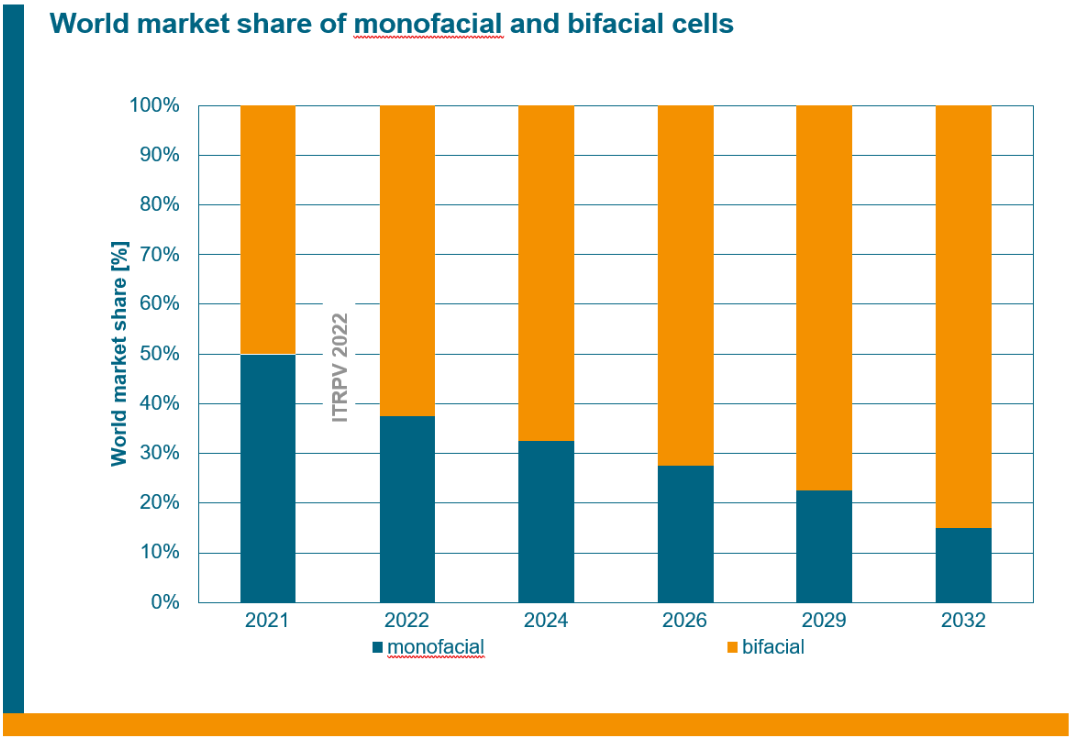

Figure 1.3 Market share for bifacial cell technology [22].

In TOPCon (Tunnel Oxide Passivated Contacts) cell designs [23], rear side contacting is accomplished by tunneling electrons rather than by making ohmic contacts to the bulk silicon. This method completely eliminates recombination current losses at resistive bulk contact and decreases the formation of recombination centers at the interface. Tunnel oxide formation may be carried out in situ using a different technique or as a separate process step. It is anticipated that in situ formation used in conjunction with another procedure will become the dominant method. By using chemical vapor deposition (CVD) techniques such as low-pressure chemical vapor deposition (LPCVD), plasma-enhanced chemical vapor deposition

(PECVD), or physical vapor deposition (PVD) techniques, the poly-Si layer may be created. According to Figure 1.4, PVD methods are rapidly developing, but PECVD is predicted to overtake LPCVD as the favored technology during the next several years.

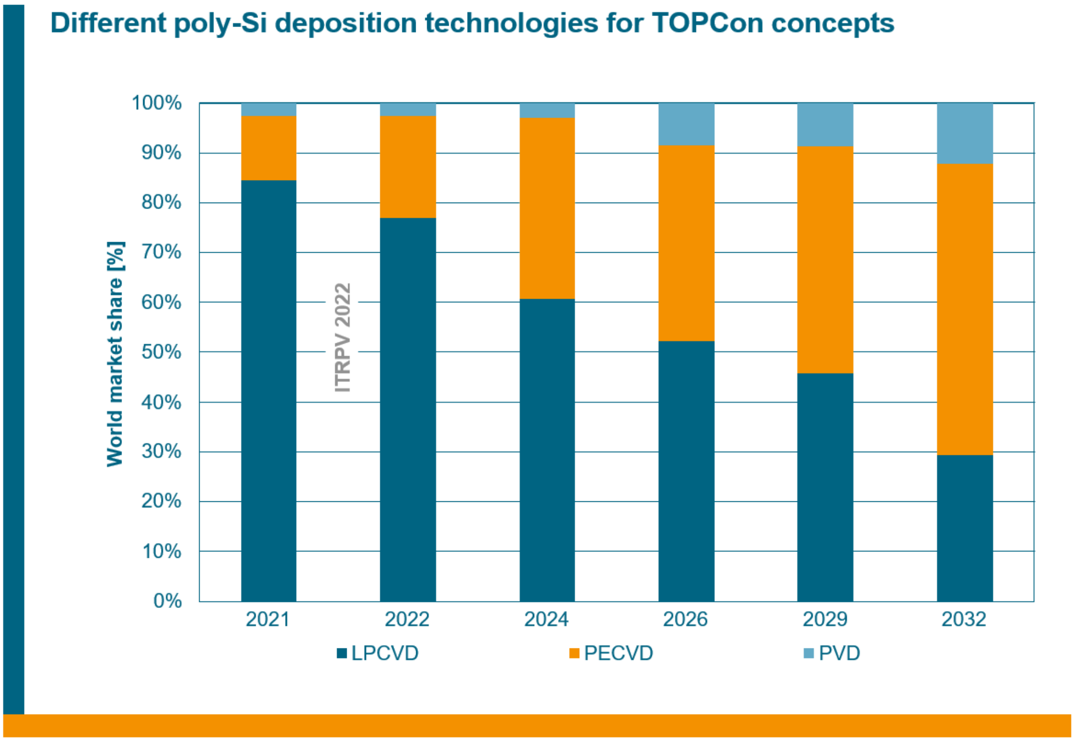

Figure 1.4 Expected trend of forming the polysilicon layer of TOPCon contacts [22].

The anticipated percentage of doping techniques for the poly-Si layers is shown in Figure 1.5. In situ doping is anticipated to enter the mainstream in the near future. This is in accordance with the pattern in Figure 1.4, which shows that the deposition process has a major role in how poly-Si gets doped. In situ doping is employed in PECVD layer doping, but ex situ doping is favored for LPCVD and PVD.

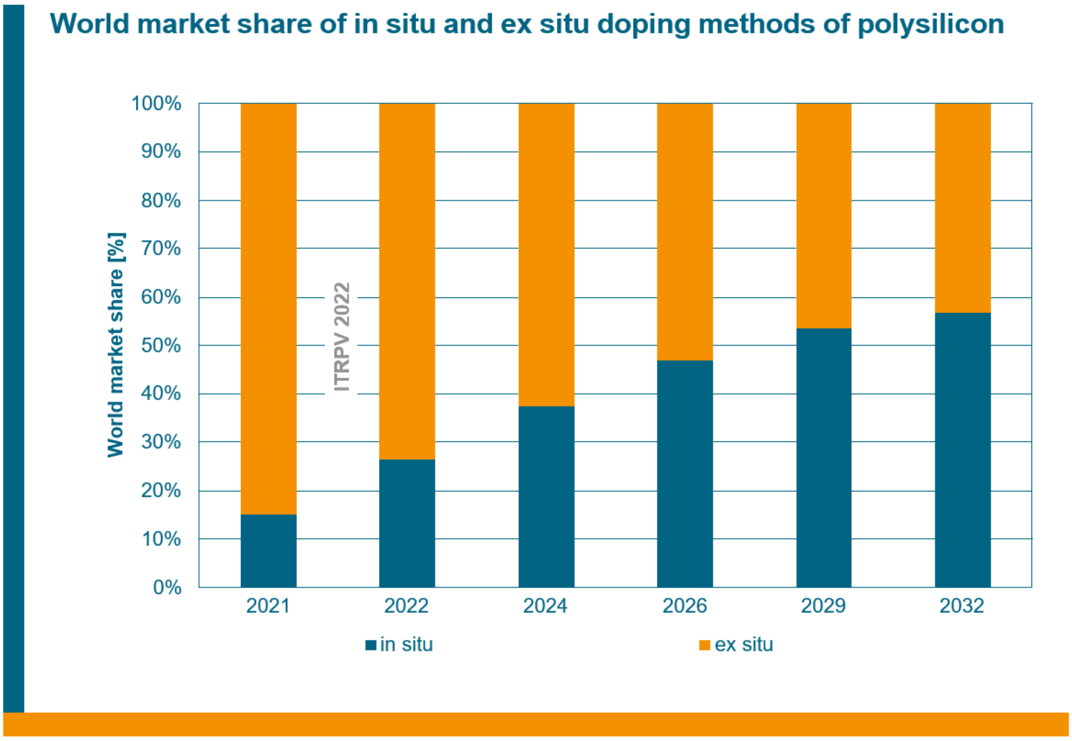

Figure 1.5 Expected trend for forming the tunnel oxide and doping the ploy Si capping layer in passivated contact forming [22].

In the next years, many top solar modules will use N-Type TOPCon technology. N-Type TOPCon (Tunnel Oxide Passivated Contact), which was adopted in a similar way to the conversion of polycrystalline/poly PERC to mono PERC (P-Type), increases module efficiency by taking a step toward increased power density from a designated region. Because it has been made more practical and N-Type TOPCon technology has entered the mainstream thanks to cell makers, TOPCon is here to stay on a massive scale. The attractiveness of TOPCon over the widely used PERC technology of the previous decade is that with solar, the tiniest percentages make the largest effect. However, advantages go beyond only efficiency. In comparison to traditional mono PERC technologies, temperature coefficient, which may be one of the most important elements outside of Standard Test Conditions (STC), has greatly improved.

The 700W bifacial TOPCon solar modules have a maximum cell level efficiency of 25.4 percent, which is the greatest known efficiency for large area industrial TOPCon solar cells to date, according to a recent announcement by Chinese PV module producer Jolywood [24]. Additionally, it was discovered that the module-level efficiency was higher—between 21.73 and 22.53 percent—than the average stabilized efficiency of mass-produced TOPCon solar modules. Contrarily, LONGi, the second well-known solar module producer, said that it had successfully developed 25.19 percent p-type TOPCon solar cells based on monocrystalline CZ c-Si wafers that had been marketed, proving the feasibility of p-TOPCon solar cells on an industrial scale [25]. However, the specifics of the method they used to achieve such a high efficiency rating have not yet been made public [26].

Currently, market share, cost management, and mass production effectiveness are all clearly in favor of N-type TOPCon. The power gap between N and P-type modules will eventually widen as TOPCon cells' efficiency rises. Process improvement and new technology will result in ongoing cost reductions [27,28]. The recent volatility in the price of Ag (silver) use, as well as the PV industry's rising percentage of industrial Ag usage, are factors that are predicted to motivate attempts to cut Ag consumption in solar cells, according to a research by Kafle, et al. [29]. The most optimistic possibility, according to the International Roadmap for Photovoltaics, is to cut the cell's Ag consumption by 50% of its present level [22]. According to Kafle, et al. [29], it's important to remember that TOPCon cell metallization costs are comparable to PERC cell metallization costs, with the former possibly achieving lower watt-peak prices ($/Wp) due to increased cell power. This is assuming that future metallization concepts allow for a 50% reduction in Ag usage (Figure 1.6).

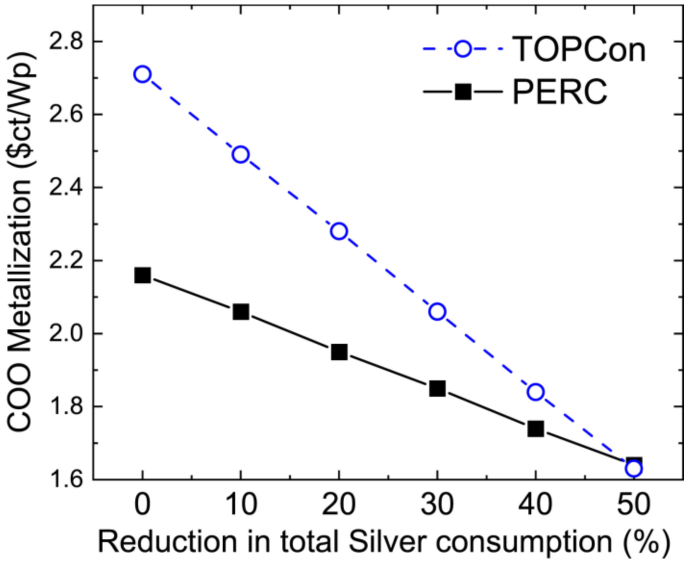

Figure 1.6. Reduction in total Silver consumption (%) [29]

Recently, TOPCon solar cells have shown exceptional cell performance. They are projected to be used in field deployments and production line implementations [30]. Jolywood solar technology co. ltd. reported the average bifaciality of 85% and low temperature coefficient of -0.32%/K analyzed for n-type bifacial TOPCon modules of 331 W (60 cells) and 392 W (72 cells) in production their line [31]. Light-Induced Degradation (LID), which happens in all p-type silicon solar cells, is the main issue in favor of n-type TOPCon over PERC. When oxygen and boron from the positive silicon layer combine, a slight, instantaneous drop in power generating capacity happens. Due to the additional boron that PERC cells often contain, this issue may be severe. Light and elevated temperature-induced degradation (LeTID) is a different issue that may affect all PERC cells and is made worse by greater operating temperatures and more intense light. Extreme circumstances may result in power degradation of up to 7%, which would significantly reduce long-term power capacity and prevent customers from producing the anticipated amount of energy. If a facility saw such a drastic decline, the Levelized cost of energy (LCOE) would be negatively affected. In order to assure long-term power for enduring performance, N-type TOPCon's property of not being sensitive to LID and LeTID is very important and appealing to investors. The industrialized response to the LID and LeTID problem is

N-type TOPCon. As shown by Jinkosolar, the Tiger Neo module with N-Type TOPCon technology may substantially lower the danger of LeTID to almost nil. The absence of LID and LeTID is of enormous value to investors given the wide variety of temperatures experienced across the globe as well as the various operating conditions and irradiation solar panels experience [32]. In essence, progresses in TOPCon solar cell developments in industry was the motivation to establish a non-hazardous and low-cost.

CHAPTER 2

LITERATURE REVIEW

High-efficiency solar cells are the main focus of an increasing number solar cell producers. N-type technology is becoming more prevalent in the market, and cell efficiency has been steadily rising. The TOPCon was considered as the next possibility for high-efficiency solar cells in mass manufacturing after PERC in order to achieve even higher performance. In addition, TOPCon offers an application that is ideally suited for achieving cell efficiencies higher than 25%.

2.1 The development of TOPCon photovoltaics

As previously remarked, solar cells with passivated contact will soon have the largest market-share. As a result, PERC and TOPCon solar cells are the main focus of the present research on solar cell designs. However, the market-dominating PERC solar cells are expected to be superseded by TOPCon solar cells in the future owing to issues such rear contact openings and carrier saturation at localized metallic contacts. Fraunhofer ISE released the first report on the advancement of TOPCon solar cells in 2013 [8]. According to the study by Feldmann et al., adding a phosphorous-doped poly silicon layer and an ultra-thin silicon dioxide layer (SiO_2) at the metal-semiconductor interface may dramatically reduce surface recombination on the back side of n-type crystalline silicon solar cells. In order for current to tunnel through chemically generated silicon dioxide layer quickly and effectively, its thickness was limited to 1.4 nm. By using the PECVD approach, “a 20 nm phosphorous doped amorphous silicon layer” was applied to this ultra-thin oxide layer. This layer was then subjected to a high temperature annealing procedure in order to become a doped poly-Si layer.

According to the annealing parameters, a very strong surface passivation was found, “which led to a very high implied open-circuit voltage (iV_{oc}) of over 710 mV and a very low recombination current density ($J_{0,rear}$) of around 9–13 fA/cm^2. This innovative method was given the term TOPCon (Tunnel Oxide Passivated Contact) structure, and the solar cells that it is used in are called TOPCon solar cells”. They use a design of a TOPCon solar cell, which has a diffused boron-doped p+ emitter and a tunnel oxide passivated rear contact. Boron-doped p^+ emitter was passivated by a stack of aluminum oxide (Al_2O_3) and silicon nitride (SiN_x) layers that were formed using atomic layer deposition (ALD) and plasma-enhanced chemical vapor deposition (PECVD), respectively. Furthermore, it is widely known that the silicon nitride (SiN_x) layer also functions as an anti-reflection coating (ARC) to increase optical confinement inside the solar cell.

High implied fill factor (iFF) as well as high implied voltage (iV_{oc}) were attained using this innovative structure under both maximum power point (MPP) and open-circuit (OC) situations. During the cell construction process, the Ti/Pd/Ag seed layer was thermally vaporized to create the front side metallic contacts, and the Ag layer was then electroplated on top. The metallic fingers' width was left at 20 micrometers. On the other hand, the back side metallic contact was made of thermally evaporated Ti/Pd/Ag stack. The best cell eventually showed “a power conversion efficiency of 21.81 percent with an active cell area of 4 cm^2 based on 200 µm thick, (100) oriented, 1 Ω.cm, n-type FZ silicon wafers”. It also had “a short circuit current density (J_{sc}) of 38.4 mA/cm^2, an open-circuit voltage (V_{oc}) of 690.8 mV, and a fill factor (FF) of 82.1 percent”. The greatest power conversion efficiency, in contrast, was attained by similar solar cells without the TOPCon structure on the back side, “with V_{oc} of 638.3 mV, J_{sc} of 37.8 mA/cm^2, and FF of 81.1 percent”. Therefore, it may be seen why adding TOPCon structure to the back of crystalline Si solar cells is important.

The process flow of TOPCon solar cell reported by Feldmann et al is began by selecting “a single-side shiny-etched 200 µm, (100) oriented, 1 Ω.cm n-type FZ Si wafers (2 cm × 2 cm)”. Cleaning of wafers fulfilled by standard RCA process. P+ emitter was established by diffusion of boron into random pyramid texturing of n-type wafer's front side (140 Ω/sq). An ultra-thin SiO_x layer (wet chemical process) of 1.4 nm grown on the wafer and "subsequent 20 nm phosphorous doped amorphous Si layer (PECVD process)" deposited at the rear shiny-etched side. Solid-phase crystallization was conducted with high temperature annealing (optimized annealing temperature ~ 850℃) in N_2 ambient. Front p+ emitter passivated by deposition of Al_2O_3 layer by ALD coating and additional SiN_x layer deposition by PECVD.

The band diagram of several interfaces, including a-Si/c-Si, poly silicon with tunnel oxide/c-Si, and amorphous/poly silicon with tunnel oxide/c-Si, is shown inFigure 2.1 (TOPCon). These band bending diagrams provide a clear understanding of the efficient and streamlined separation of photo-generated carriers at the rear side of the n-Si base for a TOPCon solar cell.

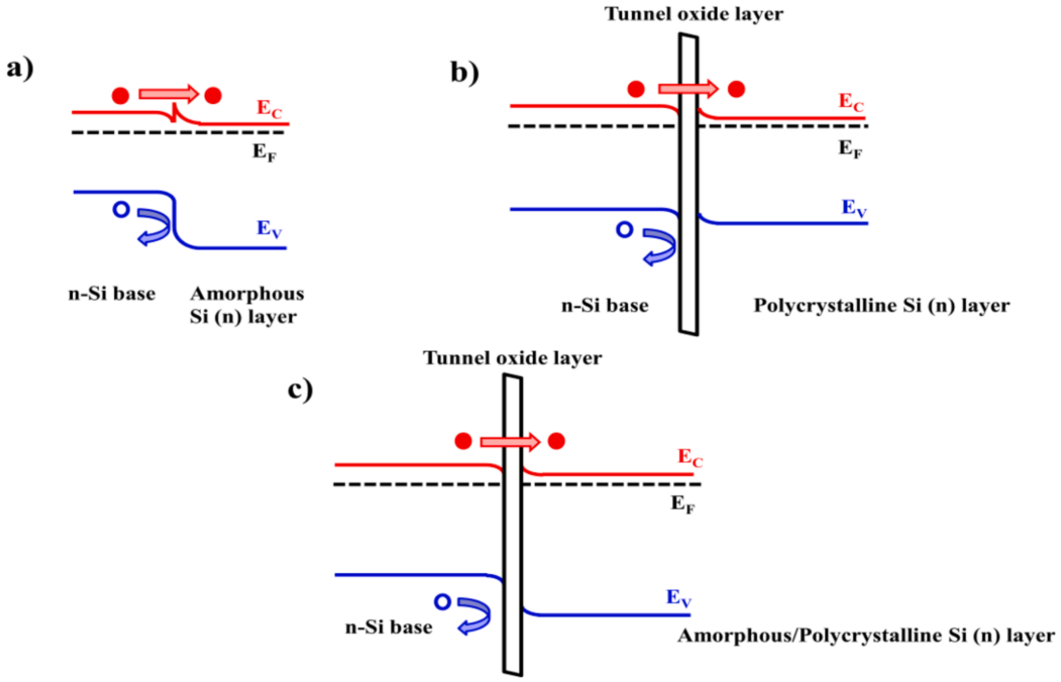

Figure 2.1. Band diagram of different passivated contact technologies: (a) a-Si/c-Si heterojunction, (b) poly silicon with tunnel oxide, and (c) TOPCon [22].

Richter et al. reported on the impact of wafer thickness and bulk resistivity on the power conversion efficiency of TOPCon solar cells in 2017—nearly one and a half years later [18]. N-type FZ Si wafers with a thickness variation of 150, 200, and 400 μm and a resistivity of 5 Ω.cm were employed in the investigation. On the other hand, the research of resistivity variation used 200 µm n-type FZ Si wafers with three distinct resistivities—1, 5, and 10 Ω.cm. A conversion efficiency of roughly 25% was obtained by solar cells with all these variables. However, a significant decline in FF and pseudo-FF (PFF) was seen with an increase in base resistivity.

Due to their affordability, p-type Si wafers are more frequent in the industrial setting than n-type Si wafers. Therefore, creating a TOPCon structure using p-type c-Si wafers would be a good idea. So, using planar, shiny-etched, 250 µm, p-type, 1 Ωcm, orientated FZ silicon wafers as their substrate, Feldmann et al. created symmetrical n-TOPCon and p-TOPCon structures [33,34]. The investigation demonstrated that the n-TOPCon structure's passivation quality was better to that of its substitute. As a result, we can say that the n-TOPCon structure's interface passivation quality is satisfactory for both n-type (as indicated before) and p-type Si wafers. The symmetrical p-TOPCon structure, on the other hand, provided inferior interface passivation (“iVoc = 680 mV”) quality because there were more defects in the bulk Si layer and at the Si/SiOx interface. Finally, p-type Si solar cells with active cell areas of 2 cm × 2 cm were created, with n-TOPCon serving as the front emitter and p-TOPCon providing the rear surface field. This was done to better understand the impact of including carrier selective contacts on the cell performance. The “Voc (693.5 mV) and FF (81%)” of the solar cells with an amorphous Si emitter were greater than those with a semi-crystalline Si emitter. The latter, however, offered increased Jsc as a result of enhanced blue response. As a result, both cell groups' achieved efficiency was almost identical (“17.9 percent for amorphous silicon emitter and 17.8 percent for semi-crystalline silicon emitter”). However, enhancing the p-passivation contact's quality may enable it to enhance its power conversion efficiency.

Additionally, using “250 µm thick, shiny-etched, 1 Ωcm, orientated p-type FZ silicon wafers”, double-sided contact solar cells with n-TOPCon on the textured front side and p-TOPCon on the planar back side were also created [35]. The construction of both-sided TOPCon solar cells with a p-TOPCon structure on the front side and an n-TOPCon structure on the back side was reported by Tao et al. in 2018 [36].

Additionally, the scientists investigated the effects of ITO sputtering on n-TOPCon and p-TOPCon structures that were “symmetrically constructed onto 3-8 Ωcm, n type, double-sided polished CZ c-Si wafers”. The research showed that the effectivinority carrier lifetime (τ_{eff}) suffered significantly from the RF-magnetron sputtering approach used to deposit ITO layers onto the p-TOPCon and n-TOPCon structures. However, following ITO deposition, considerable recovery of eff was seen for p-TOPCon samples upon high temperature (500 °C) annealing, but n-TOPCon samples only displayed a minor recovery of τ_{eff}. This discrepancy in eff recovery might be explained by the greater improvement in p-type poly-Si film quality after heat treatment. The research also showed that ITO layer deposition at ambient temperature and very modest RF power may optimize τ_{eff} recovery.

CHAPTER 3

SOLID PHASE CRYSTALLIZATION OF *IN SITU* DOPED AMORPHOUS SILICON

3.1 Introduction

Crystallization of amorphous Si is of interest for the fabrication of thin film transistors and high-efficiency thin film solar cells. The use of polycrystalline Si (poly-Si) thin films fabricated from the crystallization of amorphous Si (a-Si) has recently been proposed to form an emitter layer on a thin oxide layer, producing a tunnel oxide passivated contact (TOPCon) and polysilicon on oxide (POLO) solar cell devices. In these applications, an a-Si layer could be first deposited on a substrate, then crystallized by a high temperature heat treatment process, either with standard furnace or laser annealing [37-39].

Ideally, a-Si could be described as a covalently bonded, fourfold-coordinated, continuous, random network of Si atoms [40]. Through high temperature annealing, concurrent bond rearrangement and defect annihilation take place in the structure of the initially amorphous Si films. This leads to the crystallization process, which results in poly-Si structures [41].

When different well-established production methods for a-Si deposition, such as chemical vapor deposition (CVD) and physical vapor deposition [42-45] are compared, the electron beam evaporation (e-beam) method [37] is considered to be the most convenient way of fabricating non-hydrogenated amorphous silicon due to its high deposition rate. Meanwhile, CVD techniques, generally, use pyrophoric gas of SiH_4 and H_2 for silicon thin film fabrication which could produce hydrogenated a-Si (a-Si:H) layer. Doping is an important part of Si thin film fabrication. In CVD techniques, the doping of silicon films is usually obtained by using gases such as B_2H_6 or PH_3 [42,43], which are expensive and hazardous. In the e-beam method, however, the a-Si films are initially undoped. As an alternative way, effusion cells can be added to the e-beam chamber to supply an *in situ* flux of boron atoms by high temperature evaporation [38,46].

Crystallization of doped and undoped amorphous Si can be realized by various methods, such as solid-phase crystallization (SPC) [37,38,45,46], laser induced crystallization (LIC) [39], and metal induced crystallization (MIC) [47,48]. The latter two methods have their own advantages, but SPC is the most basic and direct of these crystallization techniques [38]. One disadvantage of LIC is that control over the heat transfer of laser light is limited by the film thickness [39,49]. Moreover, thin films crystallized by MIC can have residual metallic impurities due to the finite solubility of the metal in silicon at the eutectic temperature [50].

As mentioned above, e-beam evaporation enables deposition of non-hydrogenated a-Si thin films. This is important when controlled quality of crystallization is required (e.g., for poly-Si layers of TOPCon and POLO solar cells). The crystallization kinetics of hydrogenated a-Si (a-Si:H) depend on the amount of hydrogen coordinated to silicon. For the crystallization process, the Si–H bond must be broken, and hydrogen has to diffuse out of the structure. Therefore, the presence of hydrogen can suppress the control of crystallization, and in some cases, it can cause bubble formation (blistering) [51], which leads to deformation of the film. Takenaka et al. has shown that dehydrogenation process in the a-Si:H films is correlated with the nucleation as hydrogen dissociation generates crystalline nuclei [52,53]. Moreover, in the case of hydrogenated a-Si, hydrogen atoms are located at the bond-centered (BC) site between B and neighboring host Si atoms, which could result as boron-hydrogen simple complex, namely H-B passivation center. This argument is also negligible for the case of non-hydrogenated a-Si that could reveal a relatively more active boron doping in silicon host lattice [54].

Moreover, doping also affects SPC kinetics. Csepregi et al. [55] suggested that presence of boron (phosphorous) dopant concentration greater than 10^{19} atoms/cm^3 increases the crystallization rate in a-Si:H thin films prepared by SPC process. This effect has also been observed in other studies [56-59]. However, crystallization kinetics in the case of lower boron doping levels, and for the thin films with homogenously distributed boron doping through the depth of the film, have not been studied in detail. Boron doped thin films were prepared by an e-beam evaporator equipped with effusion cells (e-Beam EC) enabling *in situ* doping. We utilized SPC to crystallize the e-beam EC deposited a-Si thin films.

It is known that when the thin film fabrication method is changed, the crystallization kinetics can change which could lead to alteration of the electrical properties of poly-Si thin films. Hence, a deeper understanding of the corresponding crystallization process is crucial since such films can be potentially used in solar cell structures, e.g. passivated contact solar cells. In this manuscript, we are presenting a detailed investigation of the crystallization kinetics depending on the dopant concentration of boron doped poly-Si thin films prepared by a rather rarely used (and still developing) technique, electron beam evaporation of Si with in-situ doping of effusion cells (e-beam EC) which has quite important advantages when compared to other commonly used techniques such as CVD types. The e-beam EC technique does not require usage of any hazardous or pyrophoric precursor gas, and it has non-toxic exhausted byproducts while providing a higher deposition rate compared to CVD techniques. This system enables to fabricate *homogenously* boron doped Si thin films. Note that, doping can be realized in a gradual and *controlled manner*, step by step from a low doping level to heavily doping levels. The e-beam EC-fabricated films are non-hydrogenated and therefore, the solid phase crystallized silicon thin films could be blister-free. Whereas, solid phase crystallization of CVD-fabricated films could result in pin-holes originating from hydrogen-induced blistering which is hard to exclude due to dehydrogenation [51-53].

The concentration and depth/spatial distribution of the dopant play an essential role in the electrical performance of semiconductor devices. We analyzed doped poly-Si films produced using different process parameters, e.g., with different effusion cell temperatures. The corresponding boron concentrations were explored by time-of-flight secondary ion mass spectroscopy (ToF-SIMS) [60]. Raman spectroscopy and grazing incidence X-ray diffraction (GIXRD) [61] were used to trace the crystallization kinetics and obtain information about the amount of the stress in the film.

We present that a high boron concentration (e.g., more than ca. 10^{20} atoms/cm^3) altered the crystalline structure and lattice parameter of the poly-Si thin films investigated in this work. Boron has a relatively low solubility in silicon, which can result in clustering of boron atoms inside the silicon lattice [62]. This, eventually, affects the electrical activity of the boron atoms [63]. Analysis of the B_{1s} binding energy for heavily boron-doped as-deposited a-Si films and SPC-crystallized samples, using X-ray photoelectron spectroscopy (XPS), revealed information about the Si–B coordination in the structure [64,65].

Solid phase crystallization kinetics for boron doped a-Si:H has already been discussed in the literature [51-53], and it was found that an increase in boron concentration leads to increase in crystallization rate [55]. Whereas, a thorough study for non-hydrogenated in-situ boron doped a-Si has not been done before. Crystallization kinetics may differ for a-Si:H [55] and non-hydrogenated boron doped Si thin films. Hence, detailed work on the dopant effect in crystallization is crucial for the e-beam EC-fabricated Si thin films. Here, we present a detailed work on the effect of boron doping in crystallization for e-beam EC-fabricated non-hydrogenated silicon thin films, when the dehydrogenation process does not trigger the nucleation (which is the case for a-Si:H thin films).

3.2 Experimental details

In this study, e-beam EC technique was used for precise boron doping (Figure 3.1). The base pressure was 10^{-5} Pa. Effusion cells were manufactured by MBE-

Komponenten, and were originally designed for molecular beam epitaxy applications and have the quality required for precise doping.

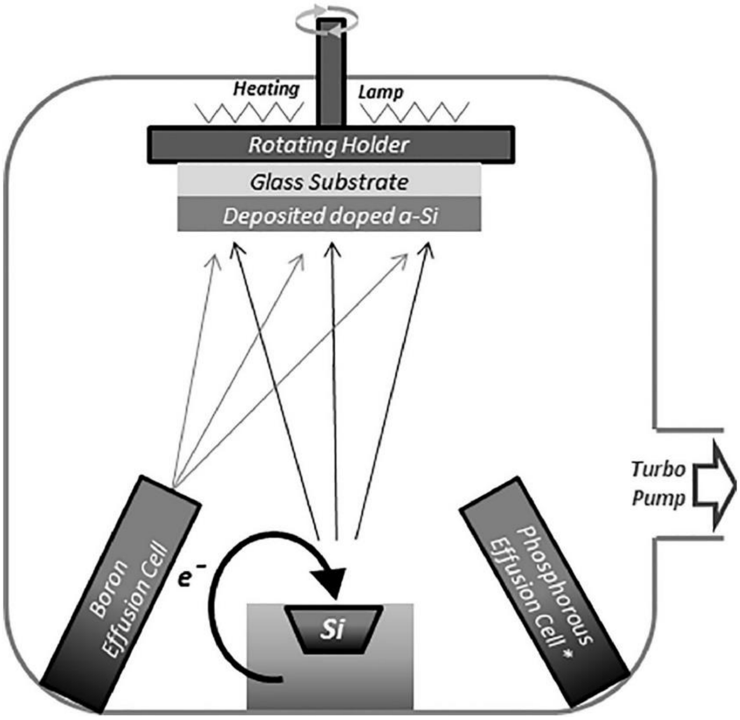

Figure 3.1. Schematic presentation of the effusion cell equipped e-beam evaporator (e-beam EC). * Denotes that though not used for the study presented in this paper, the e-beam EC chamber accompanies a separate effusion cell for phosphorous doping.

The substrate used in this study was glass, which is low cost and appropriate for thin film silicon technology applications. During the evaporation process, the substrate was placed on a sample holder located above the e-beam evaporation system. The e-beam evaporates Si, allowing the formation of an amorphous thin layer on the substrate. This thin a-Si layer is *in situ* doped with pure boron that is evaporated by the effusion cell.

The SPC process used in this work depends on the duration of annealing. The crystallization of silicon takes place at around 600 °C, which is critically high for ordinary glass substrates. The SPC process could be prolonged with annealing times up to several hours to obtain the crystal formation at this critical temperature [66]. Therefore, the glass substrate used in this study should endure 600 °C annealing processes without any deformation. For this aim, *Schott AF-32 eco* glasses were chosen. However, this type of glass contains high amounts of boron and aluminum, which can diffuse inside the Si film during the annealing procedure [65] and undesirably change the electrical properties of the crystallized films. To overcome this problem, 80 nm of silicon nitride (SiN_x) was first coated by plasma enhanced CVD to act as a diffusion barrier on the properly cleaned glass substrate. The fabrication and characterization of the SiN_x coating with efficient diffusion barrier has already been described in our previous publications [67].

The coated glasses were cleaned by acetone, alcohol, and water before loading into the e-beam chamber. The deposition process was initiated only after the vacuum level reached 10^{-5} Pa. Silicon deposition was conducted at a fixed deposition rate of 1 Å/s for the whole sample set. Four different deposition processes were conducted with effusion cell temperatures of 1700, 1800, 1900, and 2000°C. Substrates were pre-heated up to 400 °C to make the sample tolerable to any further possible stress introduced by post-thermal treatment of the crystallization process [68]. The deposition was performed at 400 °C until the film thickness reached 180 nm for each sample. The four sets of samples, named B1700, B1800, B1900, and B2000, were then annealed at 600 °C, which is the critical temperature of SPC for a-Si production. These annealing procedures were accomplished in a tubular furnace under nitrogen flow to avoid any further chemical reactions during the SPC process. For the crystallization kinetic study, annealing processes were enrolled with durations of 6, 12, 18, 24, 36, 48, and 93 hours. The annealing processes were continued until fully crystallized films were fabricated. Note that we prepared separate samples for each crystallization study.

The change in the boron dopant concentration with the change in the effusion cell temperature was analyzed by ToF-SIMS (*ION-TOF ToF-SIMS 5*). The Depth profile extracted from ToF-SIMS data measured by Bi_1 as the primary ion and oxygen source with 500 eV for sputtering. The Hall Effect measurements were performed in the Van der Pauw configuration which revealed carrier concentration and resistivity of the boron doped silicon thin films. The crystallization kinetics were studied by

Raman spectroscopy (*HORIBO Jobin Yvon iHR550*) step-by-step for each annealing process and crystallization duration until the fully crystallized samples were achieved. Raman measurements were conducted by a laser beam with a wavelength of 532 nm. The fully crystallized samples were analyzed by GIXRD with an incident angle of 0.3 degrees to cross-check the crystal quality of the thin films. The measurement were performed using a Rigaku Ultima IV diffractometer with a Cu-K_α (λ=1.541 Å) source radiation, 40kV anodic voltage, and 50mA current at each stage of the continuous scanning with sampling width of 0.02 degree in parallel beam geometry. Finally, XPS (*PHI 5000 VersaProbe*, ULVAC-PHI, Inc.) was used to obtain information about the Si–B coordination. XPS studies were carried out with a monochromatic Al-K_α X-ray source (1486.6 eV) as the X-ray anode at 24.7 W with energy pass value of 58.70 eV at a fixed incident angle of 45.0°.

3.3 Results and Discussion

Amorphous Si samples (a-Si) with 180 nm a-Si, 80 nm of SiN_x were prepared with various boron concentrations. In order to control the concentration of the boron dopant in the thin films, the temperature of the effusion cell was varied from 1700 °C (lower limit for an efficient boron evaporation of the e-Beam EC) to 2000 °C (upper limit for boron evaporation of the e-Beam EC). The concentration of the boron dopant was analyzed by ToF-SIMS with a scan-depth of the films to the point when it reaches the SiN_x layer. ToF-SIMS is a mass spectrometer for elemental analysis and provides us with the total amount of dopants (substitutional and interstitial). As seen in Figure 3.2, increasing the temperature of the effusion cell led to an increase in the concentration of boron throughout the thin film. The ToF-SIMS data represent a homogenous distribution of boron dopant throughout the film thickness for all the samples investigated in this work. B1900 was measured at EAG Laboratories and used as the calibration sample for ToF-SIMS measurements of this work. By this way, it was possible to evaluate the boron dopant concentrations for the whole sample set by applying the relative sensitivity factor which was 7.82 × 10^{21}. ToF-SIMS depth profiles revealed that the average boron concentrations for B1700, B1800, B1900, and B2000, are 3 × 10^{18}, 2 × 10^{19}, 7 × 10^{19} and 3 × 10^{20} atoms/cm^3, respectively. This shows our ability to control the dopant concentration with the temperature of the effusion cell. Moreover, Hall Effect electrical measurements were performed. The carrier concentrations (indicating the number of active dopant concentrations) were measured to be 2.73 × 10^{16}, 4.84 × 10^{18}, 3.64 × 10^{19} and 8.36 × 10^{19} cm^{-3} for B1700, B1800, B1900, and B2000, respectively.

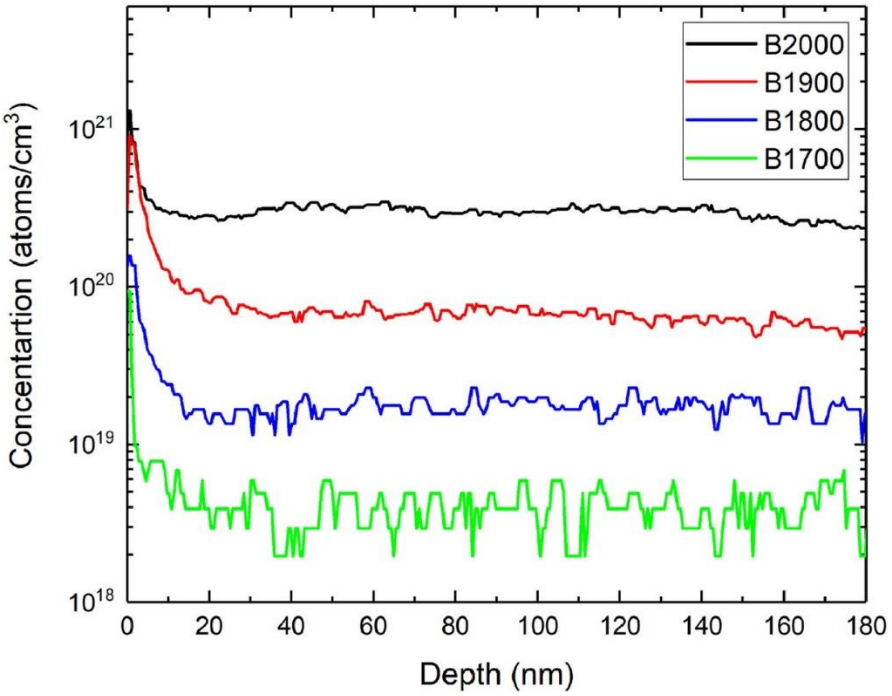

Figure 3.2. ToF-SIMS depth profiles of boron-doped samples with various effusion cell temperatures (T_{efc}) of 1700, 1800, 1900, and 2000 °C which are abbreviated as B1700, B1800, B1900, and B2000, respectively. The corresponding concentration of boron dopants are given in the text.

With the aim of understanding the mechanism of crystallization in boron-doped Si thin films, we conducted Raman spectroscopy for these samples after annealing for various durations (Figure 3.3). We ensured the accuracy of the Raman spectra by averaging the data obtained from three different points on each sample. Raman spectra presented in Figure 3.3 consist of several underlying sub-spectra which can be deconvoluted to three major components at 520 cm^{-1}, 510 cm^{-1}, and 480 cm^{-1}, originating from the transverse optical-phonon mode peaks of the Si–Si bonds of large crystal grains (>10 nm), small crystal grains (<10 nm), and amorphous phase [69], respectively. Boron-doped samples with different amounts of dopant exhibit different growth kinetics in SPC [70]. Thus, the higher the boron concentration in a-Si thin film, the shorter the crystallization duration. For instance, the heavily boron-doped sample (B2000) is almost fully crystallized after annealing for 12 h, while the lightly doped sample (B1700) is not fully crystallized even after annealing for 48 h instead it takes up to 93 h to fully crystallize (Figure 3.4). When compared to this work, CVD-grown hydrogenated a-Si films are crystallized after longer incubation times, i.e. crystalline Raman peak appears only after the hydrogen atoms are removed from the lattice [52,53]. Note that, such a crucial hydrogen dissociation process does not significantly affect the crystallization of e-beam evaporated non-hydrogenated a-Si.

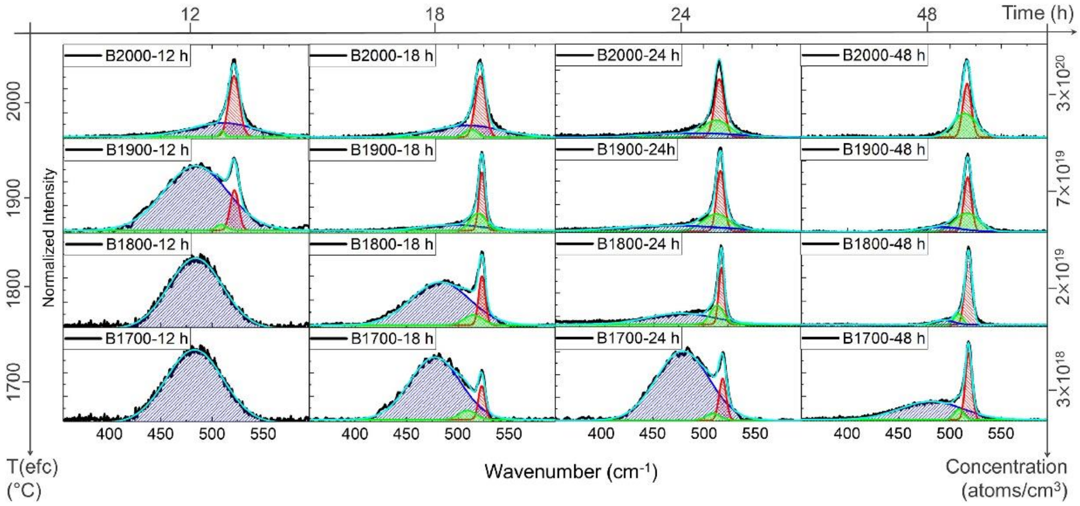

Figure 3.3. Raman spectra of boron-doped Si samples annealed at 600 °C for 12, 18, 24, and 48 h.

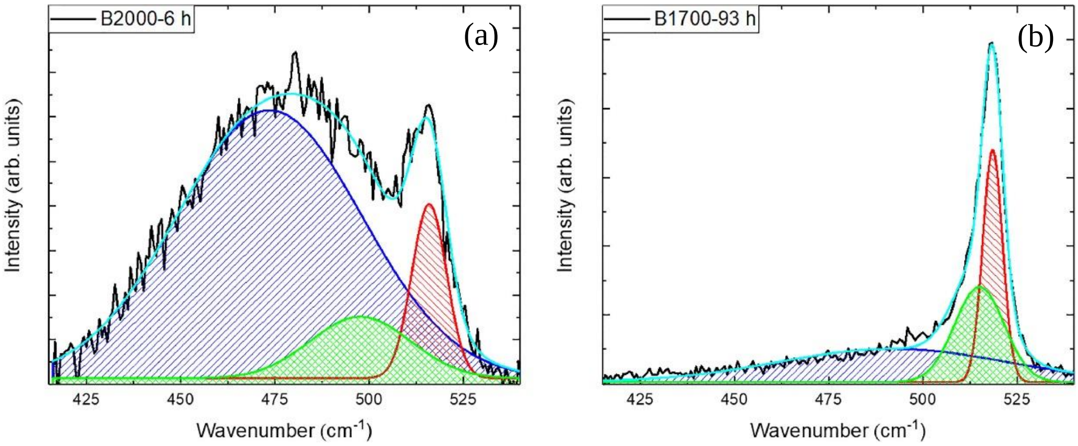

Figure 3.4. Raman spectra of boron doped samples annealed at 600 °C for (a) 6 h of B2000 and (b) 93 h of B1700.

Furthermore, in the case of fully crystallized samples with different amounts of boron doping, subtle differences are observed in Raman peak position and full width at half maximum (FWHM) of the crystalline peak at 520 cm^{-1}. As described above, the sample structure consists of three different materials: glass substrate, SiN_x coating on glass, and the deposited Si thin film. These layers have different thermal expansion coefficients, which cause stress during the annealing process of the SPC. This stress is revealed when the Raman spectra of the poly-Si samples are compared to that of a monocrystalline Si reference sample (denoted crystalline Si, c-Si) [71]. The variations of phonon frequencies are proportional to the magnitude of the corresponding stress. The FWHM principally reflects the defect density, whereas the effect of stress cannot be neglected when the lattice strain is substantially large or non-uniform. With increasing boron doping, the Raman peak around 520 cm^{-1} exhibits a shift of the longitudinal optical - transverse optical (LO-TO) phonon vibrational modes to lower wave numbers with respect to the original position. This could be indicative of a tensile stress [71,72] caused by boron doping. As shown in Figure 3.5, there is a shift of Raman signal of the doped poly-Si as compared to the signal of the c-Si wafer which indicates a tensile stress. Moreover, as the amount of boron doping increases, a further shift is observed which also contributes to the tensile stress.

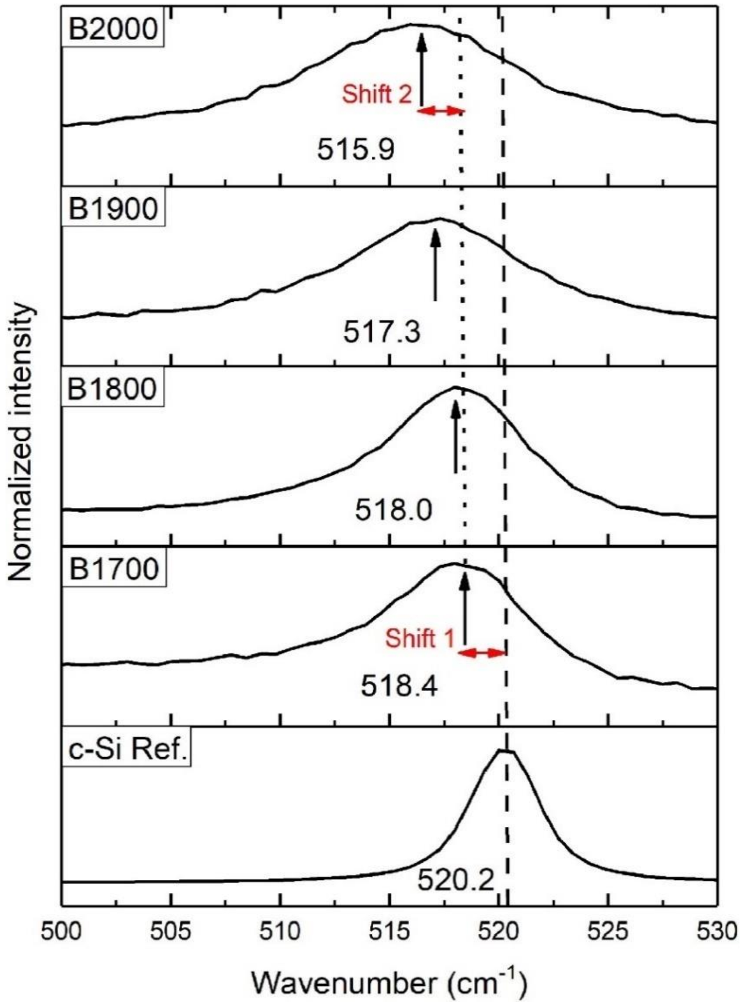

Figure 3.5. Raman spectra for c-Si TO peaks for fully crystallized samples at 48 h in 600 °C with different effusion cell temperature (boron concentration). Corresponding peak shifts are indicated.

The shift of the wavenumber of 520.2 cm^{-1} (for c-Si) to 518.4 cm^{-1} for B1700 (Shift 1 as denoted in Figure 3.5) can be attributed to the thermal expansion induced stress between silicon thin film and glass substrate. The further shift from 518.4 cm^{-1} (B1700) to 515.9 cm^{-1} (B2000) (Shift 2 as denoted in Figure 3.5) indicates the change in the amount of stress induced by the increase in boron concentration owing to the difference in the atomic radius of boron (8.7×10^{-9} cm) and silicon (1.11×10^{-8} cm). However, owing to the fact that even the sample with the highest boron concentration (B2000) contains 99% Si, the effect related to the change in the lattice contraction is expected to be minimal. Therefore, we suggest that the increase in the boron concentration triggers a change in the growth kinetics, which also contributes to the total shift of as much as 2.5 cm^{-1} wavenumbers when the Raman spectra for B1700 and B2000 are compared. The relationship between the FWHM and the lower-frequency peak shift for c-Si wafer and SPC film is shown in Figure 3.6. The magnitude of the stress can be estimated from the wave number shift of the LO-TO peak compared to that of the stress-free c-Si according to Equation 1 [71].

$$\sigma(\mathrm{MPa}) = -435\ (\omega_s - \omega_0)\ (\mathrm{cm}^{-1}) \qquad (1)$$

where ω_s is the wave number of the stressed sample and ω_0 is the wave number of the LO-TO phonon mode in stress free c-Si. The phonon shift corresponds to the isotropic part of the phonon shifts obtained in biaxial stress experiments [72]. The change in stress in the poly-Si thin films is found to be 1087.5 MPa when the amount of boron dopant is increased from ca. 10^{18} (for B1700) to 10^{20} atoms/cm^3 (for B2000) (Figure 3.7).

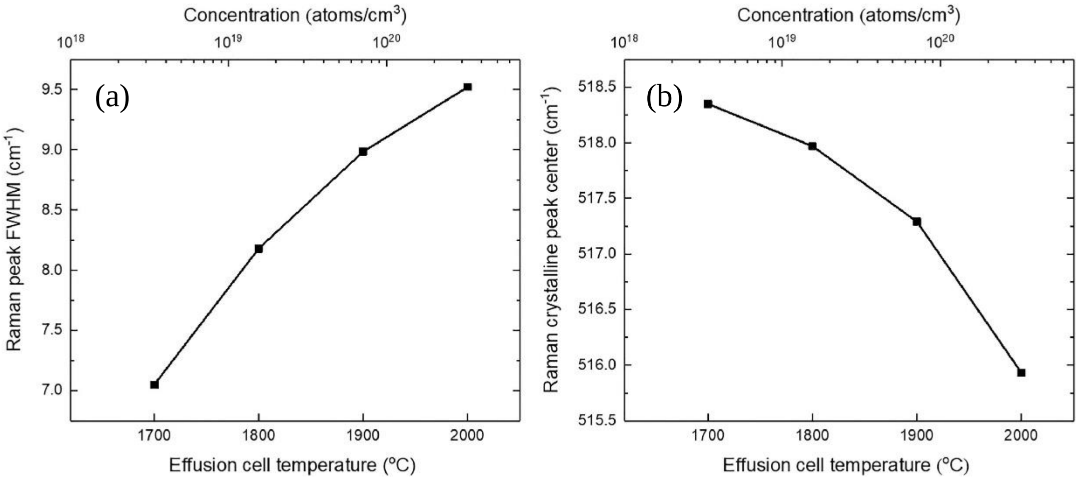

Figure 3.6. (a) FWHM changes and (b) peak shifts of Raman spectra for TO peaks of c-Si for samples crystallized for 48 h at 600 °C vs effusion cell temperature (and thus boron concentrations).

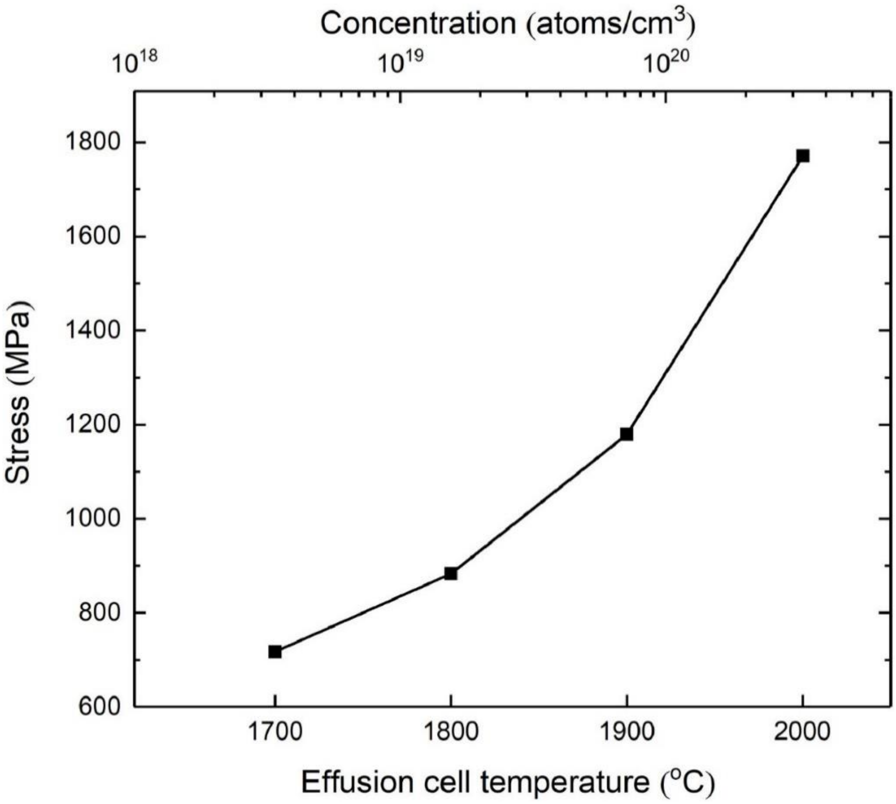

Figure 3.7. Amount of stress calculated from the shift in the wavenumber of the Raman spectrum for Si crystalline peak with respect to 520 cm^{-1} (contribution of bulk c-Si).

In the case of small-grained poly-Si (‹x› < 500 nm), the intensity of the LO-TO phonon line increases rapidly with increasing average grain size. Once the average grain size exceeds 500 nm, the increase in the intensity of the Raman peak becomes less pronounced. A higher crystallization rate leads to a smaller grain size, because nucleation starts in a greater number of sites despite the same limited amount of material. Consequently, each crystallite site involves less material.

Furthermore, the overall crystallinity of thin films can be determined from the deconvolution of crystalline peaks from the amorphous phase in the Raman spectra. For this purpose, the Raman shift at 520 cm^{-1} was deconvoluted by the process in Equation (2), which calculates the extent of crystallization [73]:

$$x_c = \frac{(I_c + I_i)}{(I_c + I_i + I_a)} \tag{2}$$

where I_a, I_i, and I_c are the integrated Raman intensities corresponding to the amorphous, intermediate, and crystalline phases, respectively. The changes in the Raman crystal fraction (x_c) with annealing time are presented in Figure 3.8. The slope of the linear part of the growth is obtained from the plots between “nucleation” and “crystal domination”, i.e., between 12–48 h for B1700, 12–36 h for B1800, 6–24 h for B1900, and 6–18 h for B2000. This slope reveals the crystal growth [76]. Thus, it is shown here that fully crystallized samples are achieved for each boron concentration.

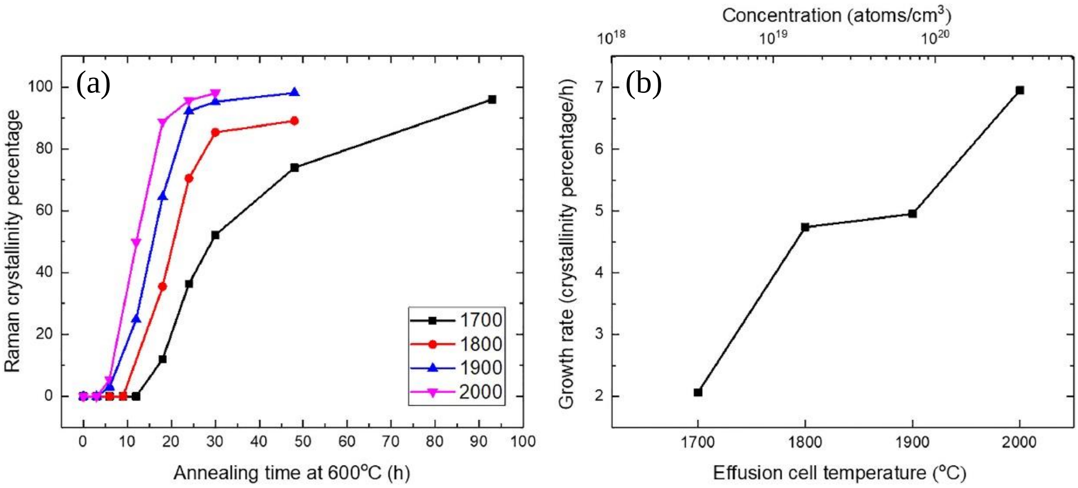

Figure 3.8. (a) Raman crystallinity percentage *vs* annealing time at 600 °C, and (b) growth rate (Raman crystallinity percentage/h) *vs* effusion cell temperature for B1700, B1800, B1900, and B2000.The corresponding Raman spectra are presented in Figure 3.3 and Figure 3.4.

Fig. 8 (right) presents the corresponding crystal growth rate which clearly increases upon boron concentration. On the other hand, for CVD-grown hydrogenated a-Si thin films, crystallization requires longer incubation times when the amount of hydrogen increases [52,53]. Since the a-Si thin films investigated in this work are non-hydrogenated, crystal growth is not hindered due to hydrogen dissociation process. This makes applications with crystallization process remarkably advantageous when a-Si thin films are grown with e-beam EC as compared to other common techniques such as CVD.

Besides Raman spectroscopy, GIXRD with 0.3 degree was applied to investigate the crystal structure of the fully crystallized boron-doped thin film samples with effusion cell temperatures of 1700, 1800, 1900, and 2000 °C, annealed for 93, 48, 36, and 24 hours at 600 °C, respectively (Figure 3.9). GIXRD is more appropriate than XRD to investigate the crystal structure of thin films, since the depth of field through the film (in this study, 180 nm) is established by smaller incident angles (e.g., 0.3 degree) [61]. As seen in Figure 3.9, for all poly-Si samples investigated in this work, (111), (220), (311), (400), and (331) plane peaks were observed in the diffraction spectra of GIXRD between 20–80 degrees (2θ). Thus, GIXRD also proves the crystallization in each degree of boron doping. Note that all the diffraction peaks were normalized to the (111) plane peak.

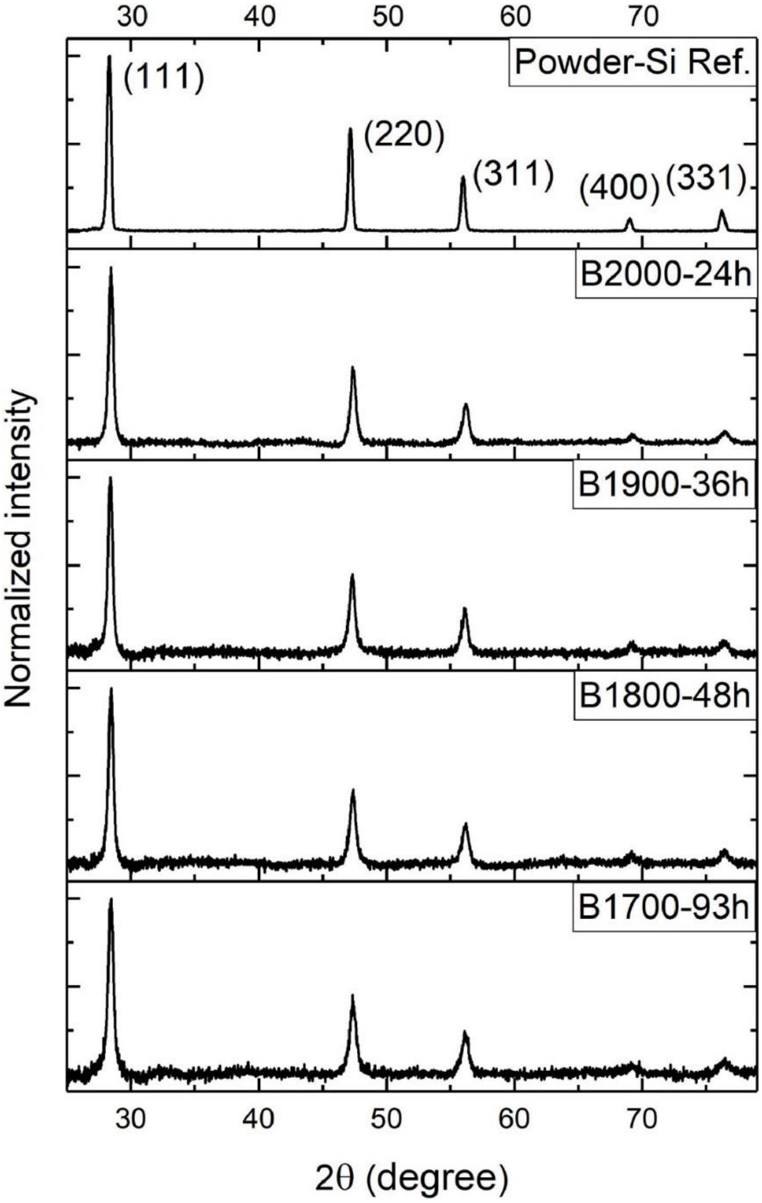

Figure 3.9. GIXRD analysis for a powder-Si reference sample and fully crystallized samples of B2000, B1900, B1800, and B1700, which were annealed for 24, 36, 48, and 93 h at 600 °C, respectively.

Furthermore, we accumulated GIXRD measurements in order to observe the changes in silicon lattice constant in the presence of the substitutional boron dopants in the case of heavily boron-doped samples. Figure 3.10 presents the corresponding GIXRD spectra which is accumulated 70 times with steps of 0.01 degree between $2\theta = 68.8$ and 70.2 degrees for the (400) plane spectra of the poly-Si samples. The (400) plane was chosen since it is symmetric and gives the best resolution to observe possible changes in lattice structure. The diffraction peaks at 69.49 degree for B1700 slightly shifts to 69.44 degree for B2000. This could be related to the tensile stress owing to the increase in the boron concentration. A shoulder peak at 69.72 degree was observed by Ulyanenkova et al. [62]. This peak was attributed to lattice contraction due to the presence of boron in silicon lattice which was not resolved in our case.

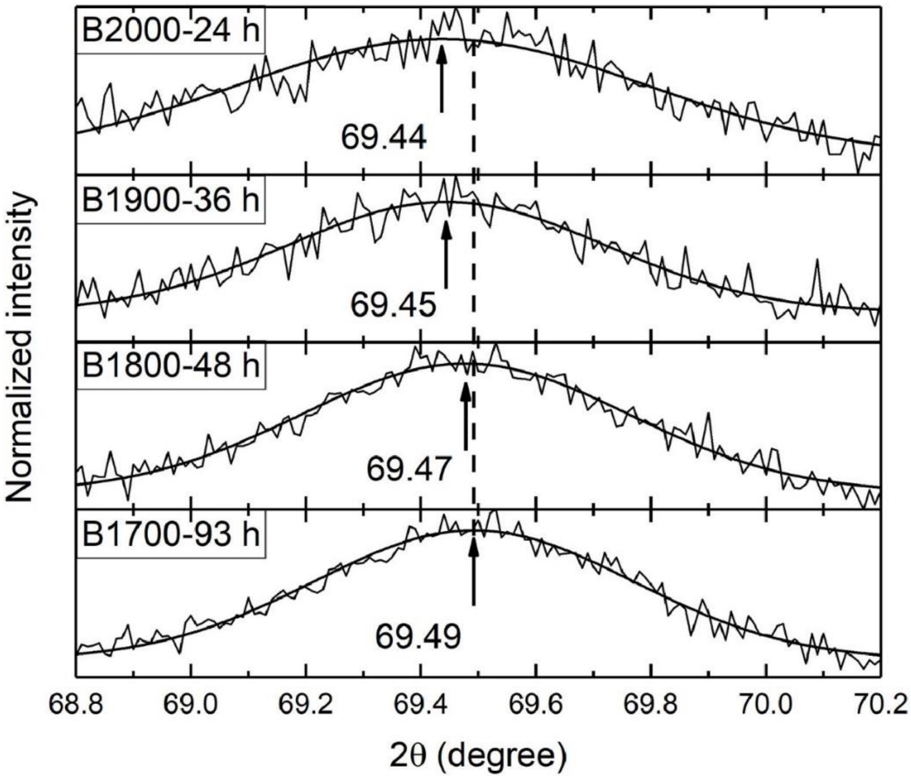

Figure 3.10. Accumulated GIXRD spectra for (400) plane spectrum for the fully crystallized samples of B1700, B1800, B1900, and B2000.

In order to investigate the chemical environment of B atoms in the Si lattice, XPS was employed for a heavily doped sample (B2000) after and before annealing for 24 hours at 600 °C (B2000 24h) (Figure 3.11 (a) and (b)). These spectra can be deconvoluted into five signals (Gaussian/Lorentzian ratio is 0.8 for each indicated signal while FWHM is kept constant) with B_{1s} binding energies of 193.1, 190.4, 188.4, 186.3 and 183.0 eV. Note that, due to the detection limits of XPS ($>10^{20}$

atoms/cm^3), only the heavily boron-doped sample (B2000) gave a reasonable resolution. As seen in Figure 3.11 (c), the signals at 188.4 and 193.1 eV are also observed for B1800. However, due to the detection limit of XPS, the main signals (186.2 and 183.0 eV), standing for active boron atoms observed for B2000, are not resolved for B1800. Furthermore, elemental boron (the pure boron which was used as the source in the effusion cell in e-Beam EC) was also measured, and the corresponding XPS spectrum revealed a peak at 188.4 eV as shown in Figure 3.11 (d). Thus, the signal at 188.4 eV in Figure 3.11 (a) and (b) can be attributed to interstitial boron in the sample. The contribution of this signal, however, is relatively small compared to the other deconvoluted lines. Moreover, its intensity is decreasing upon annealing (Figure 3.11 (c) and (d)), indicating that the interstitial boron atoms in the as-deposited sample become substitutional (active) boron atoms. Furthermore, signals observed at 190.4 and 193.1 eV for either amorphous or crystallized B2000 samples could indicate B–O binding [64]. Similar spectra were also observed by Tsutsui et al. [64] and Hao et al. [65]. In literature, there is contradictory assignments for the other two peaks (at 186.3 and 183.0 eV), attributed to various configurations of boron atoms inside the silicon matrix [64,74]. Interestingly, when the XPS signals of amorphous and crystallized B2000 samples are compared, the binding energies do not change upon crystallization. Thus, there is no evidence for considerable change in the location of boron atoms in the silicon lattice, or of an increase of boron oxide formation during the fabrication process. Hence, this shows that boron contributes to the crystal growth mechanism without drastically changing its coordination with silicon atoms.

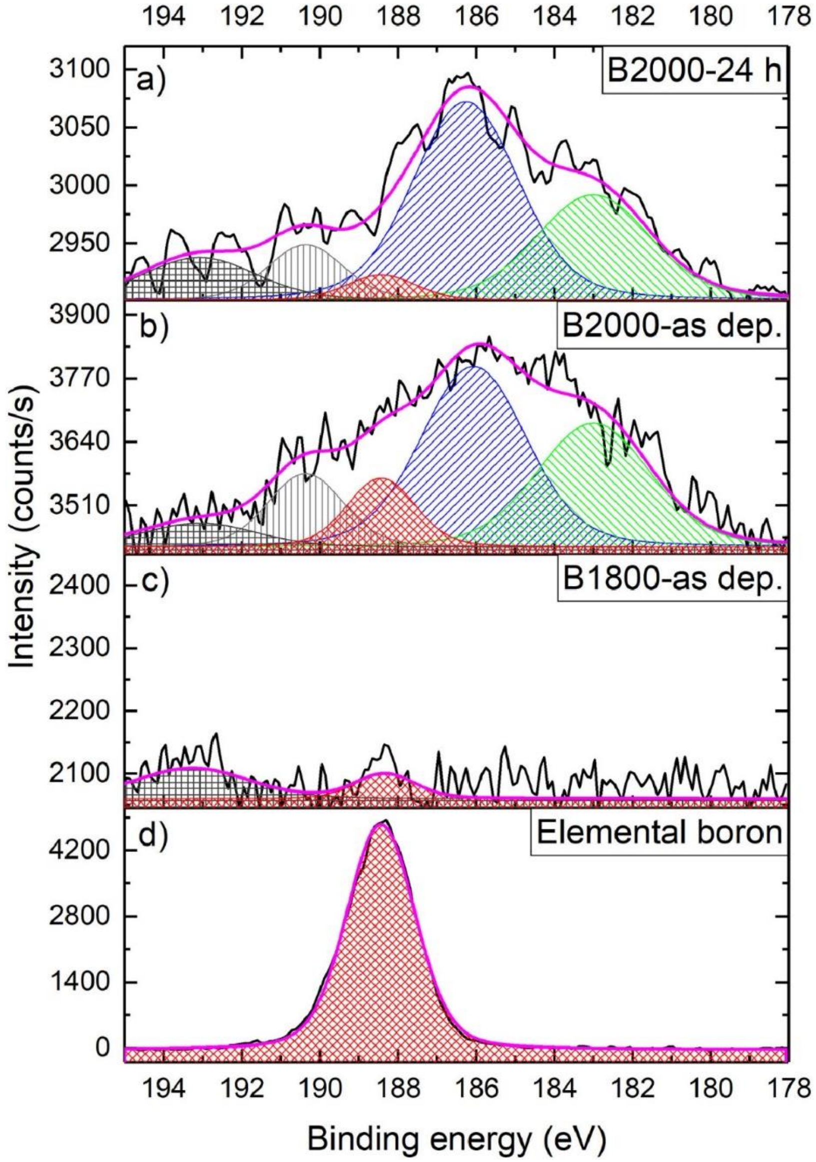

Figure 3.11. XPS spectra of a) heavily boron-doped silicon thin film (B2000) annealed for 24 h at 600 °C (poly-Si), b) amorphous silicon thin film as deposited (as-dep.), c) moderately boron-doped silicon thin film (B1800) (as-dep.), and d) elemental boron (measured from pure boron which was used in effusion cell).

In addition to the structural analysis by Raman spectroscopy and GIXRD, for potential photovoltaic application, it is essential to investigate the electrical properties of these samples. It is known that, change in doping concentration results in change in electrical properties. As ToF-SIMS results revealed, the total concentration of dopant increases by increasing the effusion cell temperature which changes the charge carrier density. This directly affects the corresponding conductivity of the thin film semiconductor. By current-voltage measurements, it is possible to calculate the resistivity (conductivity) of the boron-doped silicon thin films B1700 to B2000. In Figure 3.12, the corresponding resistivity values with respect to effusion cell temperature (boron concentration) versus resistivity and conductivity are presented. The resistivity (conductivity) value drops (rises) by increasing the effusion cell temperature and consequently by increasing the dopant concentration in the fully crystallized thin films. Increase in boron concentration results in a drastic drop in resistivity from orders of 10^2 to the 10^{-3}. Thus, the electrical effect of boron doping manifested itself in the clear change in resistivity.

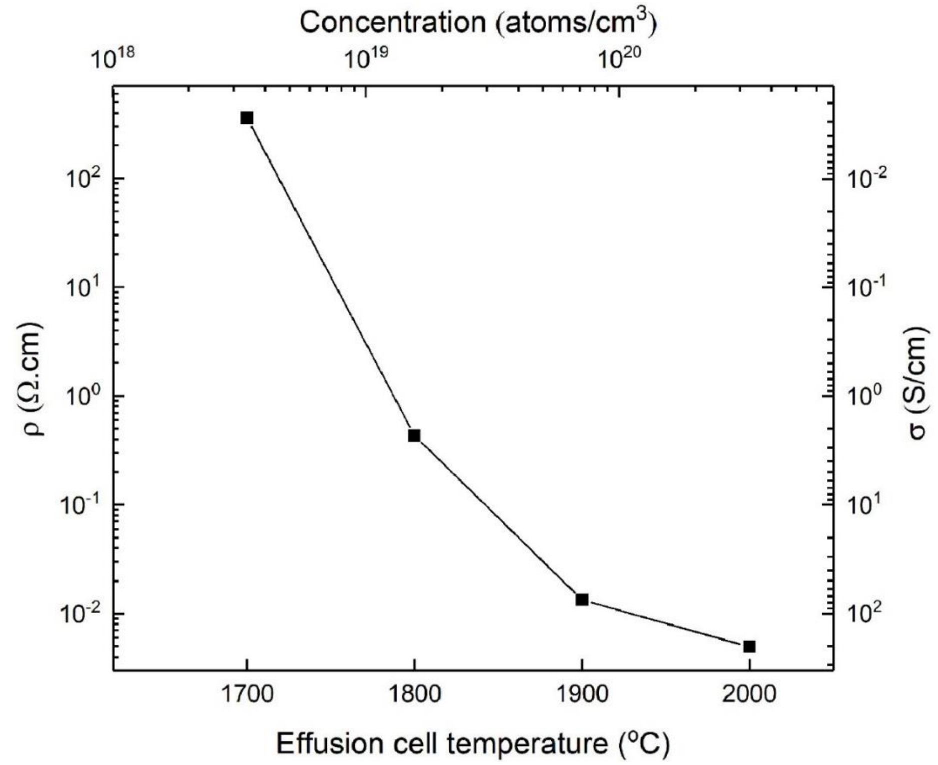

Figure 3.12. Electrical measurements of the fully crystallized samples with different amount of boron.

3.4 Conclusions

In this work, boron-doped Si thin films were prepared by an e-beam evaporation technique equipped with effusion cells. We monitor the solid phase crystallization via a systematical approach with Raman analysis of a series of samples. The gradual improvement of the crystalline peak through step by step annealing, gave a more detailed picture of the crystal growth. It was shown that the presence of boron atoms in a-Si leads to an increase in the crystallization rate, which is accompanied with the development of a tensile stress in the film. Crystal growth is not hindered due to hydrogen dissociation process, since the a-Si thin films investigated in this work are non-hydrogenated. Overall, we show that increase in boron doping increases the crystallization rate for non-hydrogenated silicon thin films prepared by e-beam EC.

Moreover, the effect of the dopant concentration is also reflected in the Raman spectra, i.e., the change in FWHM and the shift in the crystalline peak revealed the change in the crystalline properties of poly-Si thin films, e.g. increase of the stress value in the thin films. Owing to the increase in the FWHM, presumably, the higher rate of crystallization originates from the higher amount of nucleation sites with respectively higher boron concentrations. A slight shift in GIXRD for the (400) plane was observed, which might be due to the stress caused by the boron guest atoms in the silicon host lattice of the heavily boron-doped thin films.

We also made use of XPS analysis in order to compare the coordination of the boron atoms in non-hydrogenated boron doped as deposited a-Si thin films and solid phase crystallized poly-Si thin films. From the XPS analysis, we observed that B_{1s} binding energies of amorphous and crystallized B2000 sample do not change. This indicates that there is no significant change in the B–Si coordination during the crystallization process. The electrical effect of boron doping was observed in a drastic drop in resistivity from orders of 10^2 to the 10^{-3} Ω.cm.

CHAPTER 4

DESIGN OF PASSIVATING CONTACT SOLAR CELLS

The effective creation of electron-hole pairs upon light exposure and the simple transfer of these photo-generated carriers onto an external circuit are key factors in the performance of TOPCon solar cells. To put it another way, generating high efficiency TOPCon solar cells may be the consequence of boosting the optical confinement within the absorbing layers of the solar cells and improving the surface passivating quality. By enhancing the doped poly-Si layer and the ultra-thin SiO_x tunnelling layer, the passivating quality of the TOPCon structure may be improved. In addition, lowering the front emitter's recombination current density is crucial to achieving greater power conversion efficiency. The unabsorbed light from the back side metallic contact is reflected back into the absorbing layer of the solar cells in order to increase the value of J_{sc} and subsequently conversion efficiency. To enhance the quality of the front emitter, doped poly-Si layer, ultra-thin SiO_x layer, and rear side light management, we will examine a variety of findings that have been reported in the parts that follow.

4.1 Tunneling oxide passivating contact components

4.1.1 Ultra-thin SiO_x layer

The quality of the surface passivation, thermal stability, and carrier tunneling capabilities of the ultra-thin SiO_x layer may be determined. As a consequence, several research have been conducted over the years on a variety of topics, including the best way to build a high-quality tunneling layer, the qualities needed to achieve better interfacial passivation, and the effect of pinhole presence on carrier tunneling.

“In 2014, Moldovan et al. reported that doped a-Si:H layer deposition followed by sub-thermal treatment at very high temperature (up to 900 °C) produced ultra-thin SiO_x layers grown on planar Si surfaces by hot HNO3 oxidation (NAOS), providing excellent surface passivation quality with an iV_{oc} of more than 720 mV” [75]. However, textured Si surfaces at the same 900 °C annealing temperature showed a significant decline in the interface passivating quality. This result may be attributable to the textured surfaces developing a non-homogeneous tunnel oxide layer.

Finally, by using these variously produced ultra-thin SiO_x layers for the creation of the TOPCon structure, n-TOPCon solar cells with complete area passivated rear contacts were created. For the construction of the TOPCon structure, an optimum annealing temperature of 800°C was used, yielding a power conversion efficiency of 24.8 percent at a V_{oc} of 716 mV.

Typically, with a thicker SiO_x layer as dry thermal oxidation (DryOx), just quantum mechanical tunneling is unable to provide enough carrier transport channels, increasing the amount of series resistance (Rseries). This led to a lesser FF being obtained. However, excessive charge carrier transit via pinholes in oxide layer formed in higher annealing temperatures, reduced the cell's performance. Therefore, increased cell performance may be achieved with optimal pinhole density and size.

4.1.2 Poly-Si layer

Doped poly Si layer, in addition to the ultra-thin SiO_x tunnelling layer, is crucial to the TOPCon structure's ability to passivate. The manufacturing technique, doping concentration, layer thickness, annealing environment, annealing duration, temperature, and even post-annealing treatments all affect the properties of doped poly-Si layers. The various actions used to enhance the doped poly-Si layer's quality are investigated in the this section.

One can worry that using the low frequency industrial scale direct plasma PECVD process to deposit doped silicon layer atop ultra-thin SiO_x tunnelling layer would seriously harm the oxide layer, lowering the passivation quality immediately. However, when the “doped amorphous silicon layer for the formation of the TOPCon structure was deposited using the industrial scalable low frequency plasma enhanced chemical vapor deposition (RF-PECVD) technique, excellent surface passivation quality with an implied V_{oc} (iV_{oc}) of above 735 mV and an implied FF (iFF) of 87.9% was realized” [76].

The research also showed that coupling the low frequency PECVD coated doped poly-Si layer with a thermally developed ultra-thin interfacial tunnel oxide layer produced superior results than mixing it with a chemically created oxide layer. In contrast, Polzin et al. also achieved almost identical findings by realizing a “doped Si layer for the construction of the TOPCon structure using a low frequency batch-type direct plasma PECVD technique” [77].

Sputtering was one of the physical vapour deposition (PVD) methods utilized to create the doped silicon layer [78,79]. By employing a s”ingle co-sputtering system with undoped silicon (99.999 percent purity) and boron (99.999 percent purity) as target materials, Yan et al. created in-situ boron doped silicon films to achieve hole-selective passivated connections” [79]. “After performing a high temperature annealing stage in a N^2 environment, the stack of RF sputtered p-type silicon films and wet chemically produced ultra-thin SiO_x interlayer displayed intriguing passivation characteristics with a J_0 of less than 20 fA/cm^2. Ultimately, 200 µm, 1 Ω.cm, monocrystalline, p-type FZ Si wafers were used to manufacture 2cm x 2cm p-TOPCon solar cells with sputter-deposited doped Si layers. The greatest conversion efficiency was shown to be as high as 23.0 percent with V_{oc} = 701 mV, J_{sc} = 41.1 mA/cm^2, and FF = 79.9 percent. On the other hand, David et al. used a dc sputtering machine to create phosphorous doped silicon layers onto an incredibly thin SiO_x layer to create an n-type passivated contact” [79]. Additionally, symmetric lifespan samples based on n-type c-Si wafers were created, and the maximum value of iV_{oc} —which contrasts with the median value—was determined to be 695 mV.

Therefore, based on Ref. [78,79], we can infer that both p-TOPCon and n-TOPCon structures can be created utilizing a straightforward sputtering procedure with respectable surface passivation quality. Most notably, if sputtering is employed for the formation of doped silicon layers, usage of hazardous chemicals like silane, diborane, and phosphine may be avoided. To compete with the state-of-the-art TOPCon structure with chemical vapour deposited poly-Si layer, considerable improvement in the pasivating characteristics of the TOPCon structure with sputter deposited poly-Si layer is still needed. So far, we have come to the conclusion that high temperature annealing is a crucial and required stage in the activation of the dopants and the crystallization of the doped silicon layer. The thermal budget for making solar cells is obviously increased by the inclusion of such a high temperature annealing stage. Researchers have taken a number of steps in this direction to lower the temperature of the necessary annealing process and/or develop an appropriate substitute strategy for achieving the goals of annealing [80,81].

4.1.3 Blistering

Blister formation is another another significant issue connected to the growth of TOPCon structure [53,54]. Blisters often develop as a result of hydrogen building up at the interface between the doped a-Si:H layer and the SiO_x layer. As the doped a-Si:H layer loses its hydrogen content during the high temperature thermal treatment, this hydrogen buildup mostly occurs during the high temperature annealing process. The development of blisters, which generates inhomogeneity within the film morphology, is what causes the passivating quality of the TOPCon structure to degrade. Therefore, minimizing blister development is crucial to maintaining the integrity of the TOPCon structure. The necessity of a high temperature annealing procedure following the deposition of a doped amorphous silicon layer onto a SiO_2 tunneling layer for initiating the crystallization, according to Li et al., may cause damage to both the ultra-thin tunneling oxide layer and the bulk silicon layer [82].

All these parameters investigated in literature by details [83-85] while defects need more attention.

4.1.4 Defects in the dposited silicon layer

Fundamentally, V_{oc} limiting methods must be discovered if poly-Si solar cells are to achieve their full potential. Several arguments are being made as to why V_{oc} could be restricted right now. An abundance of deep defects, including those thought to be paramagnetic dangling-bond (DB) defects [86], has been linked to the electrical activity of poly-disordered Si's grain boundaries. Dislocations may operate as shallow traps, which was described by Wong et al. Additional options for recombination centers include coordination flaws or vacancies at dislocations and structural defects inside crystalline grains (intra-grain defects). It is well-known that the electrical quality of crystalline Si solar cells is constrained by contaminants introduced into the absorber layer during growth or post-deposition treatments (such as via RTA or post annealing step). Last but not least, it is well-established that post-deposition HP treatments cause structural flaws in crystalline Si (e.g., H platelets).

We present quantitative electron-paramagnetic resonance (EPR) measurements in conjunction with numerical device simulations that demonstrate the V_{oc} of poly-Si solar cells based on e-beam evaporation is limited by paramagnetic defects in the absorber bulk, which we assign to deep coordination defects, thereby ruling out the aforementioned possibilities and identifying the dominant source of device efficiency limitation. Grain size is used as a control to examine the impact of grain boundary and intra-grain imperfections on the material's electrical characteristics. Our findings indicate that the primary factor limiting the performance of poly-Si solar cells is the presence of paramagnetic defects in the absorber layer, such as DBs at grain boundaries or in dislocation cores (Figure 4.1).

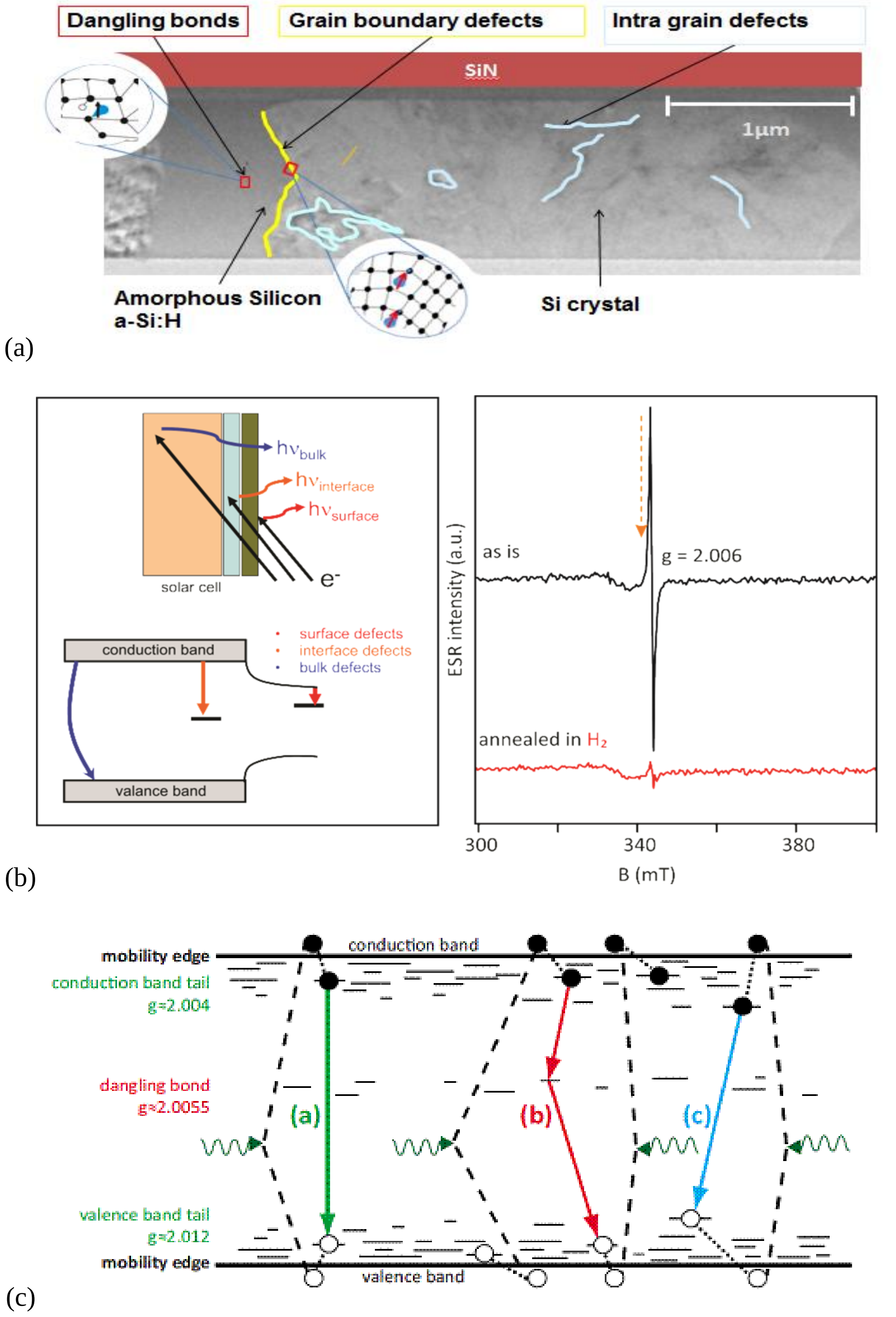

Figure 4.1. (a) Possible defects visualization in poly-Si layer, (b) healing of defects by hydrogenation, and (c) paramagnetic defect states in the bandgap

Possible defect centers in TOPCon solar cells:

i) P_b-type interface defect centers ($Si_3{\equiv}Si\bullet$): magnetic spin number S=1/2. It is a trivalent interfacial Si bounded to three Si atoms in the bulk (dot (•) symbolizes an unpaired electron in a dangling Si sp3 hybrid). These defects are known to compensate donor or conduction electrons in Si structures embedded in or surrounded by SiO_2.

ii) E′ type defect centers: generally related with the oxygen vacancies (deficiencies).

It is originated from electrically neutral Si dangling bond orbital which is closely coupled to a positively charged Si ($O_3{\equiv}Si\bullet$ + $Si{\equiv}O_3$). However, by light exposure neutral E′ center can also be created ($O_3{\equiv}Si\bullet$), as well.

iii) EX type defect centers: depend on the grown oxide thickness. This defect center consists of a hole delocalized over four oxygen dangling bonds at Si site.

4.2 Experimental Details

In an e-beam evaporation system, an electron beam heats the target material (Si). In addition to the e-beam evaporator, the system has effusion cells, one of which provides boron (B) doping (EC e-Beam system). A feature of this system is that effusion cells enable the direct addition of dopant vapor to the main flux of silicon beam. Changes in effusion cell temperature (1800 to 2000 °C) with a fixed Si deposition rate (1 Å/s) cause in the changes in the doping concentrations.

In this study, solid-phase crystallization (SPC) technique was applied, which is commonly used in many similar kinds of research of PV fabrication due to its ease of use, being contamination-free, and applicability for films with any thickness. SPC process depends on annealing time and duration. As known, crystallization of Si takes place at around 600 °C. SPC process could be prolonged annealing up to several hours to obtain the crystal formation at this critical temperature. First, for selecting the appropriate layer of polysilicon, a set of samples manufactured on thick silicon oxide layers. The fabricated 80 nm thick films on oxide-coated Si cell substrates are then further annealed at 600 °C for durations reached to 24 h to reach fully crystallized samples. We found that different doping concentrations resulted in different electrical properties. ToF-SIMS results give information about the passive value of the doping level. The active carrier concentrations were obtained from Hall Effect measurements. It is possible to apply the Tauc plot method to the absorption measurement of the UV-Vis measurements for these films and find the change (in this case increase) in the bandgap due to the increased boron concentration.

After selecting the desired doping level, correlated to the dopant amount, the number of spins (unpaired electrons) were analyzed by EPR. Then, we prepared samples with the same amount of doping and with different annealing temperatures (600, 700, 800 and 900 °C) and characterized their physical properties as sheet resistance to obtain an applicable emitter layer of poly-Si for the use of TOPCon cells.

As the amount of concentration and region of crystallization temperature fixed, it is time to apply the poly-Si layer on a structure of a cell structure. For this purpose, 4 inches, 200 µm, double side polished, two ohm.cm, n & p-type Cz- Si wafers were employed as the substrate. After RCA-1 and RCA-2 cleaning steps, single side phosphorous doping was obtained by $POCl_3$ diffusion at 940 ^oC, protecting the other side by a PECVD coated SiN_x layer. Following the post diffusion cleaning steps, both hot temperature nitric acid oxidation (NAOS) and dry oxidation at 800 ^oC were applied, resulting in 1-1.2 nm thick wet chemical oxide and 3-4 nm thick dry oxide layers, respectively. The reference samples were kept with RCA oxide till a-Si layer deposition and exposed to short HF dip prior to deposition. The deposition of the films was carried out at a high vacuum level of 10^{-7} Torr. For this part of the study again, 80 nm, highly doped, p-type a-Si layers were deposited. The passive dopant concentration of layers was already measured by using a calibrated ToF-SIMS system. Crystallization of the deposited amorphous films requires additional thermal treatment to obtain solid phase crystallization (SPC). For this study, annealing was done for one hour in tubular furnaces under N_2 at various temperatures of 800, 850, 900, and 950 °C.

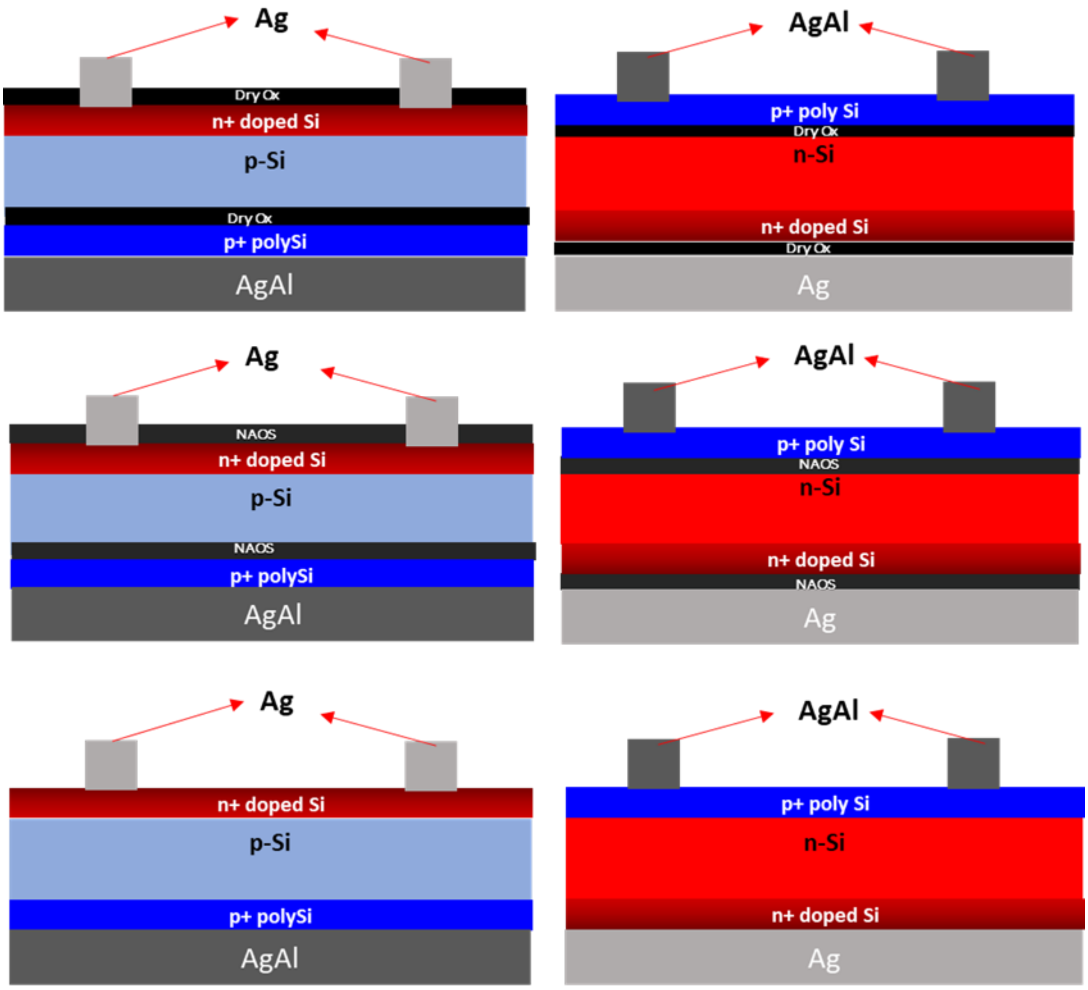

Figure 4.2. Structure of the cells with p-poly-Si as BSF at the back of p-type Si (left) and as emitter on n-type Si (right)

Annealing at high temperature converted p-type a-Si layers into p-poly-Si layers, which could then be applied for passivating contact cell structure. The performance of the obtained poly-Si layers was examined both on emitter (at the front side of n-Si) and BSF (at rear side p-Si) regions (Figure 4.2).

4.3 Results and Discussion

As the first step results, we found that different doping concentrations resulted in different electrical properties. ToF-SIMS results give information about the passive value of the doping level (Figure 3.2). The active carrier concentrations were obtained from Hall Effect measurements (Table 4.1). These results suggest that boron doped sample with effusion cell temperature of 2000 °C contain relatively more active dopant.

Table 4.1 Passive boron concentration measured by ToF-SIMS and active concentration/mobility calculated from Hall-Effect measurement

Sample	T_{efc} (°C)	Passive Dopant Conc. (Atom/cm^3)	Active Dopant Conc. (Atom/cm^3)	μ (cm^2/V.s)
B1800	1800	2.2×10^{19}	4.84×10^{18}	2.36E+00
B1900	1900	8.1×10^{19}	3.64×10^{19}	1.57E+01
B2000	2000	3.1×10^{20}	8.36×10^{19}	1.47E+01

As these layers planned to use as emitter layers, Tauc plot method (Figure 4.3) were applied to the absorption data of the UV-Vis measurements for these films and increase in the band gap were observed due to the increase boron concentration. In order to obtain an optimized emitter layer, further investigations applied to sample which doped by 2000 °C of effusion cell.

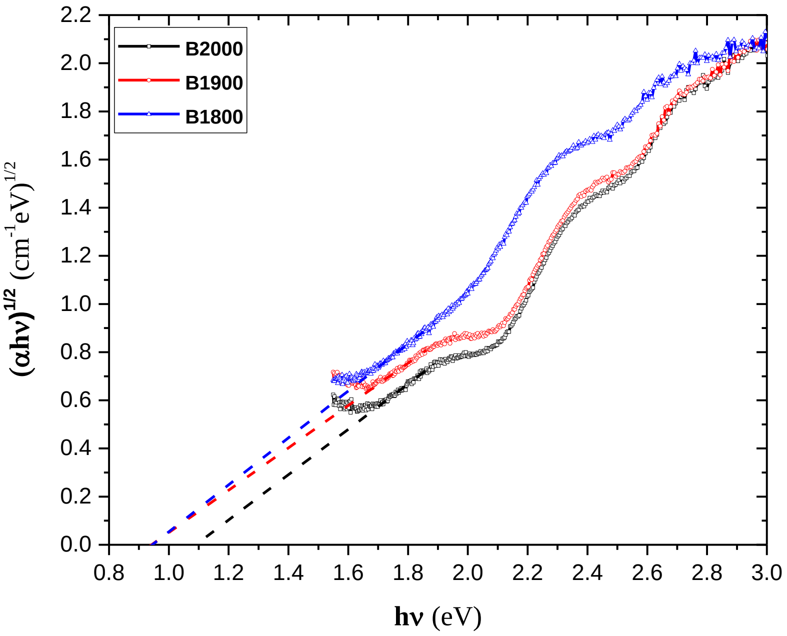

Figure 4.3. Tauc Plot for band gap measurements of the samples with different concentration of boron doping

B2000 samples were chosen for the following measurements since they show properties with the most effectively doped sample of this set and could be act as effective emitter or BSF layer for the cells. Correlated to active dopant amount of Hall-Effect measurements, we analyzed the number of spins (unpaired electrons) by means of electron paramagnetic resonance (EPR) spectroscopy. X-band EPR spectrum was measured for intrinsic poly-crystalline Si sample, 2000 °C boron doped (semi)poly-crystalline Si sample and 2000 °C boron doped poly-crystalline Si sample (Figure 4.4).

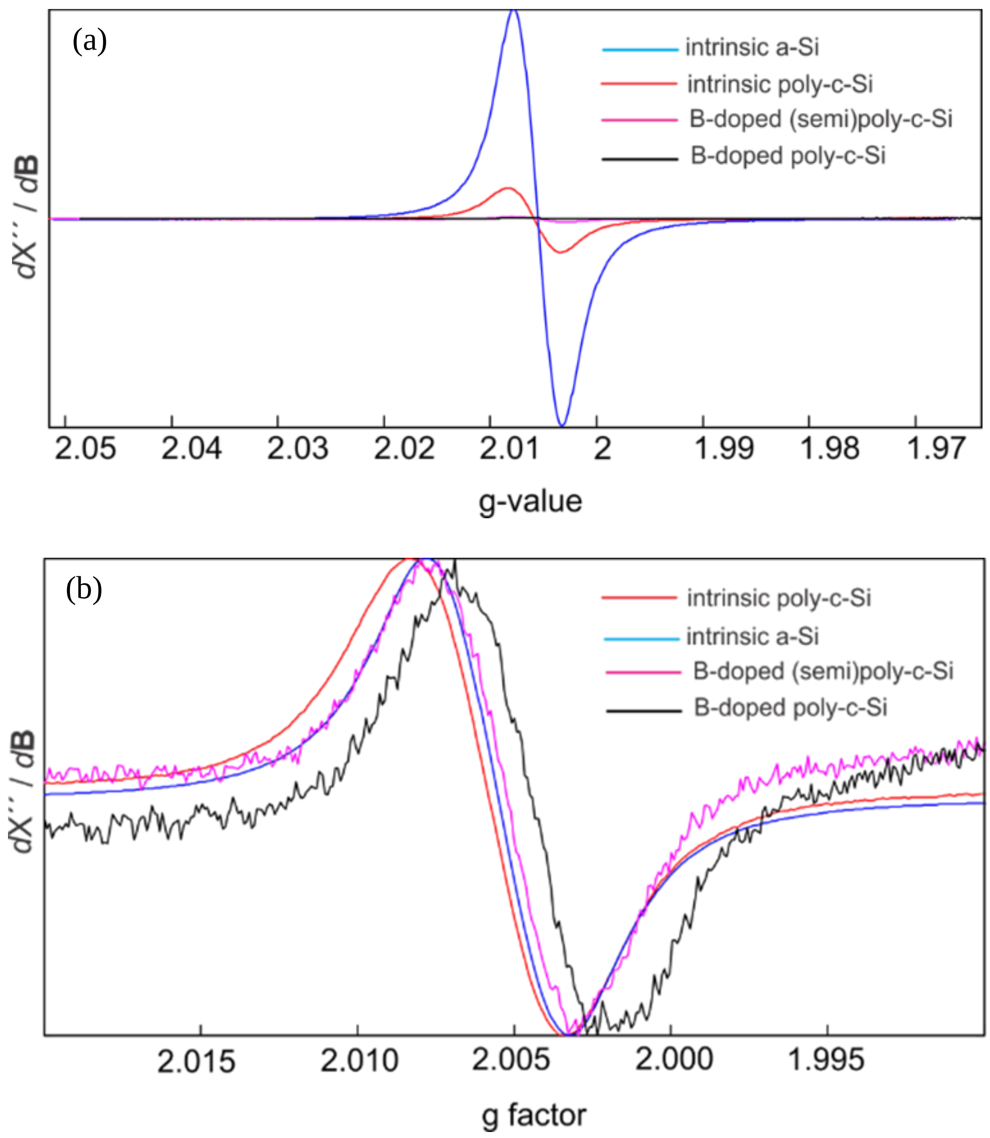

Figure 4.4. a) X-band CW ESR spectra of intrinsic (without any doping) amorphous Si reference sample (blue), B-doped a-Si (red), boron-doped (semi)poly-crystalline Si (pink), and boron-doped poly-crystalline Si sample (black) measured at 10K. b) Normalized spectra of the data.

It is clearly seen that the intensity of the signal decreases drastically while going from the amorphous phase to the crystalline phase; finally, the sample that is heated for the longest gives the least number of spins, i.e., less number of defect centers. The quantitative spin counting is presented in Table 4.2. The abbreviation “semi” poly-Si stands for those samples that are waited ca. half as long as the poly-Si samples. The decrease in the number of spins also holds, when one compares the semi poly-Si vs. poly-Si samples, i.e., 1.7 x 10^{18} vs. 0.3 x 10^{18}, respectively (Table 4.2).

Table 4.2. The number of spins obtained from ESR for the intrinsic and boron-doped Si samples. Color codes given in the table correspond to the colors used in Figure 4.4.

Si samples thin films	Number of spins/cm^3 from ESR
Blue: intrinsic a-Si	258.8 x 10^{18}
Red: B-doped a-Si	21.1 x 10^{18}
Pink: B-doped semi poly-c-Si	1.7 x 10^{18}
Black: B-doped poly-c-Si	0.3 x 10^{18}

Moreover, to understand the origin of the defects, we survey different MW energies on the detected G value (Figure 4.5). X-band CW EPR spectra of 2000 °C boron-doped samples were measured. The lowest intensity signals measured at a microwave power of 2mW, highest at 10mW. Typical signs for the defect center, which can be attributed to the dangling bonds in the interface of Si-SiO_2 is observed. Upon increasing the MW power stepwise from 2mW to 10mW, the signal intensity increased, supporting the *no-saturation-like behavior*, and suggesting the defect centers originate from a delocalized environment, i.e., closer to a *"free" electron near the conduction band*.

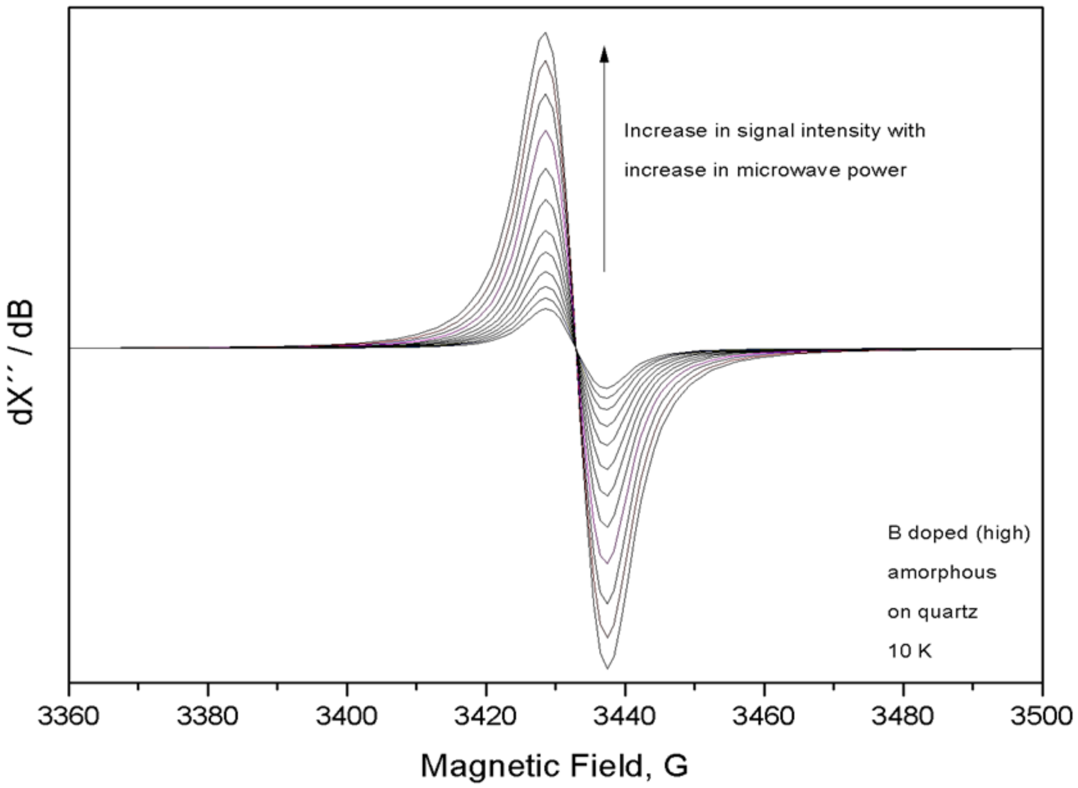

Figure 4.5. Survey of different MW energies on the detected G value to understand the origin of the defects

It has been found that reducing the number of spins is essential to reach an emitter layer with a lower amount of defects [86], such as dangling bonds that is directly correlated with the number of spins obtained from EPR. Hence, higher annealing processes should be applied in order to obtain an optimized emitter layer. Moreover, resistivity changes for the B2000 sample prepared by various durations of annealing temperatures were investigated. The sheet resistance of these samples was obtained from four-point probe measurements by averaging five measurements. As shown in Figure 4.6, a shorter duration of annealing in higher temperatures result in increased electrical conductivity of these emitter layers.

ESR enables one to have a better understanding about the crucial changes in the electronic structure. The change in the g-value (from 2.006 to 2.005, for quartz and SiN_x coated glass, respectively) suggests slight changes in the change in the electronic structure around the defect centres. In the next period of the project the effect of this change in the efficiency will be tested.

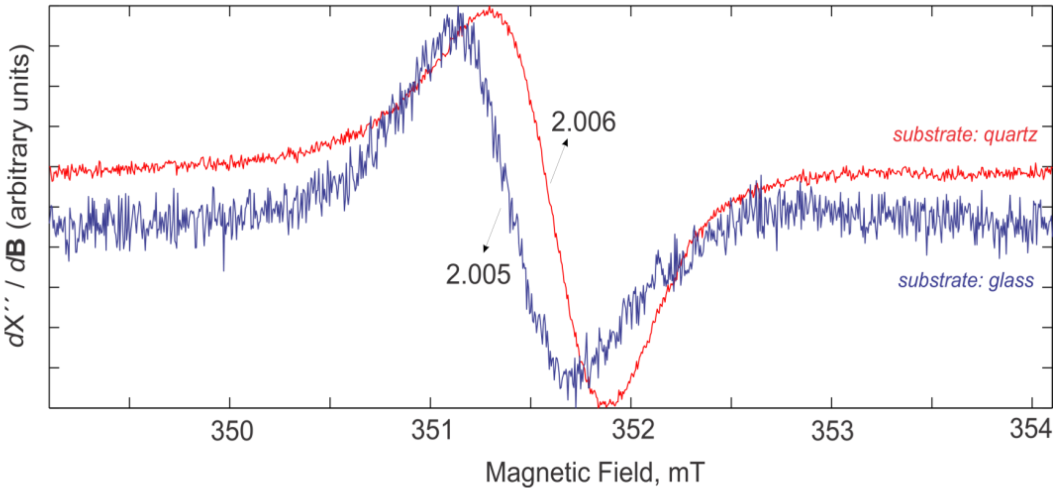

Figure 4.6. X-band CW ESR spectra of ^{11}B doped solar cells prepared at 1800°C with a thickness of 180 nm on quartz (red) and on glass (blue).

Moreover, the crystallization conditions are also examined in a detailed way. All the crystallization fraction revealed from Raman spectroscopy for the amorphous, semi-crystallized and fully crystallized samples (Figure 4.7). The crystallinity values and other important parameters of these samples gathered in Table 4.3.

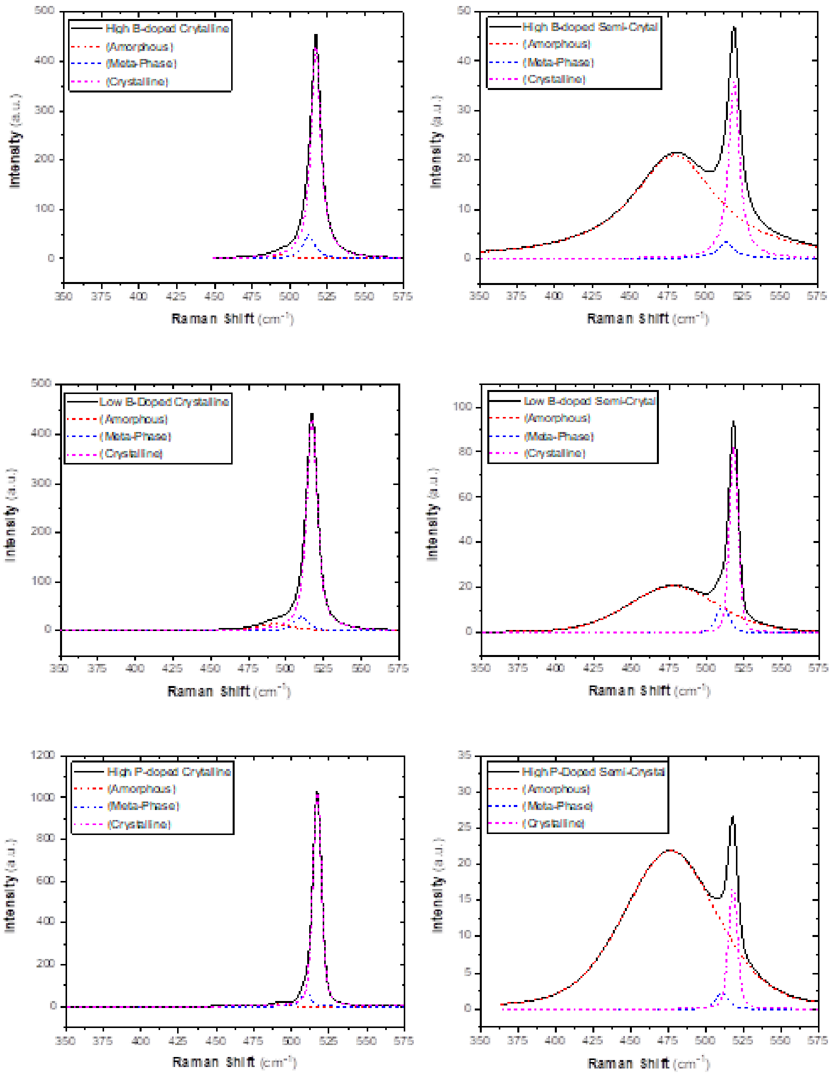

Figure 4.7. Crystallization fraction revealed from Raman spectroscopy for the amorphous, semi-crystallized and fully crystallized samples

It is well-known that, for intrinsic samples, i.e. without any ^{11}B or ^{31}P doping, majority of the defects are originating from Si dangling bonds which manifest itself with a resonant signal at around g = 2.0055 - 2.007. After doping with ^{11}B, a similar feature with g = 2.006 is observed in the case of a polycrystalline sample which is heated at 1700 °C.

Table 4.3. Doping and crystallinity amount of samples prepared for EPR investigation.

Sample	**Dopant**	**Si Deposition Rate (Å/s)**	**Thickness (nm)**	**Effusion Cell Temp. (˚C)**	**Passive Dopant Average Concentration (Atom/cm^{-3}) [Through SIMS]**	**Crystallinity (%)**
High Boron Doped	Boron (B)	5	1000	2000	2.9 e 19	Amorphous (**0%**)
						Semi-Crystal. (**65%**)
						Crystalline (**99%**)
Low Boron Doped	Boron (B)	5	1000	1800	1.2 e 18	Amorphous (**0%**)
						Semi-Crystal. (**32%**)
						Crystalline (**92%**)
High Phosphorous Doped	Phosphorous (P)	5	1000	850	4.7 e 21	Amorphous (**0%**)
						Semi-Crystal. (**8%**)
						Crystalline (**99%**)

The g-values depend on several factors: sample prepareation conditons, sample history, and material structure. Thus, there is a superposition of dangling bonds in different surroundings and this leads most often to asymmetric resonance signals (with a linewidth of 7-10 G). In addition to the asymmety of the signal, for a sample which was close to the microcrystalline growth, we have observed an additional relatively sharp (line width of ca. 1 G) signal which can be attributed to impurities (originating from e.g. ^{13}C nuclei) in the sample which hinder the crystallization. This fact could be analyezed with e.g. ^{13}C ENDOR, HYSCORE experiments.

Defect centres, in general, act as recombination centres for excess charge carriers. Understanding their location with respect to the band gap energies is essential to have a well-defined control on the improvement of the efficiency of Si solar cells. Spin-lattice relaxation time (T_1) of an unpaired electron (in this context a defect centre) gives information about its immediate surrounding. One way to have information about T_1 relaxation time is to measure the absorption signal under varying microwave power. If the signal intensity decreases upon increase in MW power (saturation), this indicates that the system is relaxing slowly, and the total magnetization cannot be fully recovered during the course of the signal accumulation. Whereas, in case of an increase upon increase in MW power (no saturation), the unpaired electron is relaxing fast enough that the total magnetization is recovered. A "bounded"/localized electron would behave like the former type, while a "free"/delocalized electron like the latter.

As a reference measurement, the X-band CW ESR spectra were recorded for an intrinsic sample, i.e. without any ^{11}B or ^{31}P doping. As presented in Figure 4.8 the typical signal for the defect centre which can be attributed to the dangling bonds in the interface of Si-SiO_2 is observed. Upon increasing the MW power stepwise from 2mW to 10mW, the signal intensity increased, supporting the *no-saturation-like behaviour*, and suggesting a *delocalized electron*.

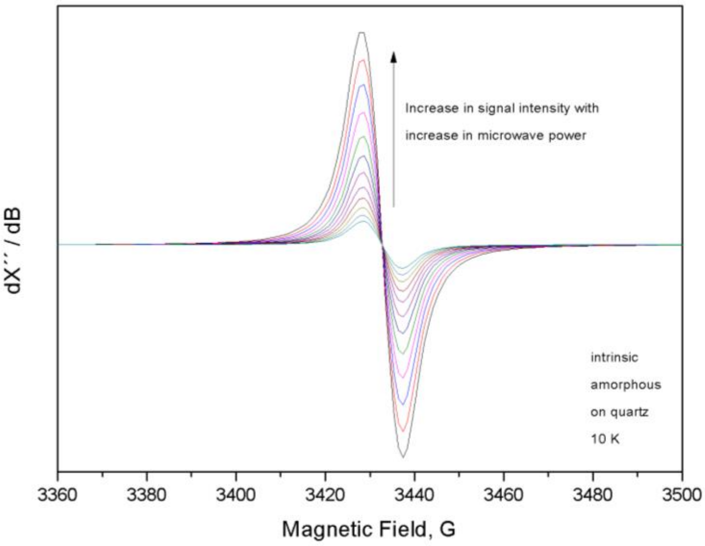

Figure 4.8. X-band CW ESR spectra of intrinsic amorphous Si solar cell sample grown to a thickness of 1μm on quartz (Sample thickness is increased to 1μm in order to increase the number of spins which can be observed with ESR). Lowest intensity signal measured at a microwave power of 2mW, highest at 10mW.

As shown inFigure 4.9, both for boron and phosphorous doped amorphous Si solar cells, the X-band CW ESR spectra reveal a similar behaviour of defect centres upon increase in microwave from 2mW to 10mW. Hence, in both cases, the unpaired electrons, representing the defect centres, originate from a delocalized environment, i.e. more closer to a *"free" electron near the conduction band*.

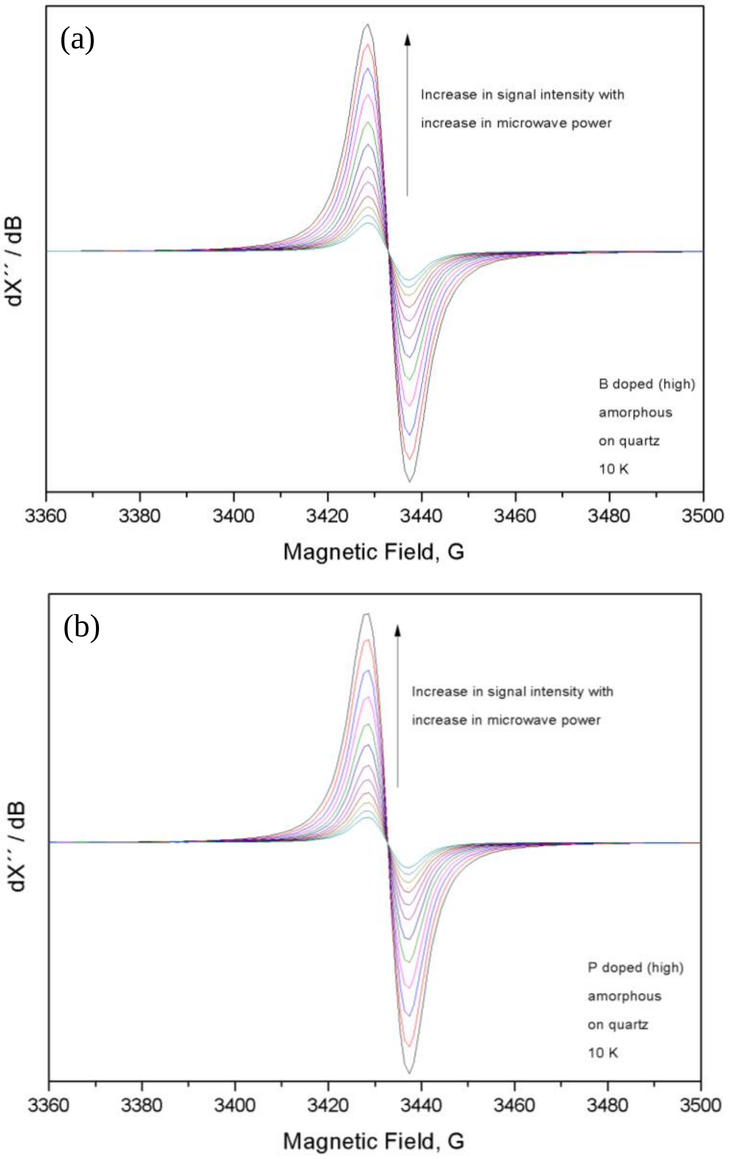

Figure 4.9. X-band CW ESR spectra of (a)boron and (b)phosphorous doped amorphous Si solar cell samples grown to a thickness of 1µm on quartz. In both cases the lowest intensity signals measured at a microwave power of 2mW, highest at 10mW.

The doping level was also correlated with an increase in the ESR signal intensity without having any change in the g-value (Figure 4.10). This indicates that the level of doping doesn't change the electronic structure of the solar cell. Only in the case of the highly doped phosphorous samples, the saturation behaviour is achieved at lower microwave powers (already at 5-6 mW). This can be due to different size and/or electronic properties of phosphorous as compared to boron. The latter fact has be considered and investigated in a detailed manner in the coming period of the project.

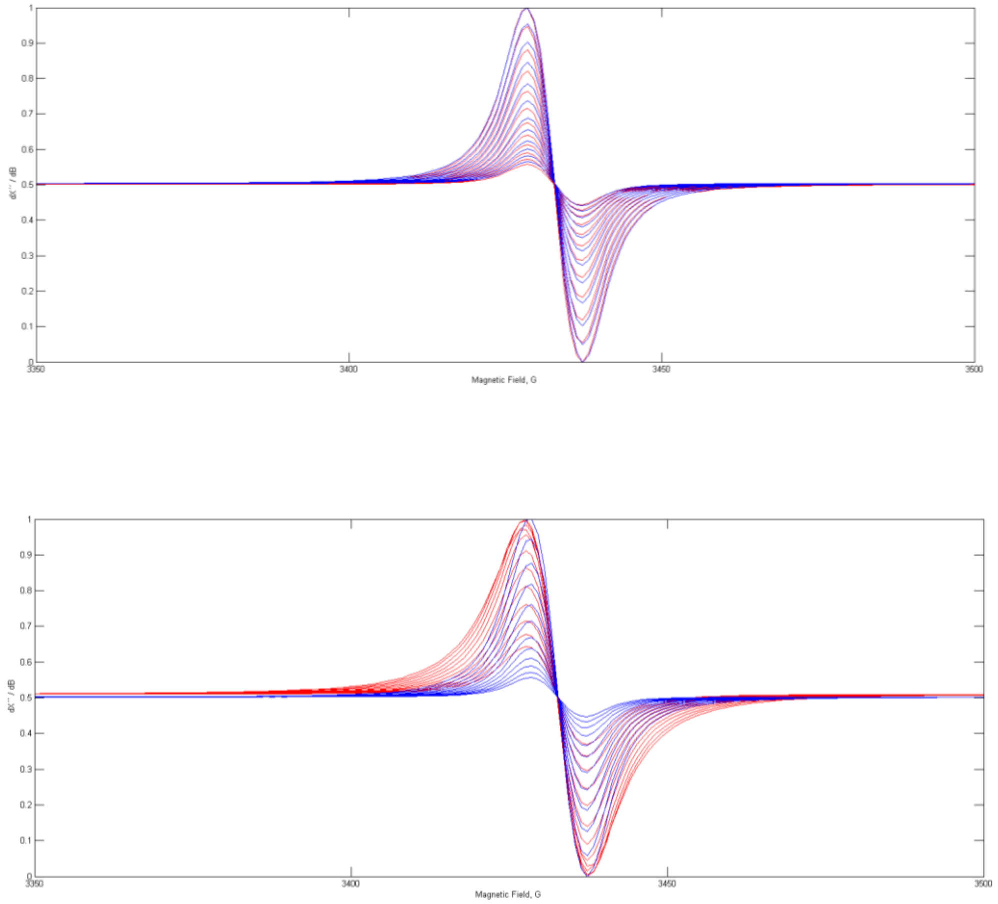

Figure 4.10. X-band CW ESR spectra of boron (red, less doped; blue highly doped) and below phosphorous (blue, less doped; red highly doped) amorphous Si solar cell samples grown to a thinckness of 1μm on quartz. In both cases the signal intensity increases upon increase in microwave power from 2 mW to 10 mW.

Dangling bond defects are possibly located at the Si-SiO_2 interfaces, crystalline regions, the grain boundaries, or they are in connection with the impurity atoms such as oxygen. When the solar cell is doped with boron or phosphorous not only these atoms substitute the Si atoms but also they replace the oxygens and thereby they repair the defect centres and some of the defect density might change upon doping and this might have an influence on the efficiency of the solar cell.

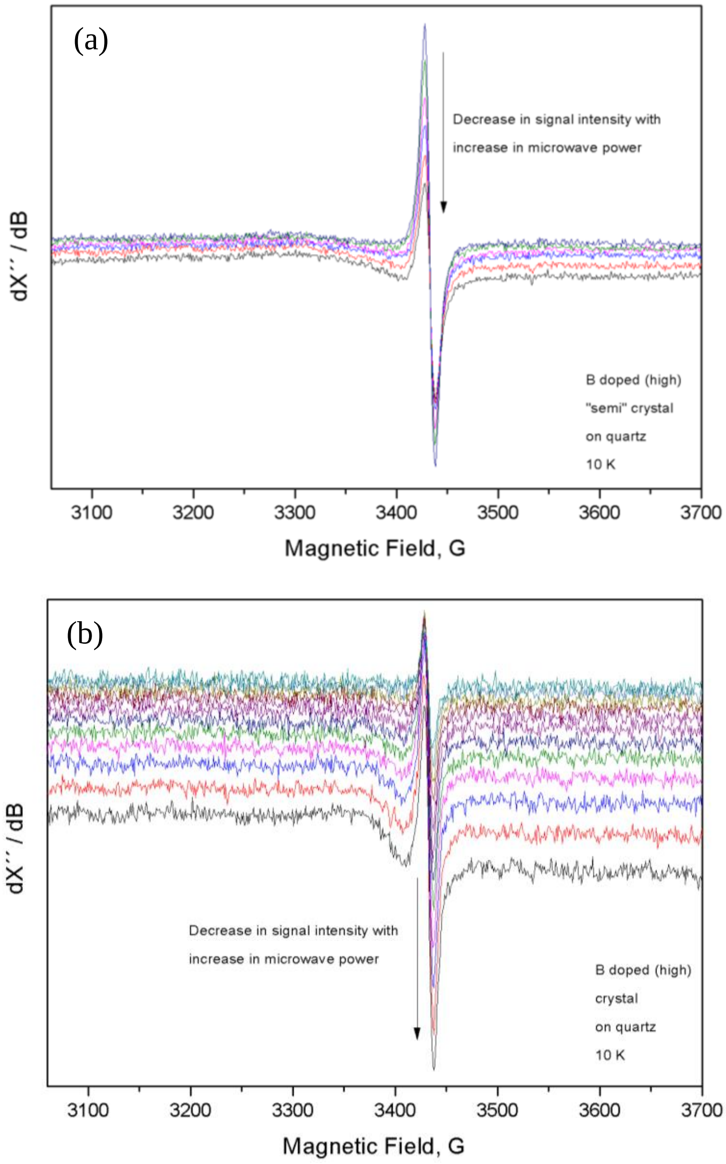

Figure 4.11. X-band CW ESR spectra of (a) low, and (b) high boron doped polycrystalline Si solar cell samples grown to a thinckness of 1µm on quartz. In both cases the highest intensity signals measured at a microwave power of 2mW, lowest at 10mW.

Not only the doping (level) but also a transition from amorphous to crystalline growth has to be considered while constructing solar cells. The above mentioned ^{11}B and ^{31}P doped samples were heated further for 3days and the corresponding X-band CW ESR spectra are shown in Figure 4.11 for boron doped (high and low) crystalline samples and in Figure 4.12 for phosphorous doped polycrystalline sample. When the doping level was increased step wise for the boron doped samples, it was observed that the main signal from the dangling bond defects (at $g = 2.087$) correspondingly decreases and a broader additional signal intensity (at $g = 2.064$) is increasing. As discussed above, presumably upon crystallization the dangling bonds are decreasing and correspondingly the signal at $g = 2.087$ is decreasing, and vacancies are appearing which is reflected in the increase in the signal at $g = 2.064$. Interestingly, the defect centres which are attributed to these ESR signals have a different nature compared to the ones introduced above for the corresponding amorphous samples: Upon increase in microwave power, the intensity of these signals decrease. As discussed above, this kind of behaviour is associated with a saturation-like behaviour of the unpaired electron, i.e. *localized/vacancy related electron near the valance band*.

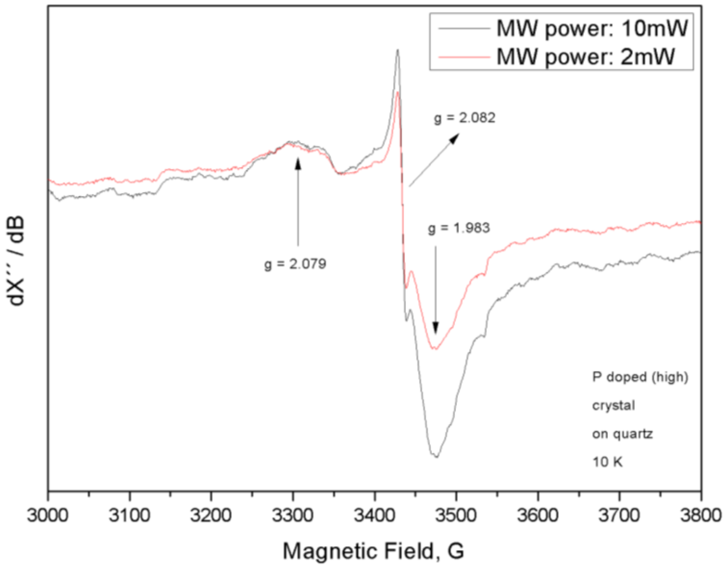

Figure 4.12. X-band CW ESR spectra of phosphorous doped polycrystalline Si solar cell samples grown to a thinckness of 1μm on quartz. Measured at a microwave power of 10 mW (blue) and 2 mW (red).

For the case of phosphorous doped samples, however, there is one more signal resolved at g = 1.983 which also possesses a saturation-like behaviour upon change in power, hence, slowly relaxing. This signal, presumably, correspond to a so-called EX type defect center which is usually observed around g-values around g = 2, and the defect centre consists of a hole delocalized over four oxygen dangling bonds at the Si site.

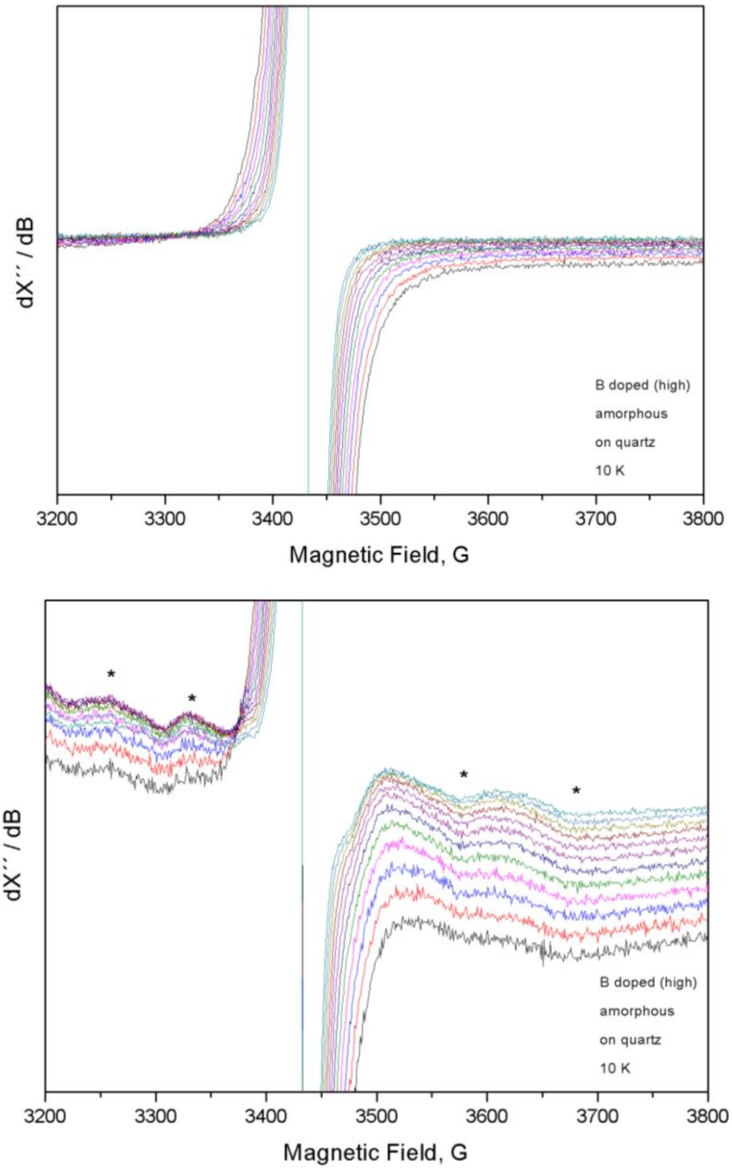

Figure 4.13. X-band CW ESR spectra of boron doped polycrystalline Si solar cell samples grown to a thinckness of 1µm on quartz (left) and glass (right). In both cases the lowest intensity signals measured at a microwave power of 2mW, highest at 10mW.

The effect of three different defects in the boron doped poly-Si layer (Figure 4.13) was also simulated to find the portion of each defect type in the layer. As shown in Figure 4.14, additional of the g values related to the three defect center are appearing in the case of samples grown. The assigned signals are relatively sharp and they are separated evenly from each other which might indicate hyperfine splitting corresponding to a hyperfine interaction of a nucleus with the unpaired electron at the defect centre.

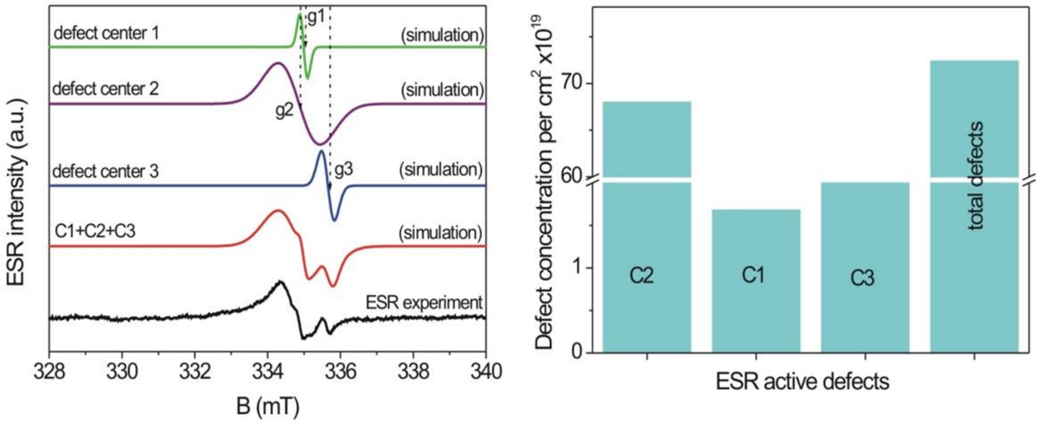

Figure 4.14: X-band spectrum of boron doped poly-Si thin film measured at 4 K and simulation of each defect center.

In order to understand the nature of this nucleus (identification of the nucleus and its interaction strength and influence on the efficiency), pulsed ESR experiments, e.g. ESEEM and double resonance experiments, e.g. ENDOR could be performed, which is out of focus of this dessertation.

Overall, it was observed that upon transition from amorphous to crystallization of both boron and phosphorous doped Si solar cell samples, the nature of the defect centres changes from a delocalized-like electron (with fast relaxation) to localized-like electron (with slow relaxation) behaviour. In the next period of the project, more effort will be given in understanding the correlation between this change in the defect nature and efficiency of the solar cells.

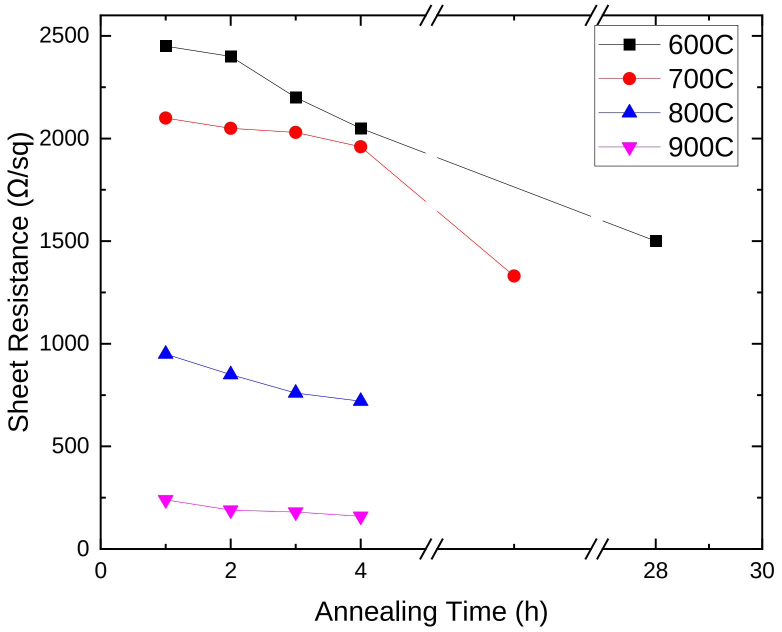

Figure 4.15. The sheet resistance of the different annealing durations and temperature for sample B2000 for the fulfilment of SPC with a lower amount of defects

From this result, we fix the crystallization temperatures for the values higher than 800 °C and fabricate new layers for the structures of the passivated contact cells described on Figure 1. For these cells, implied V_{oc} (iV_{oc}) values of the samples were measured using Sinton-WCT 120 after each process steps on half-fabricated cell structures. As shown in Figure 4.15, crystallization has a positive effect on most of the p-doped layers deposited on n-type substrates regardless of the interfacial layer between the Si substrate and poly-Si layer on top. Right after the crystallization step, samples with wet chemical oxide had higher iV_{oc} values compared to samples with a dry oxide layer. Crystallization at 950 ^oC had a negative or minimal effect on surface passivation with iV_{oc} values of 630 mV and 610 mV for dry oxide and wet chemical oxide, respectively. Additional hydrogenation at 400 ^oC improved iV_{oc} for all samples. Additionally, symmetrically deposited SiN_x layer on both sides of the samples increased iV_{oc} by 5-10 mV for both types of oxide layers. Based on these results, we can deduce that crystallization at temperatures up to 900 °C followed by a subsequent hydrogenation process and SiN_x capping give reasonably good passivation quality with iV_{oc} of 670-675 mV.

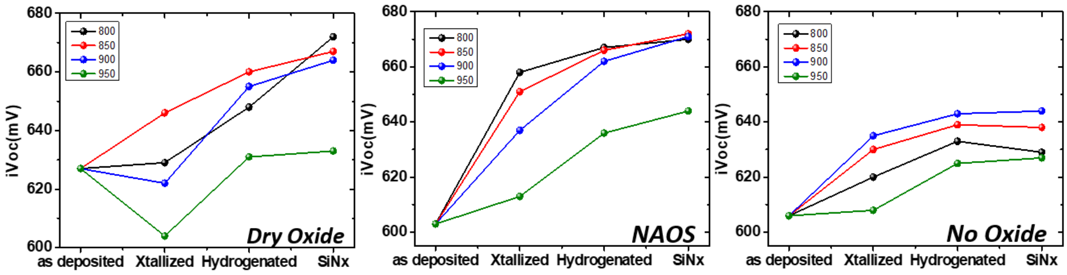

Figure 4.16. Implied V_{oc} values through each step of process for p-type poly-Si on the n-type wafer with dry oxide (left), wet chemical oxide (middle) and without oxide layer (right).

The behavior of the iV_{oc} for p-type substrates was different than it was for n-type substrates (Figure 4.16). Crystallization of the deposited layers degraded iV_{oc} for all temperatures with a more pronounced drop for temperatures above 850 °C. This drop could be related to degradation of bulk lifetime of p -type wafers at high process temperatures. For p-type substrates (Figure 4.17) where p-poly-Si layer was used as BSF region, samples with dry oxide had better performance with a maximum iV_{oc} of 680 mV which was 660 mV for wet chemical oxide case. Moreover, sheet resistance was traced both for $POCl_3$ diffused and p-poly-Si deposited surfaces as a function of crystallization temperature. For both wafer polarities sheet resistance of the $POCl_3$ diffused side reduced from 40 down to 10 Ω/□ as a function of increasing temperature. For p-poly-Si on n-Si, sheet resistance was around 10 Ω/□ and on p-Si, it reduced from 250 down to 25 Ω/□.

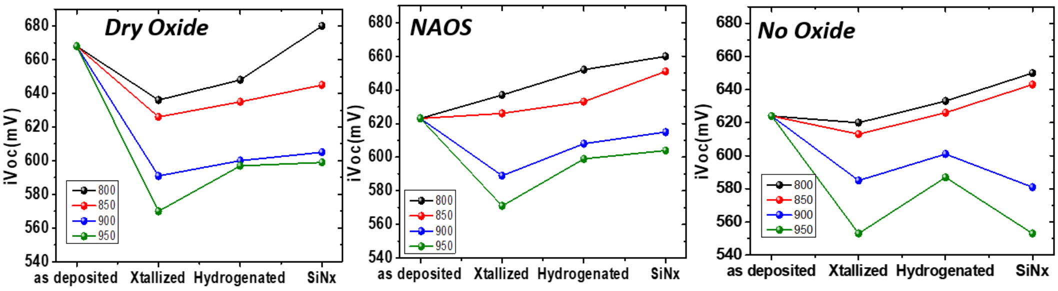

Figure 4.17. Implied V_{oc} values through each step of the process for p-type poly-Si on the p-type wafer with dry oxide (left), wet chemical oxide (middle), and without oxide layer (right).

To understand the defects limiting V_{oc} values EPR measurements applied to the samples. Charge carriers play important role in defect structures and the carrier transport behavior of the whole system. The significant shift in g-factor of n and p type substrates indicates that both substrates have point defects with different electronic environment thus the symmetry. The most symmetric crystal is expected to give g-factors around the similar value of free electrons (g_e=2.0023) which gives the most significant contribution to the electronic conductivity. Thus one can take the g_e value as reference and depending on the spin-orbit coupling the electrons will shielded from the magnetic field this shielding will cause deviations from the free electron values either larger or lower magnetic field positions. Since we have here a typical S=1/2 system such deviations are too small but thanks to high sensitivity of EPR Nano EMX system that we can observe clear shift with respect to n- and p- type substrate as g= 2.004 and 1.99, respectively (Figure 4.18).

In this step of research, the n-type substrate has been used as the substrate of the different configurations. Nevertheless the p-type poly Si will be also applied on the substrate as emitter layer of the potentially designed passivated contact solar cell device.

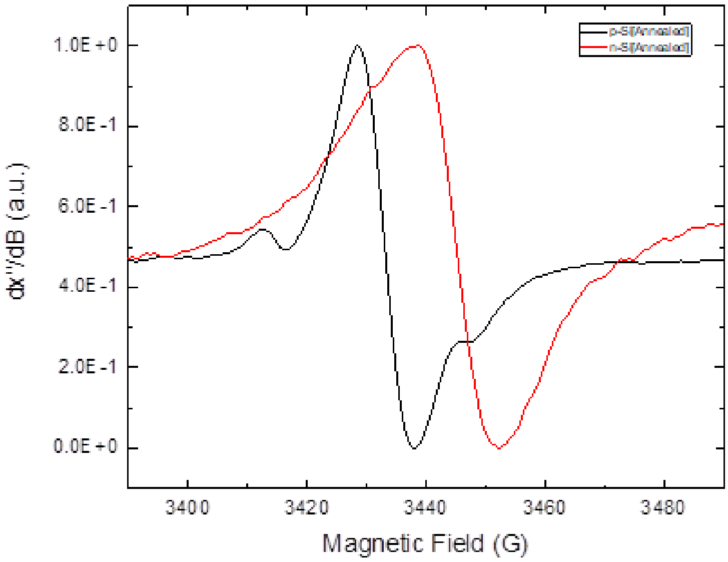

Figure 4.18. Magnetic field position shift with respect to n- and p- type substrate as g= 2.004 and 1.99, respectively

In order to increase the kinetic energy of charge carries back surface field (BSF) has been employed at the back side of the absorber layer. In this work this is n-type substrate. Thus whether the BSF application changes the defect structures or not could be safely understood and can be controlled. From Figure 4.19 one can get following useful information for the substrate processing of the solar devices. From the bare n-type substrate it is necessary to monitor the defect evolution by the heat treatment. For BSF procedure such heat treatment is necessary for the P atoms to enter the substrate for the formation of such back field. Thus we first heat the bare substrate to observe the heating effects then we do the similar test by the existence of $POCl_3$ gas. Consequently it was observed from EPR that the defect concentration (observed via peak-to-peak intensity) is decreasing by the heat treatment. This means heat somewhat heal the defects in the system. Moreover by the BSF procedure it is possible that more P atoms incorporate or substitute with Si atoms increased number of P atoms either substitutional or interstitial will reveal even P-hyperfine lines visible in EPR spectra as can be seen in Figure 4.19.

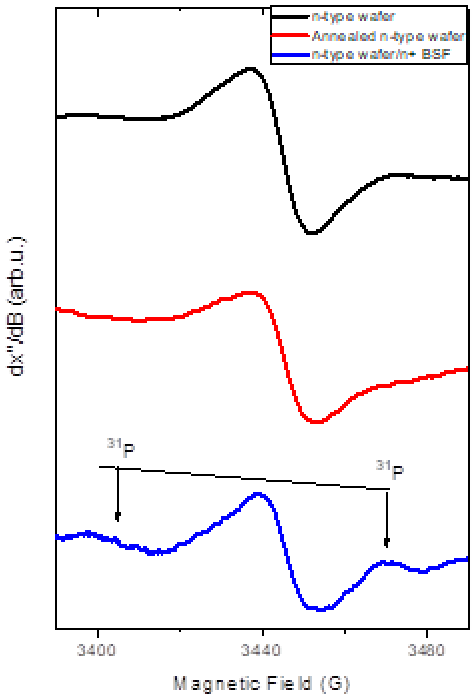

Figure 4.19. N-type substrate the effect of annealing and n+ doping for BSF to trace P-hyperfine

Here at this stage three different designs were proposed to correlate the V_{oc} values of defect structures. Therefore, the first aim was to measure via EPR the signal of defect structures and compare the EPR analysis results with the obtained electrical V_{oc} ones. Wet oxide, dry oxide interfaces were deposited on the n-type substrate as well as one design was implemented without any oxide. Thus, the effect of dry and wet oxides was tested (Figure 4.20). The designed cells were also given at the side of the EPR plot in details.

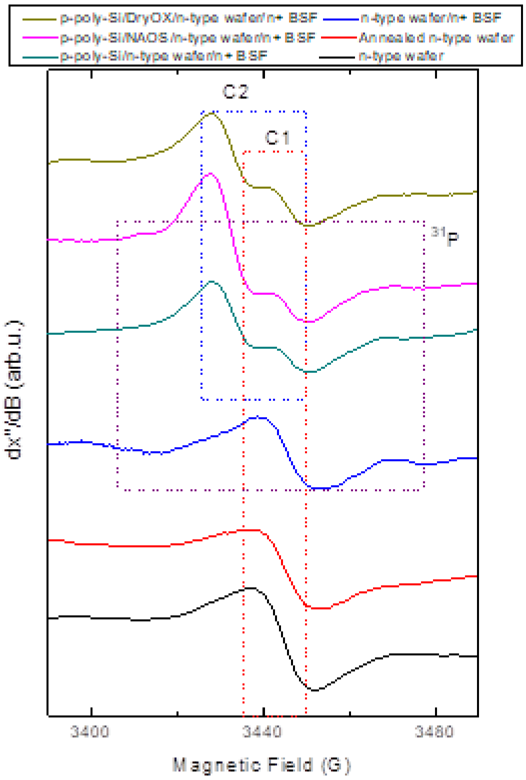

Figure 4.20. Effect of different oxide types on the paramagnetic defects detetected by EPR.

Figure 4.20 covers all three devices including the comparison with the substrate. This careful EPR experiment shows how the defects created at every stage of the solar cell device production. By this one may extensive control and understanding of not only the roles of such defect but also get further information on the electrical properties that are related with the point defects. Following useful information can be gathered from this EPR experiment.

Table 4.4. Comparison of g-factors of different samples.

	g-factor (n-type)	**g-factor (p-type)**	**Ip-p /a.u.**
n-type substrate	1.9997	-	30

n-type substrate annealed at 850 °C, 1 h, under N_2	1.9997	-	24
n-type substrate with n+BSF	1.9997	-	16
F2 (p-poly Si on n-type substrate with n+BSF)	1.9993	2.0060	27
D2 (p-poly Si with dry oxide interface on n-type substrate with n+BSF)	1.9996	2.0064	32
E2 (p-poly Si with wet (NAOS) oxide interface on n-type substrate with n+BSF)	1.9994	2.0067	43
p-type substrate annealed at 850 °C, 1 h, under N_2	-	2.0067	100

At first glance addition of p-poly Si (F2) on the processed substrate remarkably changes the shape of the EPR spectra. As it is seen from the Figure 4.20 that an additional EPR active center at around g~2 is appeared (Table 4.4). This signal can be attributed to the p-type Si-related bulk defects. This g-factor value is also consistent with the p-type substrate. On the other hand, the effect of oxide interface is highly complicated to understand via X-band EPR spectrometer due to the following reasons. The g-anisotropy and the broadening and the overlap all of the possible defects somehow hinders the main information that can be extracted from the EPR spectra. Nevertheless the slight intensity changes indicates that the extensive defect healing is can possible via addition of wet or dry oxides. Moreover when the lower field region of the spectra is magnified (see inset, find g-factor as well) there is a third defect center arises which stem from the structural point defects located at the interface. Overall such defect healing via BSF and oxide layer the electrical performance of the devices has been improved substantially.

Beyond the specific role of these three defects (which is out of scope for this step of the investigation) accumulation of the EPR data of n and p-type substrates with passivating oxide (Figure 4.21) show a finger-print of the acceptable defects for a TOPCon half fabricated cell with improving V_{oc}.

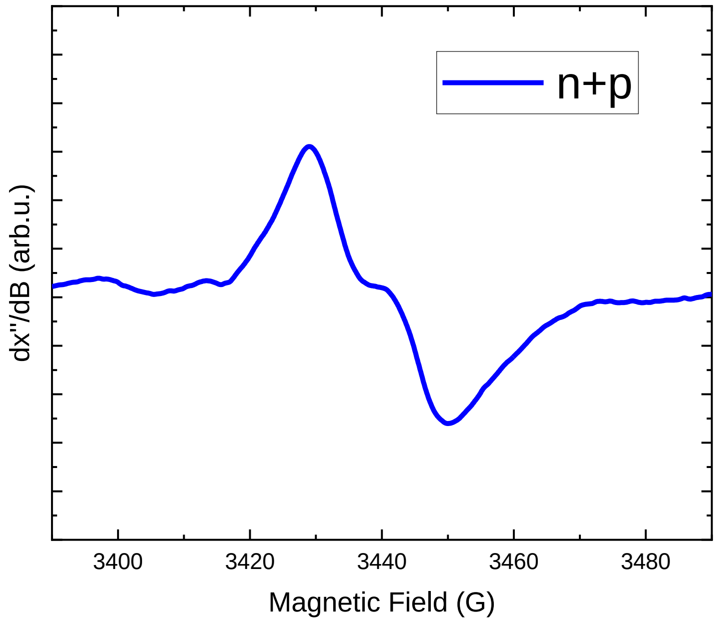

Figure 4.21. Accumulation of the EPR data of n and p-type substrates with passivating oxide.

Comparing this fingerprint with the half fabricated cells with different crystallization temperature present a good tendency with the sample with highest iV_{oc} (Figure 4.22)

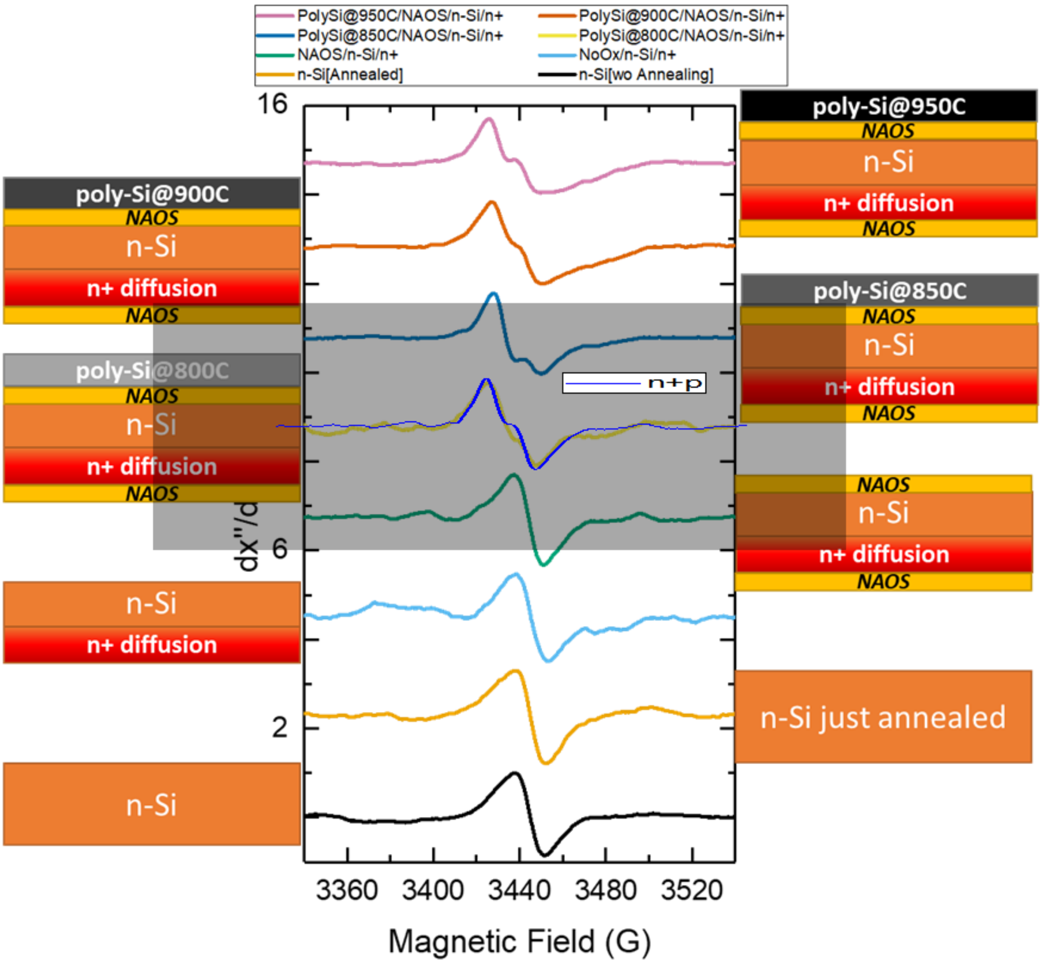

Figure 4.22. Comparing this fingerprint with the half fabricated cells with different crystallization temperature present a good tendency with the sample with highest iV_{oc}

As the final step, screen printing was applied with FT-Ag and FT-AgAl paste on $POCl_3$ diffused and p-poly-Si side respectively. Co-firing was carried out at 940 ^{o}C. Then, External quantum efficiency and current-voltage measurements were done for the contacted samples. When we check EQE results for p-poly-Si on p-Si, we can see that Annealing process beyond 800 °C drastically reduced EQE for p-poly-Si on p-type substrate (Figure 4.23(a)). While, EQE results for p-poly-Si on n-Si (Figure 4.23(b)) demonstrate annealing process beyond 900 °C drastically reduced EQE for n-type substrate and there is a significant loss in IR region for the samples annealed at 950 °C.

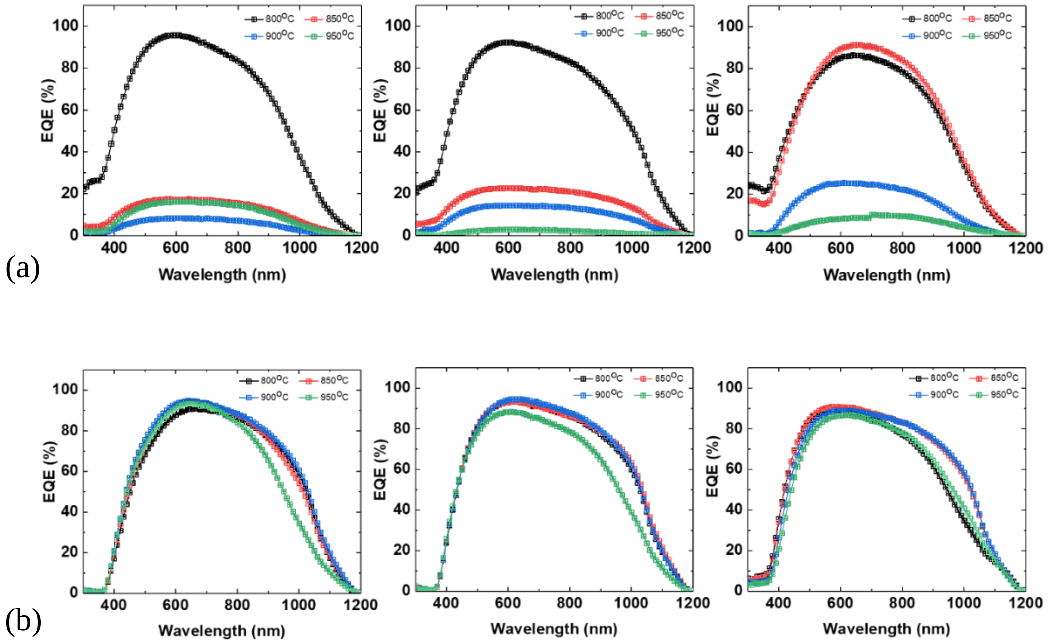

Figure 4.23. EQE for p-poly-Si crystallized at 800, 850, 900 and 950 °C a) as BSF at back of p-type Si and b) as emitter on n-type Si substrate

It is possible to calculate J_{sc} from the EQE results, which performed in Figure 4.24. Obviously, n-type substrates show better performance with higher amount of generated carriers for all samples compared to p-type substrate.

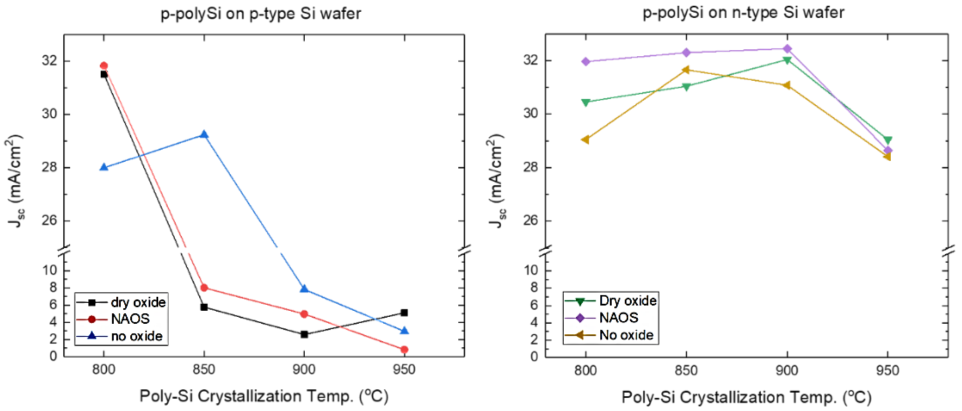

Figure 4.24. J_{sc} results calculated from EQE data for cells with p-poly-Si as BSF at the back of p-type Si (left) and as emitter on n-type Si (right)

Considering Figure 4.25, in comparing two different substrates with a crystallization temperature of 850 °C, p-poly-Si on an n-type substrate shows better performance for all samples compared to p-type substrate. Comparing p-poly-Si/SiO_x stack for dry oxide and NAOS cases, using p-poly-Si with NAOS significantly improves UV-response compared to dry oxide for n-type Si, which is observed for IR-response for p-type substrate since p-poly/SiO_x stack was used as BSF.

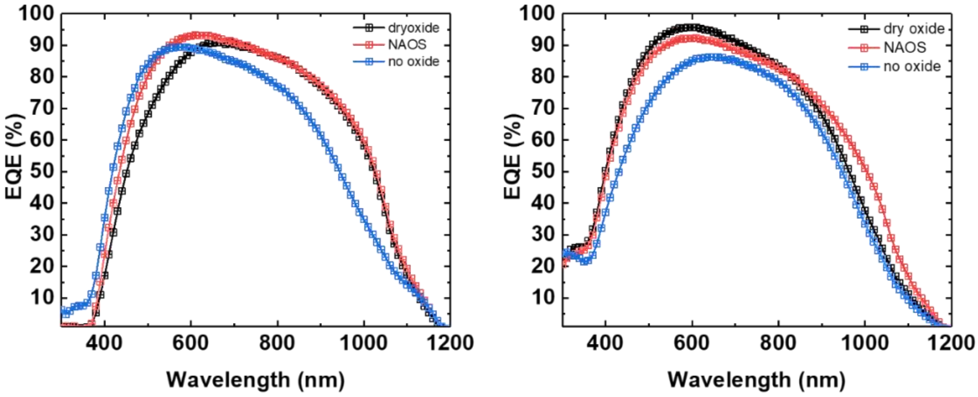

Figure 4.25. EQE for p-poly-Si crystallized at 850°C used as emitter on n-type Si (left) and as BSF at the back of p-type Si (right)

Considering I-V measurements (Figure 4.26), obtained FF values were poor (< 60 %) as expected since the substrates were polished wafers (which hard to make a sufficient contact attachment) and the highest efficiency value of the batch was ~ 10 %. The other samples with higher potential did not show any acceptable result, which could be explained by low adhesion of contact paste with poly-Si on a polished wafer.

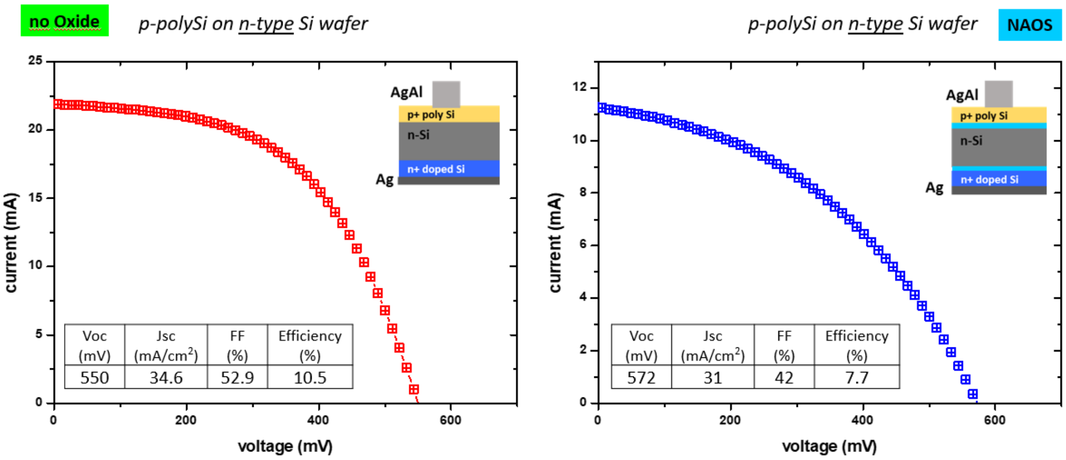

Voc (mV)	Jsc (mA/cm^2)	FF (%)	Efficiency (%)
550	34.6	52.9	10.5

Voc (mV)	Jsc (mA/cm^2)	FF (%)	Efficiency (%)
572	31	42	7.7

Figure 4.26. I-V measurements for two best-resulted cells of each substrate

SunsVoc measurements, along with V_{oc} values (Figure 4.27), revealed that pseudo efficiency values (Figure 4.28) could reach above 15%. Pseudo Efficiency resulted by applying J_{sc} calculated from EQE to V_{oc} measured by Sinton SunsVoc. For further improvement, optimized process parameters will be applied to textured samples. The thickness would be reduced to 50 nm to avoid recombination sites in the poly-Si layer.

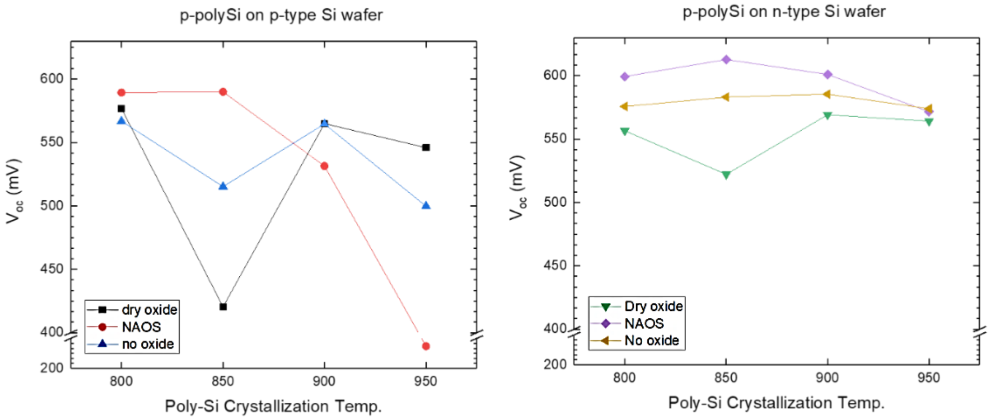

Figure 4.27. SunVoc cells with p-poly-Si as BSF at the back of p-type Si (left) and as emitter on n-type Si (right)

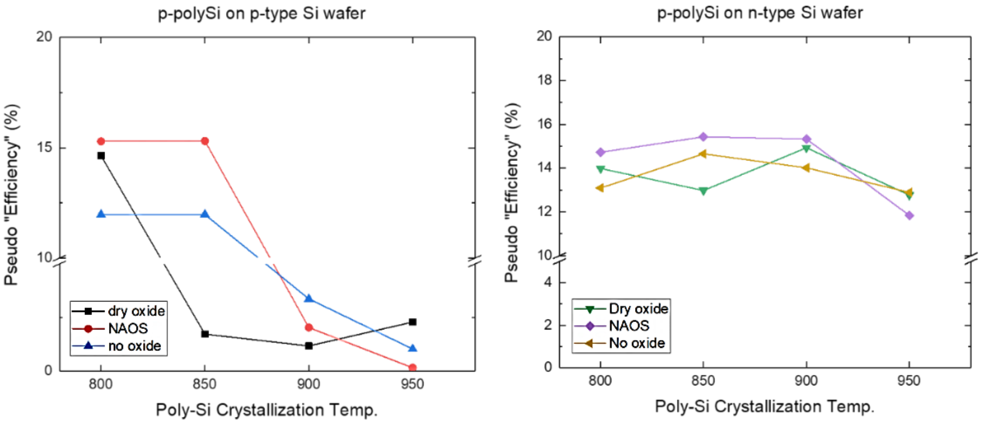

Figure 4.28. Pseudo efficiency cells with p-poly-Si as BSF at the back of p-type Si (left) and as emitter on n-type Si (right)

As presented in Figure 4.26. DSP wafers did not perform adequately in the first run due to contacting problems on polished surfaces. Also, we are not acquainted with proper firing process temperature of contact paste and related speed. Understanding the performance of single side p-poly-Si in the cell structure could be possible by finding favorable conditions for forming the contacts in the first place. The firing process should be applicable to both the emitter and the BSF side. Therefore, working with the bifacial cell could be enlightening to do a more efficient kind of cell. The structure of these cells is similar to the first set with dry oxide and NAOS (Figure 4.29).

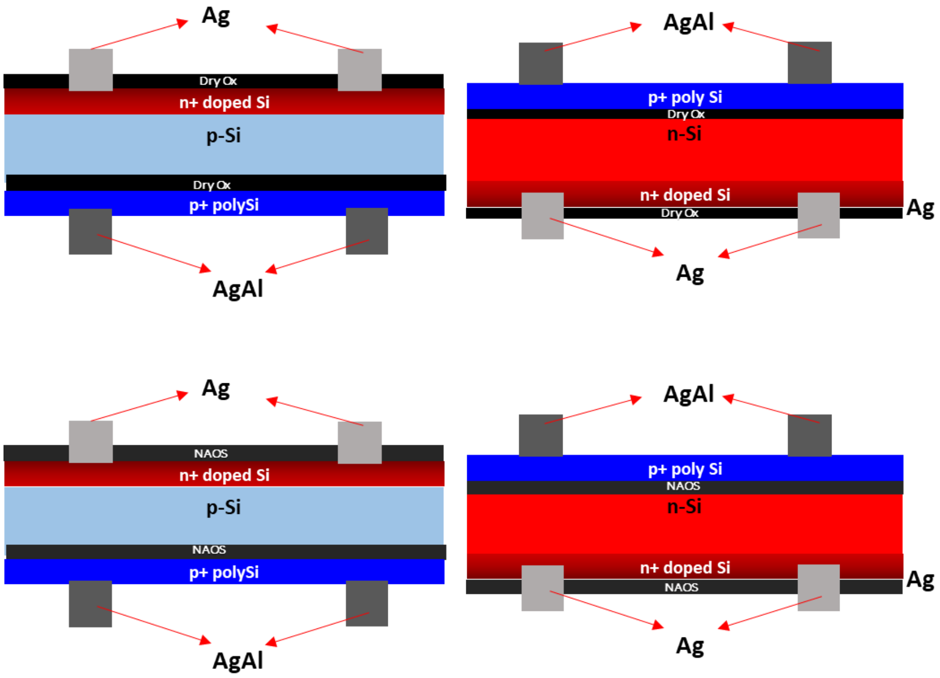

Figure 4.29. Structure of the cells with p-poly-Si as BSF at the back of p-type Si (left) and as emitter on n-type Si (right)

Furthermore, choosing textured surfaces could solve that problem and assist a better contact attachment. In this case, we must do investigate the performance of p-poly-Si on textured surfaces to choose the efficient recipe for poly-Si fabrication. As all the initial results of the first set presented temperatures below 900 °C should be investigated. As suggested above, we try 50 nm of poly-Si with crystallization temperatures of 800 and 850 °C. ToF-SIMS analysis of two selected samples show no visible SiO_x barrier, but boron leaked through the bulk (Figure 4.30). Higher crystallization temperature causes deeper boron diffusion, logically. Seen possible Carbon contamination could result in severe losses in cell performance.

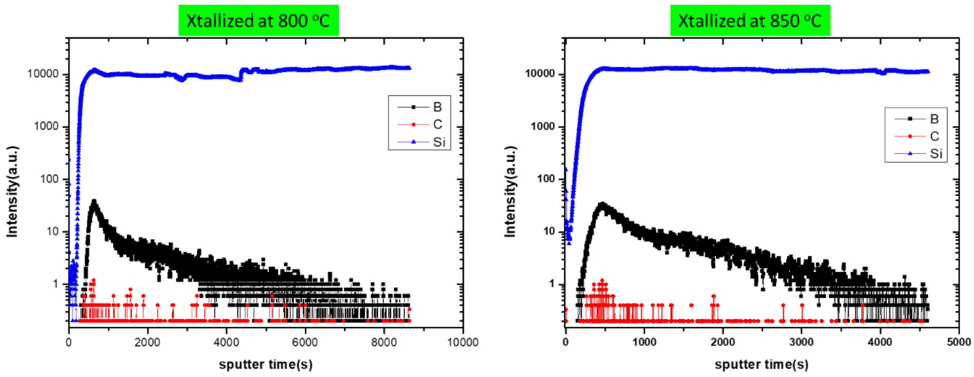

Figure 4.30. Boron diffusion of boron from p-poly-Si to the c-Si bulk by applying 800 and 850 °C.

For evaluating primary cell properties, photoluminescence (PL) mapping and four-point probe mapping could be useful (Figure 4.31). For obtaining textured surfaces, CZ 4” wafers had been processed from chosen n-type and p-type Si substrates. Single side POCl3 diffusion applied to samples to have emitter on p-wafer and BSF on n-wafer. On the other hand, p-poly-Si take the role of BSF and emitter in the opposite position of these samples, respectively. Figure 4.31 represents a deadly outcome for Dry Ox on n-Si for 850 °C, while Dry Ox on p-Si shows the best performance at the same process temperature.

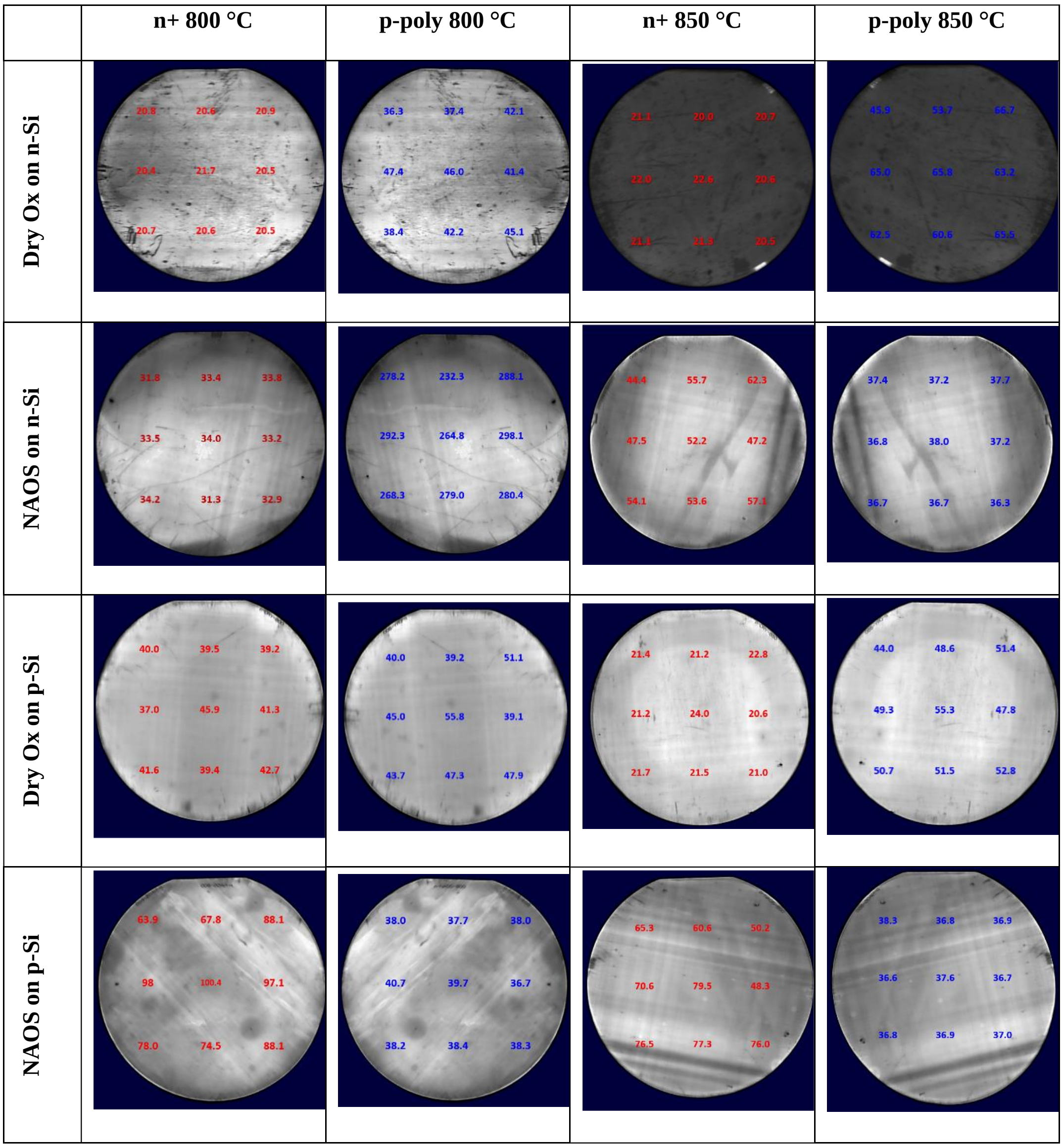

Figure 4.31. PL images and sheet resistance mappings of the dry Ox/Naos samples on n/p-type substrates with p-poly-Si on the opposite side

Industrial FT-Ag and FT-AgAl paste used for making the contacts. Firing optimization followed by a combination of three different firing temperatures (930, 940, and 950 °C) and two different conveyor belt speed (400 and 500 cmpm). Solar Cell Results in Figure 4.32 show the effect of crystallization temperature on the p-type substrate with dry oxide, which contains p-poly-Si crystallized at 800 °C with the means of efficiency and FF.

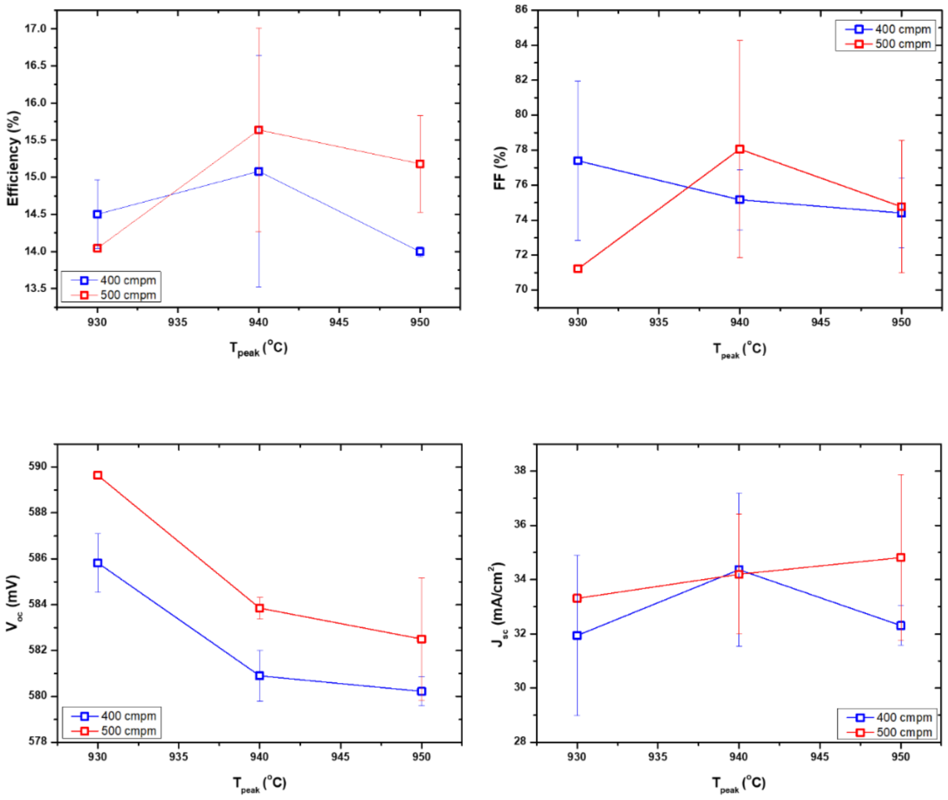

Figure 4.32. Cell properties of p-DRY-800 °C samples with different firing values.

The best cell shows the performance of additional efficiency of 18.04%, consisting of 16.2% for front contact and 2.3% from the back contact (which multiplied by 0.8 factor in total efficiency measurement) resulted from 800 °C crystallization temperature (Figure 4.33), which fired at 940 °C with 500cmpm. Moreover, samples activated at 850 °C were unfunctional (fired at 930 °C with 500 cmpm) with V_{oc} : 247 mV, J_{sc} : 4.1 mA/cm^2, FF: 39 and Efficiency < 1%.

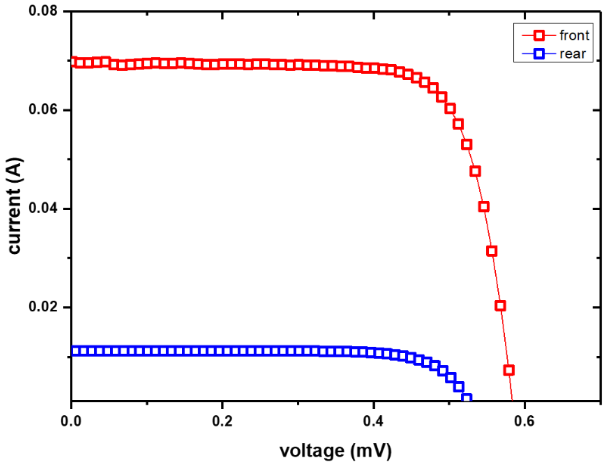

Samples
=> Xtallized at 800°C &
=> fired at 940 °C with 500 cmpm

Front side:
- Efficiency: 16.2 %
- FF: 76 %
- Voc : 584 mV
- Jsc : 36.2 mA/cm^2

Rear side:
- Efficiency: 2.3 %
- FF: 75.3 %
- Voc : 528 mV
- Jsc : 5.58 mA/cm^2

Figure 4.33. Best cell properties of the sample measured from I-V set-up solar simulator for p+ poly-Si-Dry Oxide/p-Si/n+ emitter structure.

In the set of samples with NAOS passivation on the p-type substrate, second-best results achieved for lower crystallization temperatures. The variation of the cell performance result presented in Figure 4.34.

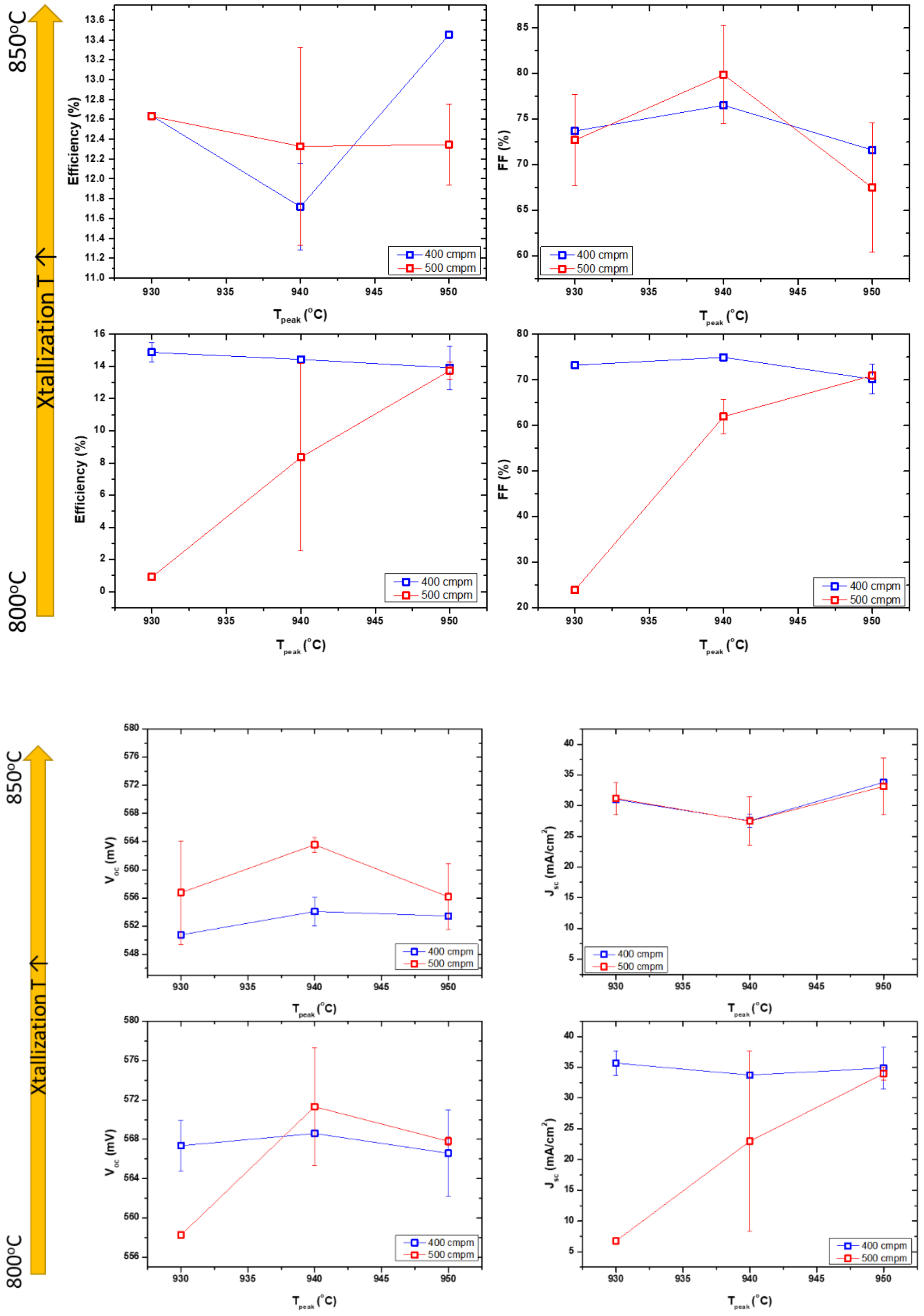

Figure 4.34. Cell properties of the samples on the p-type substrate with a NAOS passivating layer with different firing values.

The best cell performance of samples with NAOS on the p-type substrate shows additional efficiency of 16.75%, consisting of 15.07% for front contact and 2.1% from the back contact (multiplied to 0.8 correction factor) for p+ poly-Si-NAOS/p-Si/n+ emitter (Figure 4.35(a)). This outcome resulted from 800 °C crystallization temperature, which fired at 950 C with 400cmpm. Furthermore, in the case of 850 °C of crystallization with the same firing values, 15.1% efficiency from the front-side and 1.1% from the back-side (multiplied to 0.8 correction factor) perform the total 15.98% efficiency for the cell consisting p+ poly-Si-NAOS/p-Si/n+ emitter (Figure 4.35(b)).

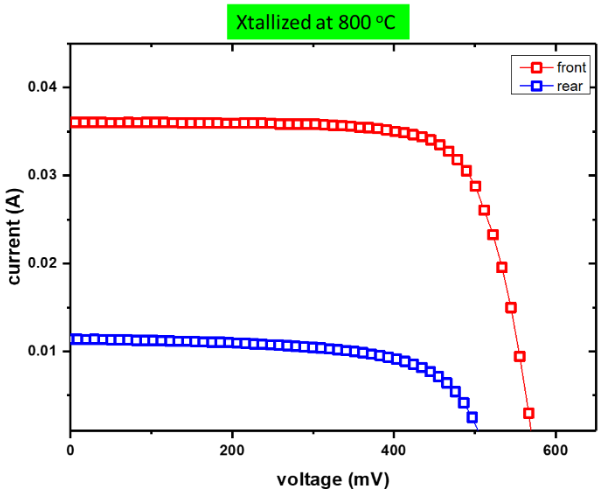

(a)

Samples
- => Xtallized at 800°C &
- => fired at 950 °C with 400 cmpm

Front side:
- Efficiency: 15.07 %
- FF: 74.5 %
- Voc : 570 mV
- Jsc : 35.3 mA/cm^2

Rear side:
- Efficiency: 2.1 %
- FF: 63.6 %
- Voc : 508 mV
- Jsc : 6.31 mA/cm^2

(b)

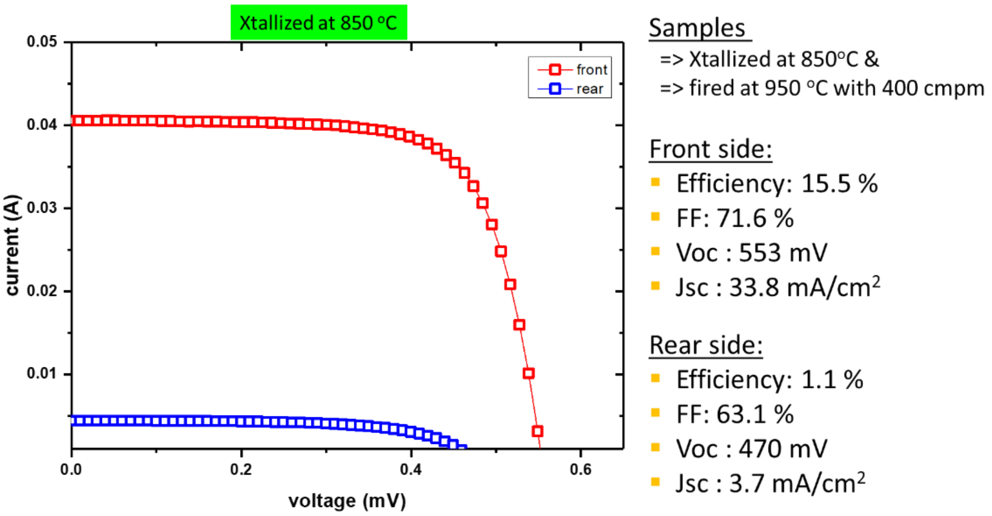

Samples
=> Xtallized at 850°C &
=> fired at 950 °C with 400 cmpm

Front side:
- Efficiency: 15.5 %
- FF: 71.6 %
- Voc : 553 mV
- Jsc : 33.8 mA/cm^2

Rear side:
- Efficiency: 1.1 %
- FF: 63.1 %
- Voc : 470 mV
- Jsc : 3.7 mA/cm^2

Figure 4.35. Best cell properties of the sample measured from I-V set-up solar simulator for a) p+ poly-Si-NAOS/p-Si/n+ emitter, and b) p+ poly-Si-NAOS/p-Si/n+ emitter, structures.

In the case of NAOS on the n-type substrate, results are generally with low photovoltaic values. Notably, the side of p-poly-Si showed more share of losses in the performance. In Figure 4.36 represents efficiency, FF, V_{oc}, and J_{sc} of the samples processed with NAOS no the n-type c-Si with various crystallization temperature of the p-poly-Si.

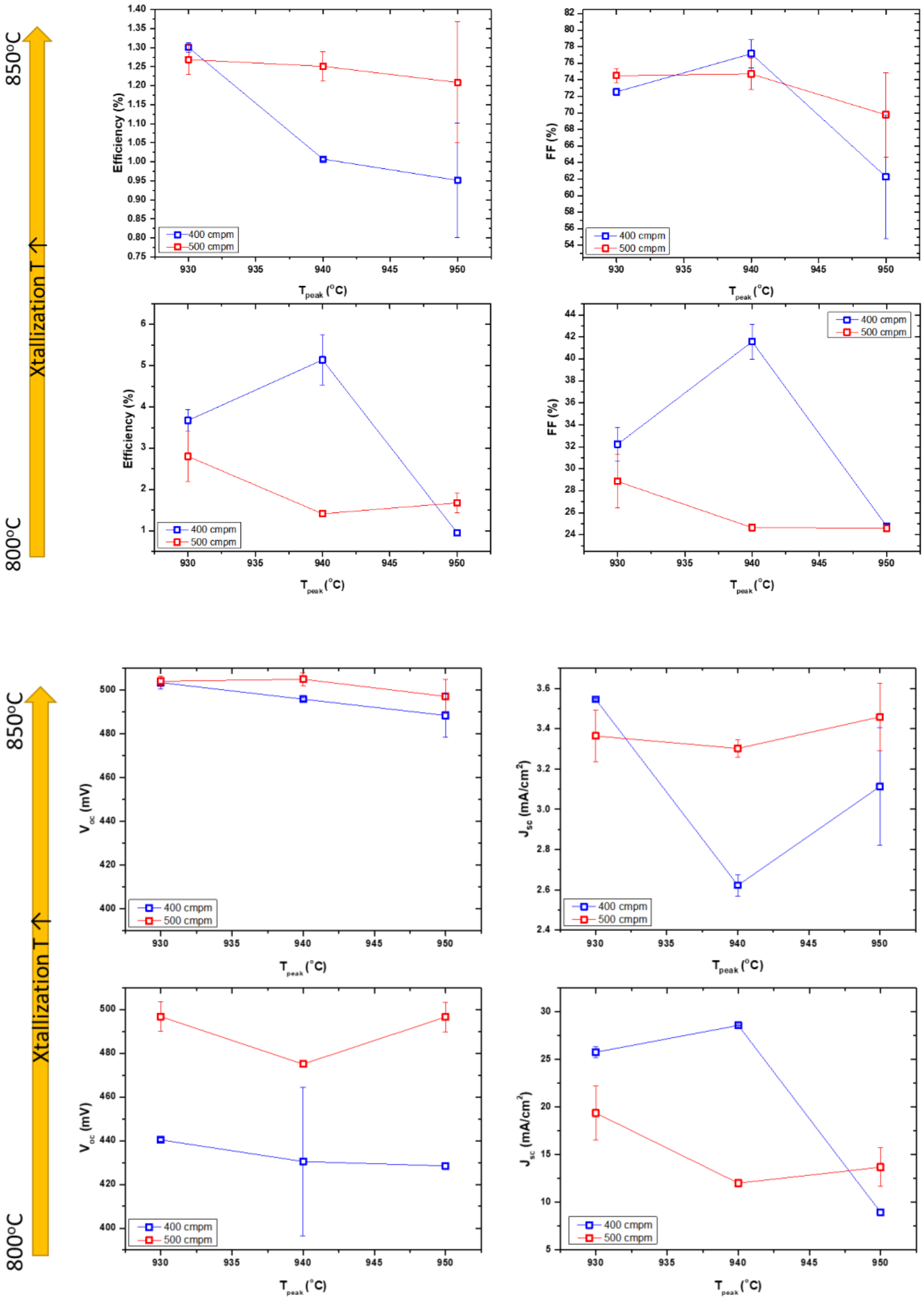

Figure 4.36. Cell properties of the samples on the n-type substrate with a dry oxide passivating layer with different firing values.

Highest values of cell performance for p-poly-Si emitter on the n-type substrate with NAOS passivation for crystallization at Figure 4.37(a) at 800 °C and (b)at 850 °C.

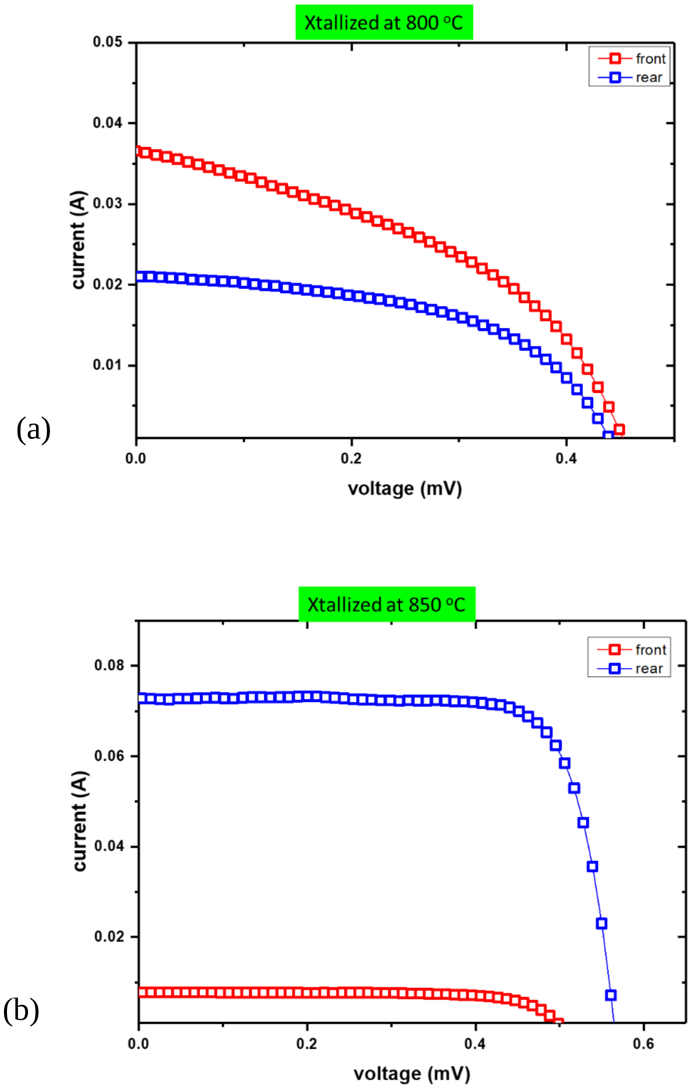

Samples
=> Xtallized at 800°C &
=> fired at 940 °C with 400 cmpm

Front side:
- Efficiency: 5.7 %
- FF: 42.7 %
- Voc : 454 mV
- Jsc : 28.6 mA/cm^2

Rear side:
- Efficiency: 3.8 %
- FF: 52.1 %
- Voc : 443 mV
- Jsc : 16.4 mA/cm^2

Samples
=> Xtallized at 850°C &
=> fired at 940 °C with 500 cmpm

Front side:
- Efficiency: 1.2 %
- FF: 73 %
- Voc : 501mV
- Jsc : 3.33 mA/cm^2

Rear side:
- Efficiency: 13.7 %
- FF: 77.4%
- Voc : 565 mV
- Jsc : 31.3 mA/cm^2

Figure 4.37. Highest values of cell performance for p-poly-Si emitter on the n-type substrate with NAOS passivation for crystallization at a) 800 °C and b)850 °C.

In Figure 4.38, we can see the effect of crystallization on the external quantum efficiency measurements. The results comparing the crystallization effect for a) p-poly-Si as BSF on p-Si with NAOS and DRY Ox, b) n-poly-Si as emitter on n-Si with NAOS and DRY Ox.

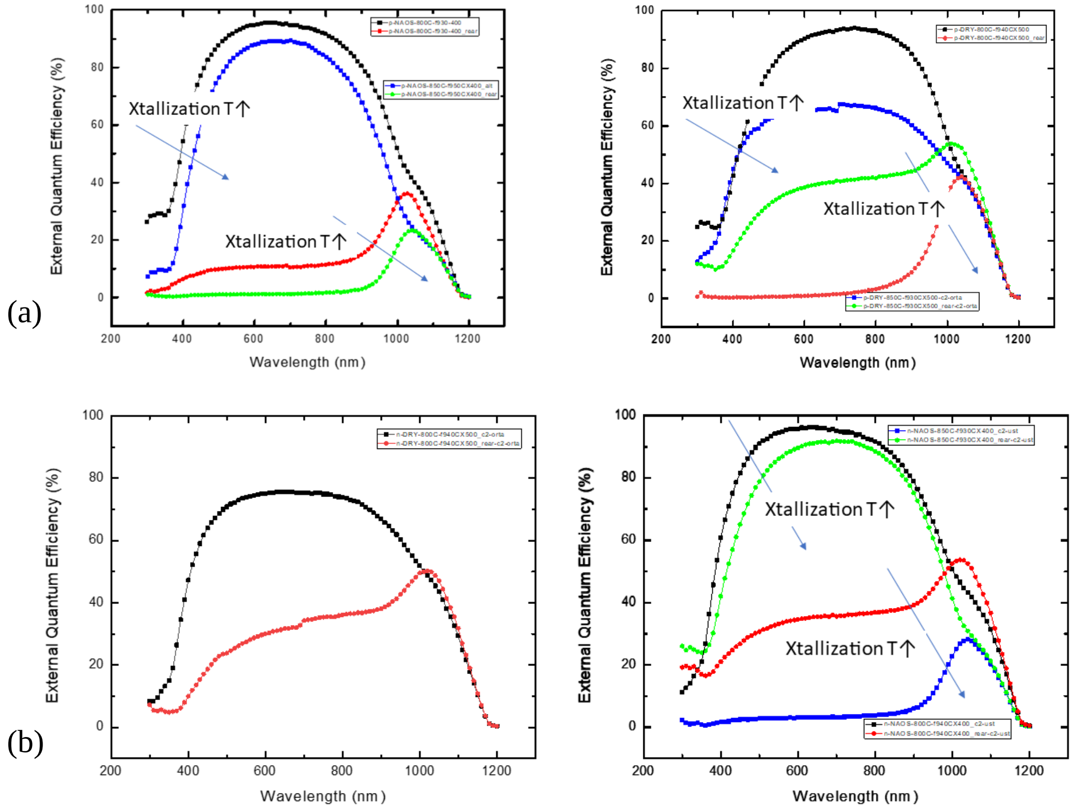

Figure 4.38. External quantum efficiency results for comparing the crystallization effect for a) p-polySi as BSF on p-Si with NAOS and DRY Ox, b) n-poly-Si as emitter on n-Si with NAOS and DRY Ox.

There are two primary outcomes from these results. On the one hand, for both NAOS and dry oxide passivating samples, increasing the temperature of the crystallization process reduces the cell performance. On the other hand, NAOS passivation presents better performance compared to dry oxidation.

CHAPTER 5

BIFACIAL PASSIVATING CONTACT (TOPCON) SOLAR CELLS WITH TRANSPARENT CONDUCTING OXIDE

5.1 Introduction

The heterojunction solar cell with intrinsic thin-film (HIT) features such contacts and a record efficiency of silicon based solar cells. However, this passivation scheme cannot withstand temperature above 250 °C and therefore requires a dedicated back-end processing like low-temperature TCO and metallization as Feldmann et al., presented at 2014. The promising concept of TOPCon (Tunnel Oxide Passivated Contact) solar cell technology could adopt the TCO layer as well.

As of now, it has been shown that following the sputtering deposition of ITO layers, the carrier lifetime of a-Si:H/c-Si heterojunctions drastically decreases. First, the ion bombardment from Argon plasma is the primary cause of this event. Ar^+ ions' kinetic energy is transmitted during the deposition process by striking the sample surface directly (Illiberi et al., 2011). Second, owing to the well-known Staebler-Wronski effect of a-Si:H, the a-Si:H layer is exposed to plasma luminescence, which is also responsible for the deterioration of the a-Si:H/c-Si interface (Wolf et al., 2011). Because of the high-energy ion bombardment of the poly-Si thin films used in TOPCon solar cells, it is also discovered that the TOPCon structure's passivation quality has decreased (Feldmann et al., 2014d).

Sputtering at room temperature and subsequent post-annealing are effective for the excellent passivation quality of a-Si thin films, according to investigations on ITO sputtering damage for a-Si thin films produced by PECVD (Zhang et al., 2011). The effects of sputtering damage on the TOPCon structure, however, have not yet been thoroughly investigated. Therefore, it is important to investigate how ITO sputtering affects the passivation property of both n-type and p-type TOPCon. The goal of this research is to determine if ITO deposition is responsible for the sputtering damage to different kinds of TOPCon structures. Additionally, by adjusting the ITO deposition settings and post-annealing conditions, the recovery of the passivation quality of TOPCon is investigated. Finally, our work revealed our primary experimental findings about the investigation of TOPCon solar cells' top and rear.

As mentioned, CVD techniques such as PECVD lead to a hydrogenated a-Si (a-Si:H) while PVD techniques such as e-beam evaporation result in an a-Si without hydrogen component. The crystallization kinetics of a-Si:H depends on the hydrogen amount bonded to the Si in the structure. For fulfilling the crystallization process, hydrogen atoms must break the bond and diffuse out. Therefore, the higher the concentration of hydrogen is, the lower control on crystallization kinetics. It suggests that the PVD produced non-hydrogenated a-Si film to be preferable for poly-Si-based films and devices.

One of the major important components for the electrical performance of semiconductor devices is the dopant concentration levels and their depth and spatial distributions. In this study, activated doping of a-Si films and their effect on the devices were analyzed with Lifetime and photoluminescence measurements. The corresponding boron and phosphorous doping concentration were explored by Electrochemical capacitance-voltage (ECV) technique due to its accuracy and dependency on the activated dopants. Implied V_{oc} and lifetime values calculated by using Sinton WCT-120 device for each step. Finally, solar simulator measurements show the efficiency of the fabricated cells.

5.2 Experimental Details

In an e-beam evaporation system, an electron beam heats the target material (Si). In addition to the e-beam evaporator, the system has effusion cells, one of which provides boron (B) doping (EC e-Beam system). A feature of this system is that effusion cells enable the direct addition of dopant vapor to the main flux of silicon beam. Changes in effusion cell temperature ramp (2000 to 2030 °C) with a ramped Si deposition rate (0 to 0.5 Å/s) cause in the changes in the doping concentrations and profiles. On the other hand, there are two choices of PECVD recipes as seen in Table 5.1.

Table 5.1. PECVD process parameters.

	p-type Recipe		
Temperature (°C)	**190-170**		
Pressure (Torr)	**1**		
Power (W)	**30**		
Deposition Duration (min)	**5**		
Gas Flow Rate(sccm)	SiH_4	B_2H_6	H_2
	13	**34**	**190**
Ratio B_2H_6/SiH_4	**0.052**		
	n-type Recipe		
Temperature (°C)	**210-130**		
Pressure (Torr)	**1**		
Power (W)	**30**		
Deposition Duration (min)	**5**		
Gas Flow Rate(sccm)	SiH_4	PH_3	H_2
	13	**25**	**125**
Ratio PH_3/SiH_4	**0.038**		

In this study, solid-phase crystallization (SPC) technique was applied, which is commonly used in many similar kinds of research of PV fabrication due to its ease of use, being contamination-free, and applicability for films with any thickness. SPC process depends on annealing time and duration. As known, crystallization of Si takes place at around 600 °C. SPC process could be prolonged annealing up to several hours to obtain the crystal formation at this critical temperature. First, for selecting the appropriate layer of polysilicon, a set of samples manufactured on thick silicon oxide layers. The fabricated 80 nm thick films on oxide-coated Si cell substrates are then further annealed at 600 °C for durations reached to 24 h to reach fully crystallized samples. We found that different doping concentrations resulted in different electrical properties. ECV results give information about the active value of the doping level.

After selecting the desired doping level, correlated to the dopant amount, the number of spins (unpaired electrons) were analyzed by EPR. Then, we prepared samples with the same amount of doping and with different annealing temperatures and characterized their physical properties as sheet resistance to obtain an applicable emitter layer of poly-Si for the use of TOPCon cells.

As the amount of concentration and region of crystallization temperature fixed, it is time to apply the poly-Si layer on a structure of a cell structure. For this purpose, 4 inches, 200 µm, double side textured, two ohm.cm, n & p-type Cz- Si wafers were employed as the substrate. After RCA-1 and RCA-2 cleaning steps, single side phosphorous doping was obtained by $POCl_3$ diffusion at 940 ^oC, protecting the other side by a PECVD coated SiN_x layer. Following the post diffusion cleaning steps, both hot temperature nitric acid oxidation (NAOS) and dry oxidation at 800 ^oC were applied, resulting in 1-1.2 nm thick wet chemical oxide and 3-4 nm thick dry oxide layers, respectively. The reference samples were kept with RCA oxide till a-Si layer deposition and exposed to short HF dip prior to deposition. The deposition of the films was carried out at a high vacuum level of 10^{-7} Torr. For this part of the study again, 50 nm, highly doped, p-type a-Si layers were deposited. The passive dopant concentration of layers was already measured by using a calibrated ECV system. Crystallization of the deposited amorphous films requires additional thermal treatment to obtain solid phase crystallization (SPC). For this study, annealing was done for one hour in tubular furnaces under N_2 at various temperatures of 800, 850, 900, and 950 °C.

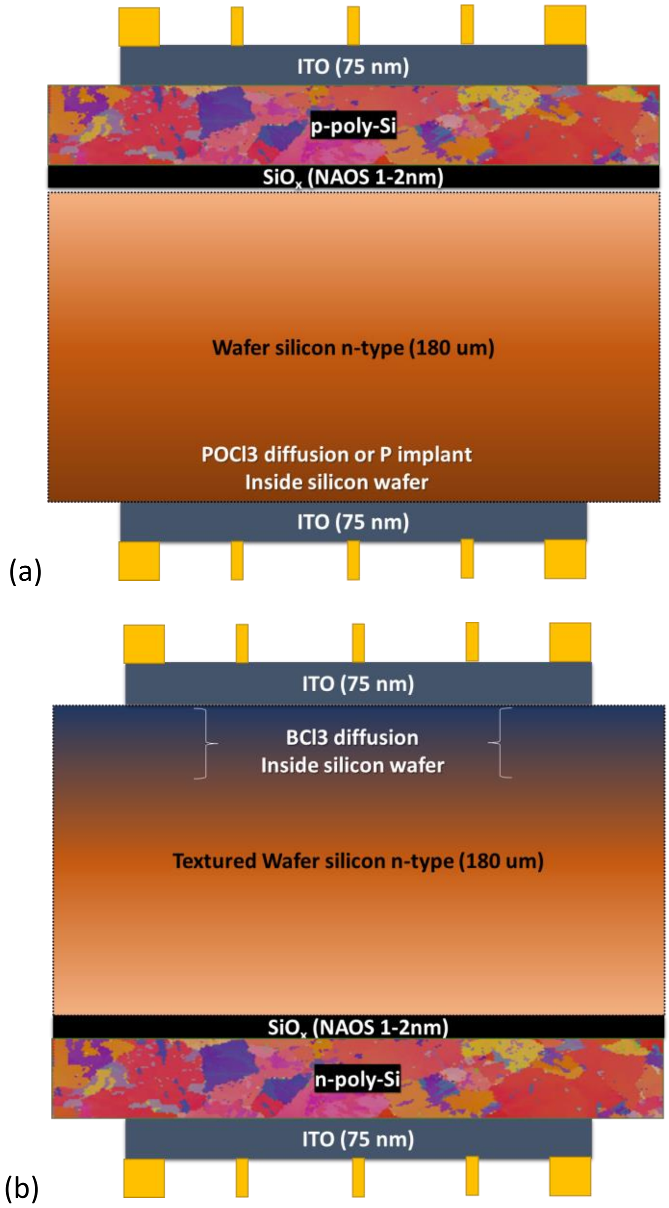

Figure 5.1 Structure of the cells with p-poly-Si as emitter on n-type Si (a) and n-poly-Si as BSF at back of n-type Si (b)

Annealing at high temperature converted p-type a-Si layers into p-poly-Si layers, which could then be applied for passivating contact cell structure. The performance of the obtained p-poly-Si layers by e-Beam EC was examined as emitter (at the front side of n-Si Figure 5.1(a)) and n-poly-Si by PECVD as BSF (at rear side n-Si) Figure 5.1 (b)).

For making the contacts standard 75 nm thick ITO deposited by sputtering and low temperature HJT past (Heraeus Sol590) was used. H-Grid Screen with 5BB/pitch, 1.65 mm and fw: 40 µm employed for both side of the bifacial cells. Furthermore, Drying 180°C 10 min in BTU Conveyor Belt Furnace. Then, post annealing applied at 200°C 15 min in NUVE Convection Furnace for separately front and rear side metallization steps.

5.3 Results & Discussion

The fabricated films were analyzed by several techniques in several steps with different approaches. Therefore, I am going to discuss each under some subtitles. As the process optimization was not assigned as my work, I just get some standard samples from the existing ones which generally optimized for HJT cases. The only importing approach for me is the doping profile. The results represented in Figure 5.2.

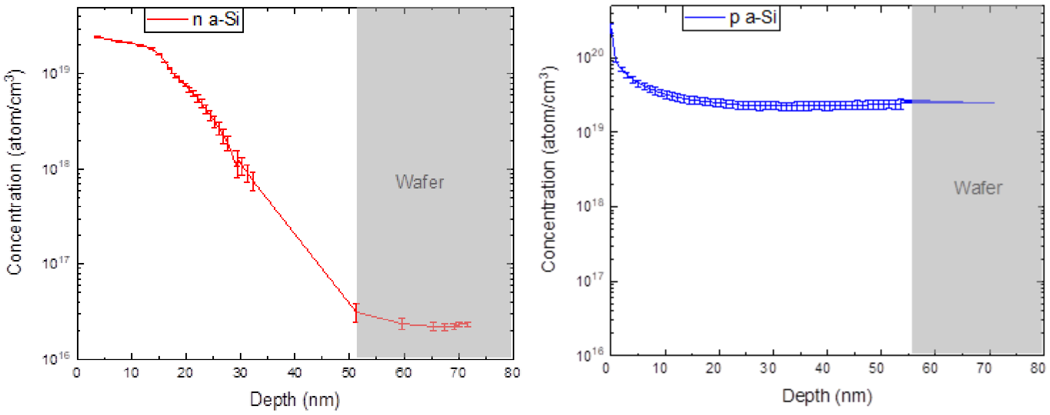

Figure 5.2. Doping Profile of a) n a-Si:H and b) p a-Si:H by ECV

i) Hydrogen and blistering effect on CVD fabricated films

In comparison of e-Beam EC and PECVD fabricated films mentioning the importance of the hydrogen atom roles in non-hydrogenated and hydrogenated a-Si through the experimental results is essential. From Sedani et al. 2020:

- To introducing hydrogen origin of hydrogenated a-Si (a-Si:H);

“Meanwhile, CVD techniques, generally, use pyrophoric gas of SiH4 and H2 for silicon thin film fabrication which could produce hydrogenated a-Si (a-Si:H) layer.”

- To introducing the possible effect of hydrogen in silicon lattice and to clarifying argument about boron activation and B-Si coordination;

“Moreover, in the case of hydrogenated a-Si, hydrogen atoms are located at the bond-centered (BC) site between B and neighboring host Si atoms, which could result as boron-hydrogen simple complex, namely H-B passivation center. This argument is also negligible for the case of non-hydrogenated a-Si that could reveal a relatively more active boron doping in silicon host lattice.”

- To arguing the effect of hydrogen presence in comparison between CVD-grown a-Si:H and e-beam EC-grown non-hydrogenated a-Si,

“When compared to this work, CVD-grown hydrogenated a-Si films are crystallized after longer incubation times, i.e. crystalline Raman peak appears only after the hydrogen atoms are removed from the lattice. Note that, such a crucial hydrogen dissociation process does not significantly affect the crystallization of e-beam evaporated non-hydrogenated a-Si.”

i) PECVD TOPCon Symmetric Samples for Lifetime Measurements

“In the case of e-Beam EC fabricated a-Si, it was presented before as the corresponding crystal growth rate which clearly increases upon boron concentration. On the other hand, for CVD-grown hydrogenated a-Si thin films, crystallization requires longer incubation times when the amount of hydrogen increases. Since the a-Si thin films investigated in this work are non-hydrogenated, crystal growth is not hindered due to hydrogen dissociation process. This makes applications with crystallization process remarkably advantageous when a-Si thin films are grown with e-beam EC as compared to other common techniques such as CVD.” The symmetric samples fabricated as scheme presented in Figure 5.3.

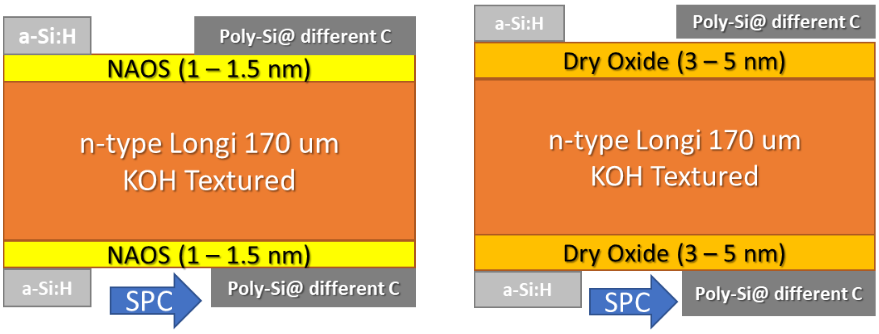

Figure 5.3. Symmetric samples for lifetime measurements.

We know that record-holding TOPCon cells fabricated by PECVD systems with at least 400 °C substrate temperature, world widely. In our system, we could not reach even 200 °C generally. I propose a dehydrogenation step. Due to the literature, 40h of post-annealing at 400 °C is the point that H concentration reaches the lowest amount. On the other hand, after 12h annealing results shows significant decrease in the H amount. Therefore, two sets of samples compared as one dehydrogenized for 40h while the other on face no dehydrogenation. Then crystallization process applied for 1 hour on both samples. SEM images in Figure 5.4 shows the blistering effect on the sample which not dehydrogenized.

	Dehydrogenated-40h @400C	Not Dehydrogenated
800C/1h	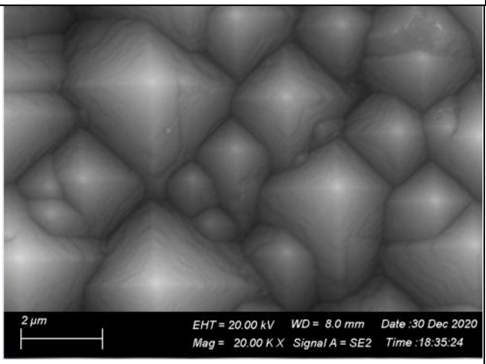	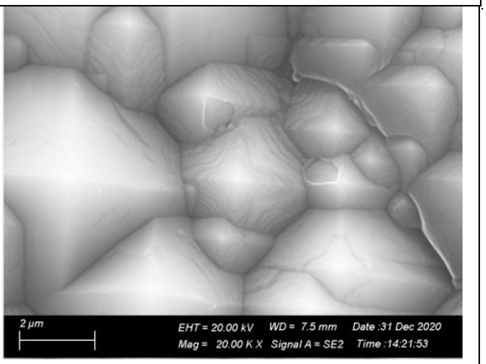
825C/1h	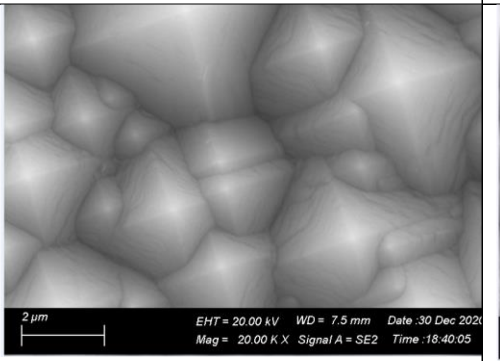	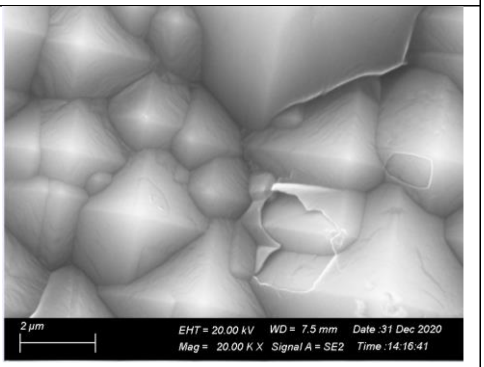
850C/1h	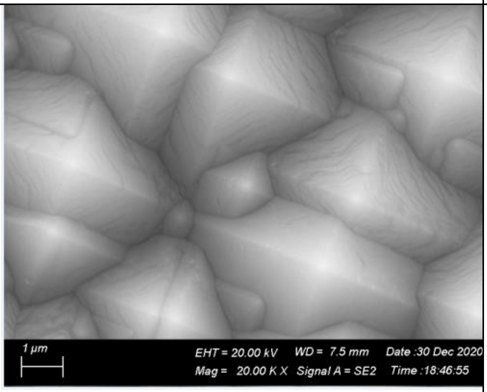	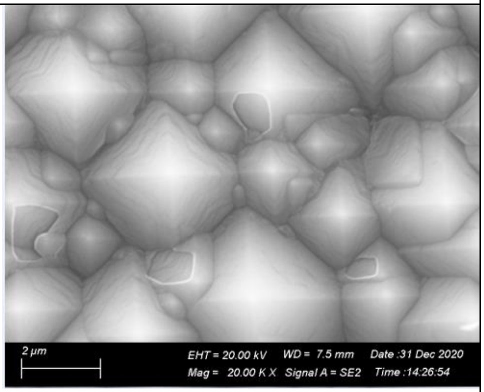
875C/1h	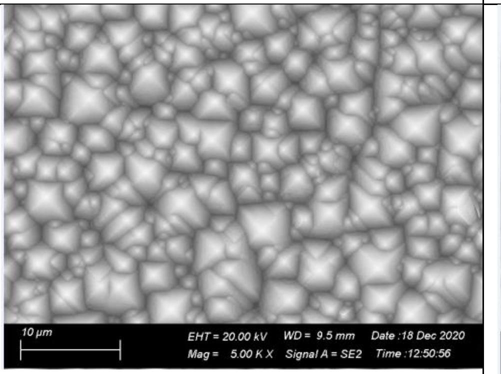 ***Large scale shown as blistering was rare**	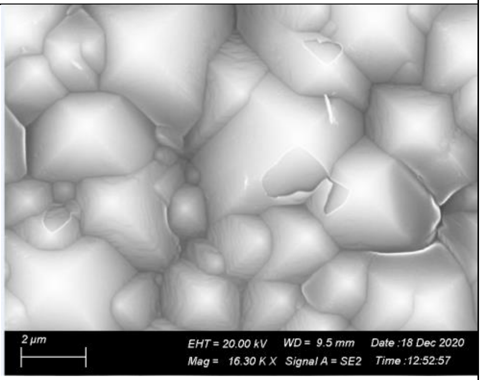

Figure 5.4. SEM mages for investigating blistering.

In the case of no dehydrogenation, there is blistering in all crystallization while in the case of dehydrogenated samples in temperatures higher than 875 could find some blistering.

As the dry oxide is thick as 5 nm and much dense in comparison with NAOS with 1-1.5 nm thickness, the dehydrogenation could act differently in meanwhile. Hydrogen atoms in dry oxide could get out of sample while in NAOS case H could penetrate in buck silicon as well. Making an analogy by PL mapping image could help us with the case.

For the last part I present iV_{oc} and lifetime results for symmetric coated samples which could reach 680 mV. There is no forming gas annealing (FGA) as the SiN_x could not perform for now (FGA should fulfilled just before SiN_x coating).

Dehydrogenation positive effect could seen all over, but detailed analysis should perform to explain the results propositions. At the end, without forming gas annealing or SiN_x coating (+firing) the results are desirable (Figure 5.5). The iV_{oc} higher than 680mV and lifetime more than 0.5 ms could reach higher values just by standard passivation steps.

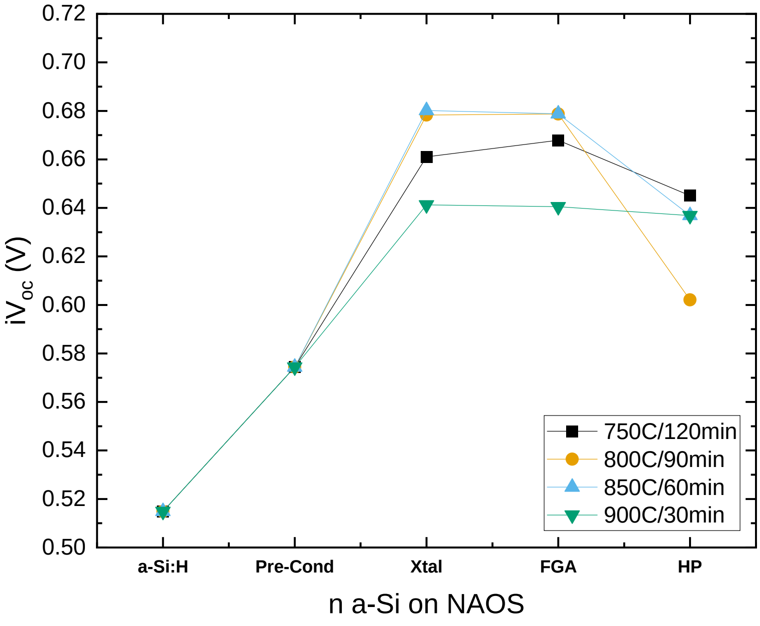

Figure 5.5. Evolution of iV_{oc} values for n a-Si on NAOS.

First of all, 425 °C and 1h Forming gas annealing (FGA) and the Hydrogen plasma applied at 200 °C for 7min for the sample of n-poly-Si on NAOS to heal the defects. Evolution of the symmetric samples could be followed by iV_{oc} values which is in a proper tendency with PL imaging results.

Also, 425 °C and 1h Forming gas annealing (FGA) and the Hydrogen plasma applied at 200 °C for 7min for the sample of n-poly-Si on Dry-Ox to heal the defects. Evolution of the symmetric samples could be followed by iV_{oc} values (Figure 5.6) which is in a proper tendency with PL imaging results.

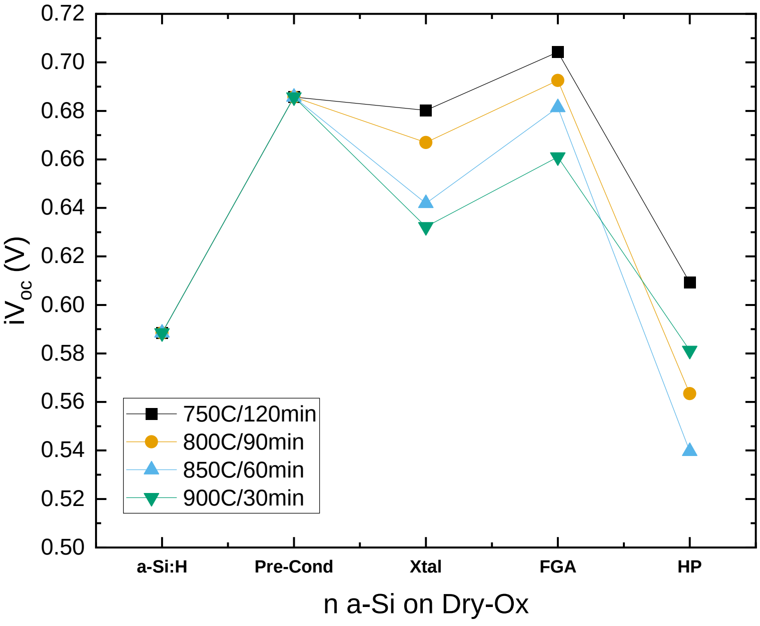

Figure 5.6. Evolution of iV$_{oc}$ values for n a-Si on Dry-Ox.

To understand the phosphorous behavior XPS analysis was utilized. The spectroscopy data gathered from a slight depth from the surface of poly-Si which produced by an Ar sputtering for a short while.

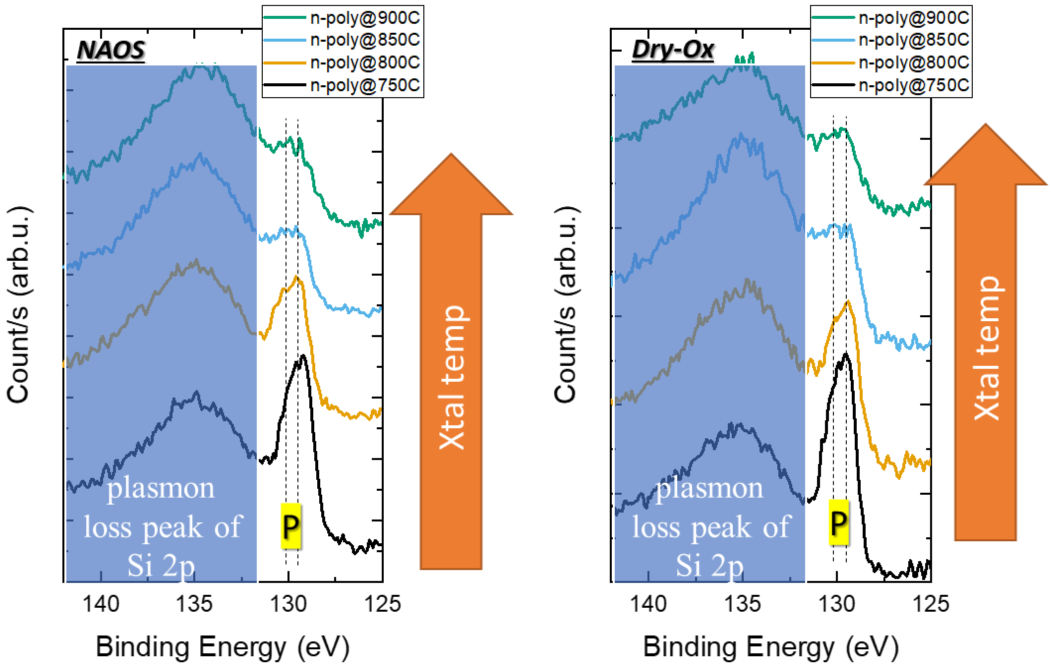

Figure 5.7. Phosphorous evolution through change in the annealing temperatures investigated by XPS analysis.

The XPS results (Figure 5.7) show a decrease in the phosphorous amount. In contrast, ECV measurements show that a primary annealing temperature help for phosphorous activation while higher temperatures lead a diffusion of phosphorous dopant in the bulk silicon. Moreover, extreme diffusion of dopants which occurred in highest temperatures cause lack of phosphorous in the poly-Si layer that reduce the performance of the half-fabricated cell (134.0 eV, 129.9 eV, and 129.0 eV, plasmon loss peak of the Si 2p photoelectron, P 2p1=2, and P 2p3=2 peaks, respectively).

Detail investigation by ECV shows that increase in the annealing temperatures cause for phosphorous activation in the upper layer while higher temperatures cause an over diffusion of the phosphorous to the substrate and an extra gathering in the surface and interface (Figure 5.8).

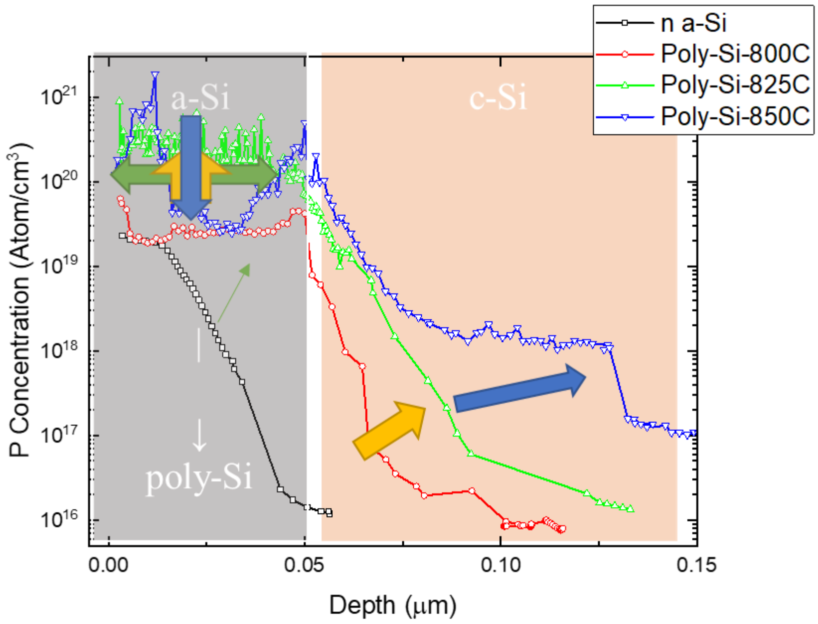

.

Figure 5.8. Trace of active phosphorous dopants in the TOPCon structures with different annealing temperatures.

On the other hand, 425 °C and 1h Forming gas annealing (FGA) and the Hydrogen plasma applied at 200 °C for 7min for the sample of p-poly-Si on NAOS to heal the defects. Evolution of the symmetric samples could be followed by iV$_{oc}$ values (Figure 5.9) which is in a proper tendency with PL imaging results.

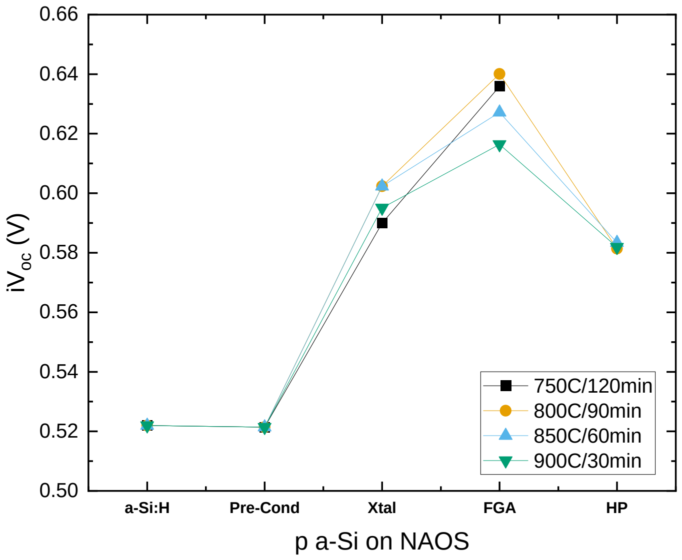

Figure 5.9. Evolution of iV_{oc} values for p a-Si on NAOS.

Finally, 425 °C and 1h Forming gas annealing (FGA) and the Hydrogen plasma applied at 200 °C for 7min for the sample of p-poly-Si on Dry-Ox to heal the defects. Evolution of the symmetric samples could be followed by iV_{oc} values (Figure 5.10) which is in a proper tendency with PL imaging results.

In the case of p-poly-Si XPS results (Figure 5.11) for e-Beam evaporated p-poly-Si presented in the chapter 3. For the p-poly-Si deposited by PECVD we can see that variation of crystallization temperatures did not change the state of boron in the poly-Si structure.

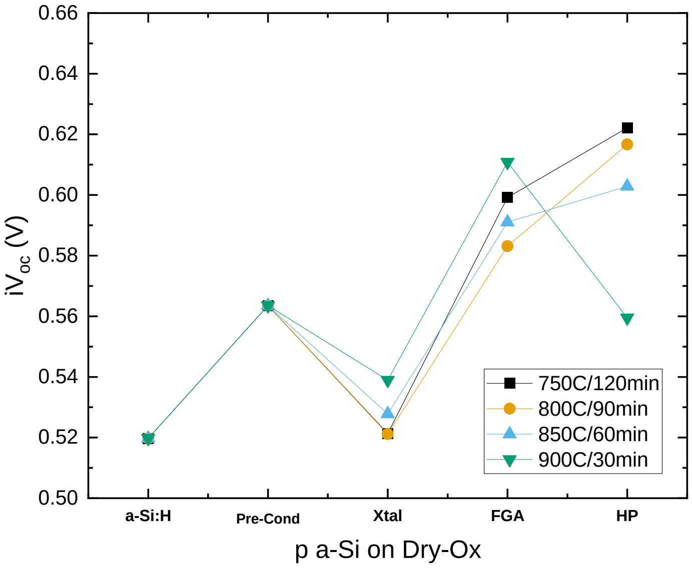

Figure 5.10. Evolution of iV$_{oc}$ values for p a-Si on Dry-Ox.

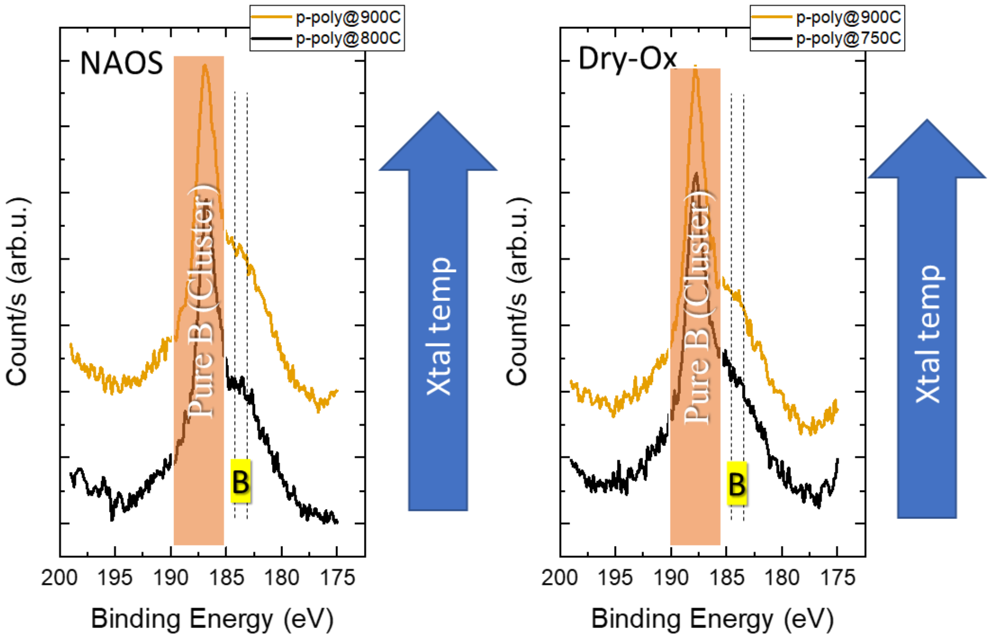

Figure 5.11. Boron evolution through change in the annealing temperatures investigated by XPS analysis.

Three dimensional ToF-SIMS tomography (Figure 5.12) propose that, boron is not active in the PECVD deposited p-poly-Si due to the hydrogen bonded boron compounds as BH and BH_2. Even more, B_2 compounds detected ions represent boron clusters inside the deposited layer which act as a passive boron and defect states.

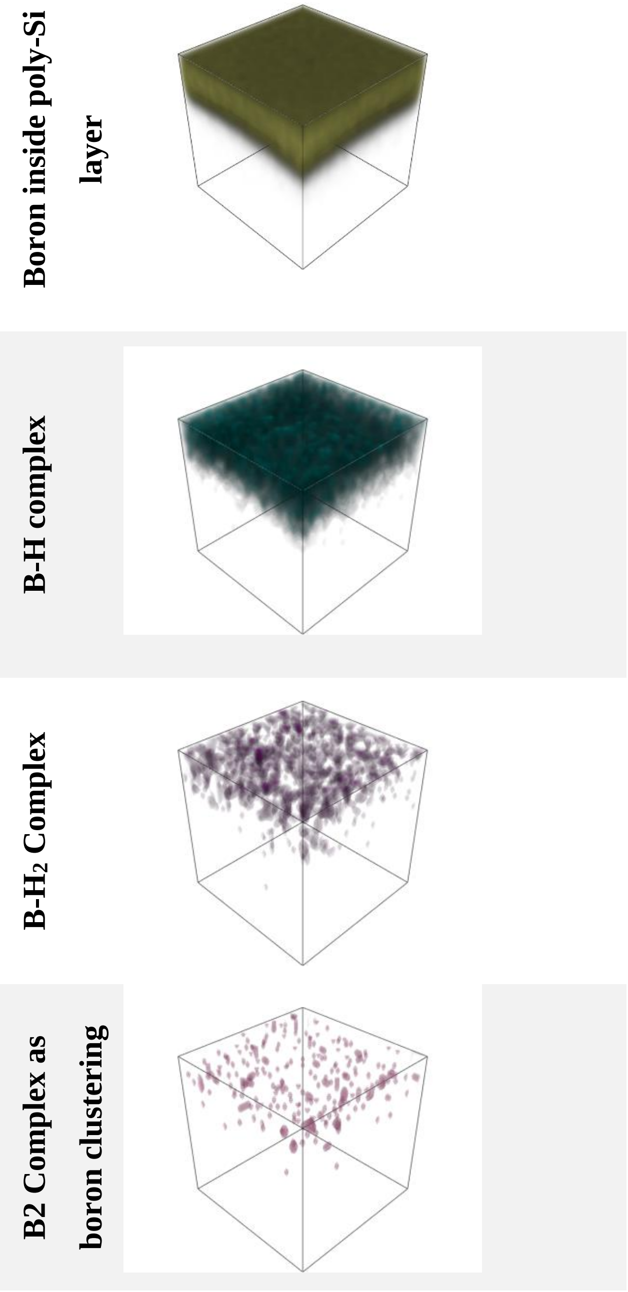

Figure 5.12. Three dimensional ToF-SIMS tomography for boron containing compounds.

As discussed before, e-beam EC evaporated p-type layer is non-hydrogenated and could be replaced for p-poly TOPCon due to lack of hydrogen bonded boron compounds.

i) Fabrication for the e-Beam EC set of TOPCon

First attempt in previous chapter resulted with 680 mV value of iV_{oc}, which had not measured as cell. Second attempt fulfilled for cell fabrication, which reached record efficiency of 16.2% with 550mv iV_{oc}. The low iV_{oc} assumed to cause by contamination affected all the laboratory infrastructure (as ToF-SIMS analysis proposed).

Now, the third set fulfilled with dry oxide and NAOS samples with fabricating reference samples. The homogeneity of the poly-Si checked by Spectroscopic Ellipsometry showing as 7 angstrom max variation from middle of a 4-inch wafer to the edge-side.

Boron activation evaluated primarily by fabricating poly-Si on thick oxide. ECV measurements for different crystallization temperatures with fixed 60 min duration.

The results show a slight deference in the amount of activated boron in the films. For deeper understanding, higher durations applied to lower crystallization temperatures to see the active dopant amount for comparable thermal loads.

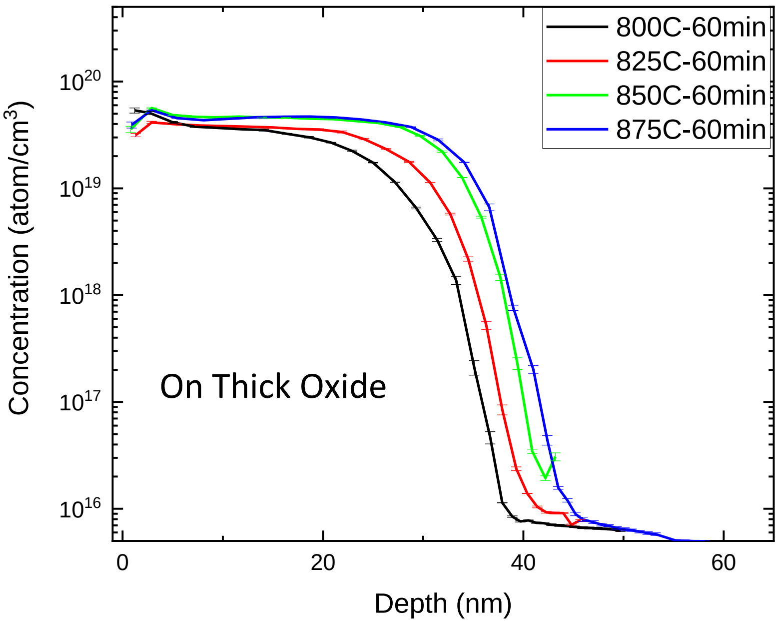

Figure 5.13. On n-type Topsil polished wafer (4 inch) with thick silicon oxide.

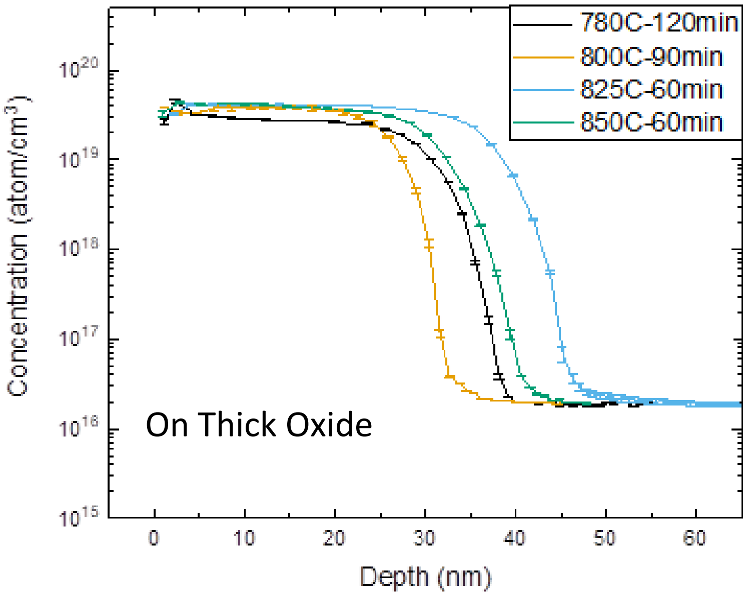

Figure 5.14. On p-type Topsil polished wafer (4 inch) with thick silicon oxide.

ECV results presented inFigure 5.13 and Figure 5.14, show that compensation of the thermal load by changing duration for different crystallization temperatures tune the active amount of boron in the poly layer with similar values. Solid phase crystallization occurred at temperatures more than 600C like 700C seems to be insufficient. However, temperatures more than 750 ~780C with duration more than 2h could described as minimum essential annealing condition.

Nevertheless, doping profile is must tuned due to calibrating V_{oc} and J_{sc} to reach the best possible efficiency according to the fill factor of the cell. Higher V_{oc} could reach by higher active doping while passive doping reduces the J_{sc} by rising the defects causing recombination centers. Although, higher doping of an emitter could be use foul with a junction depth limitation. Thermal load (temperature & duration) could be used as the basic tuning factor to adjust the depth profile with an accurate annealing process as our trials on fabricating p-poly-Si layer on a silicon oxide coated silicon wafer for a TOPCon/POLO cell. In this Example of annealing effect on doping, ECV profile (Figure 5.15) shows boron tail tuned inside wafer by adjusting e-beam evaporated p-poly crystallization temperature.

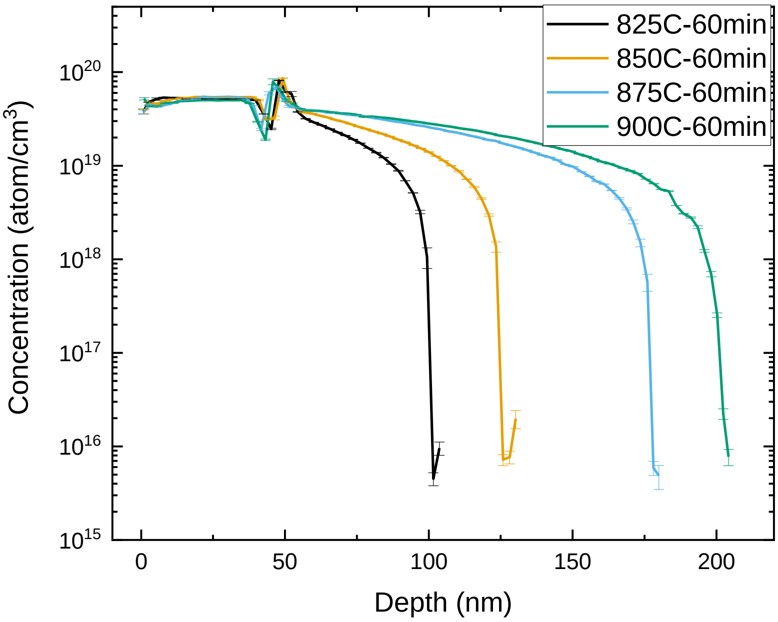

(a)

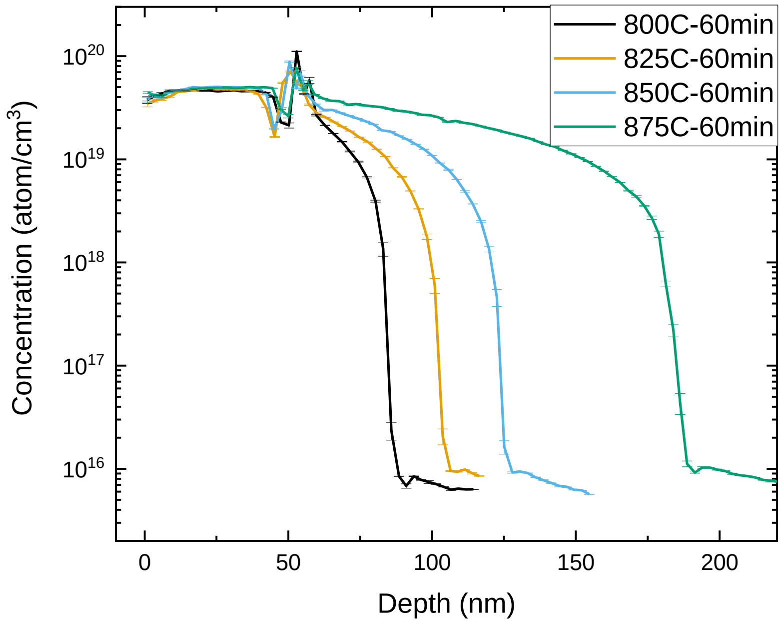

(b)

Figure 5.15. ECV profile of boron for NAOS on a)n-type wafer and b) p-type wafer.

The boron accumulation on NAOS interface could be approved by ECV results of the interface between poly-Si and bulk silicon. However, we could trace hydrogen gathering in the interface and poly-Si grain boundries, as well (Figure 5.16).

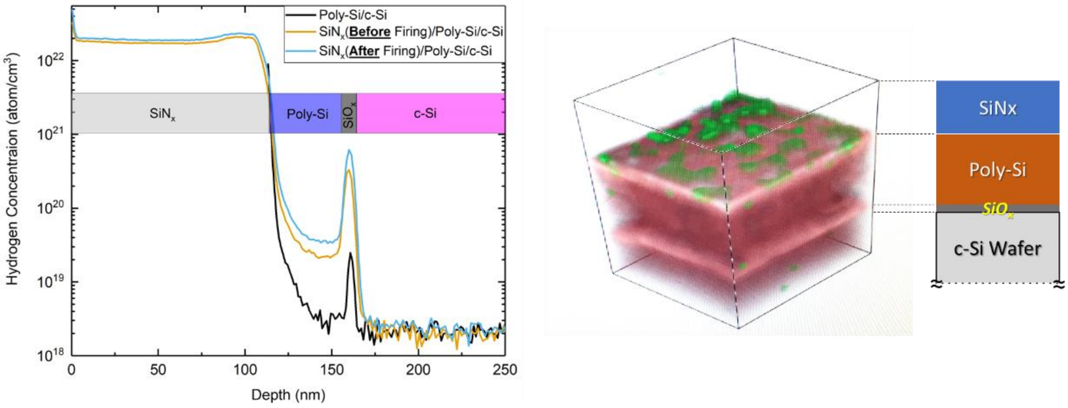

Figure 5.16. Trace of hydrogen in a TOPCon structure.

Finally, the optimization of half-fabricated cells lead us to the production of the final cells. Thickness of 50 and 30 nm was proposed for both p-poly-Si emmiter and n-poly-Si BSF on n type textured wafers (170 µm, 1-3 Ω.cm). Furthermore, four different crystallization temperature were investigated for each step of the process.

At the end p-poly emitter by e-Beam EC and n-poly by PECVD investigated with different thicknesses and different annealing temperatures to reach the champion cells as the consequence of this work. All the figures below show the comparison to let us for conclusion.

p-poly 50 nm emitter:

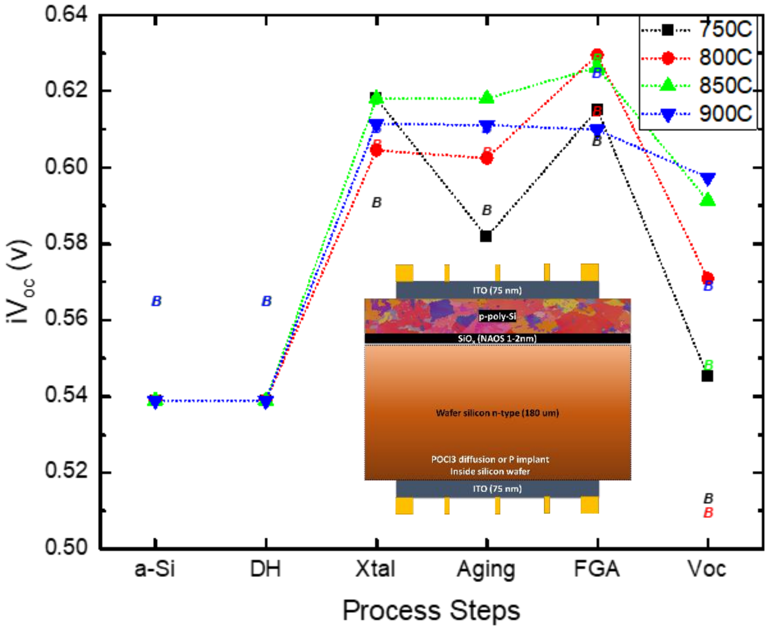

Figure 5.17. The iV$_{oc}$ evolution result:

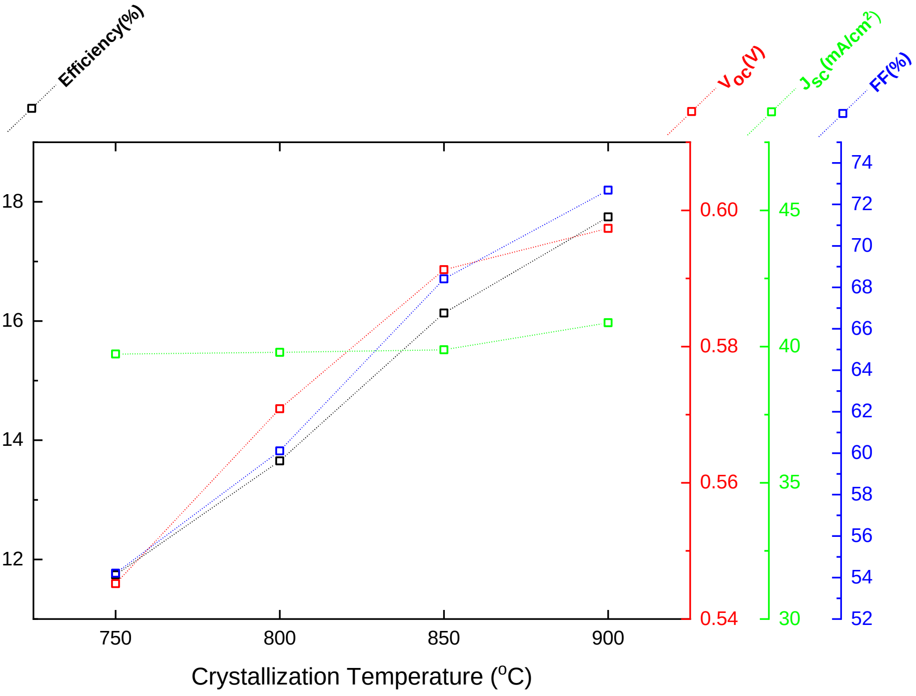

Figure 5.18.: Bifacial cells' efficiency results of front side:

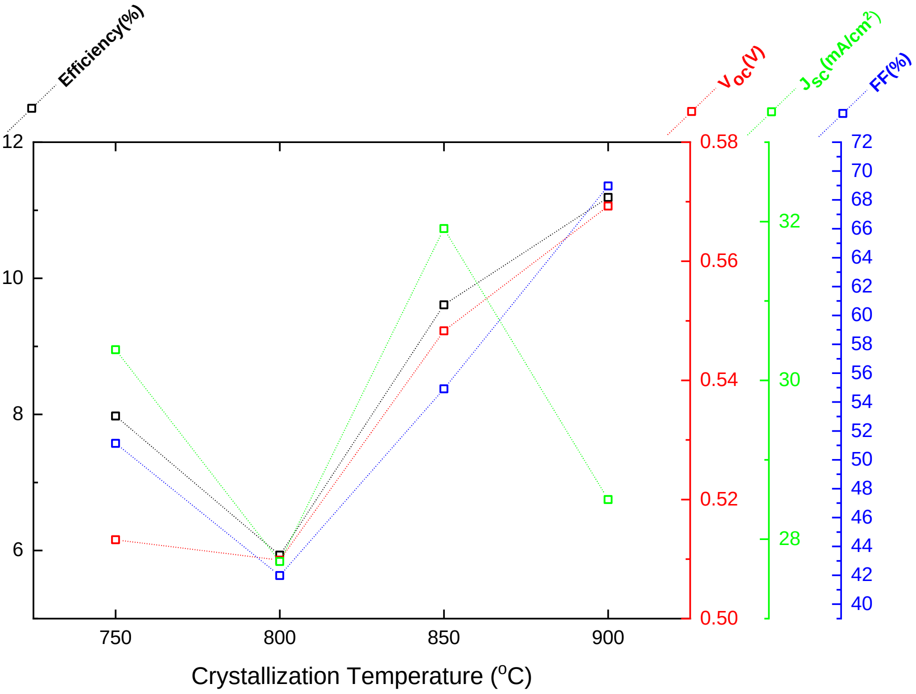

Figure 5.19. Bifacial cells' efficiency results of rear side

p-poly-30nm emitter:

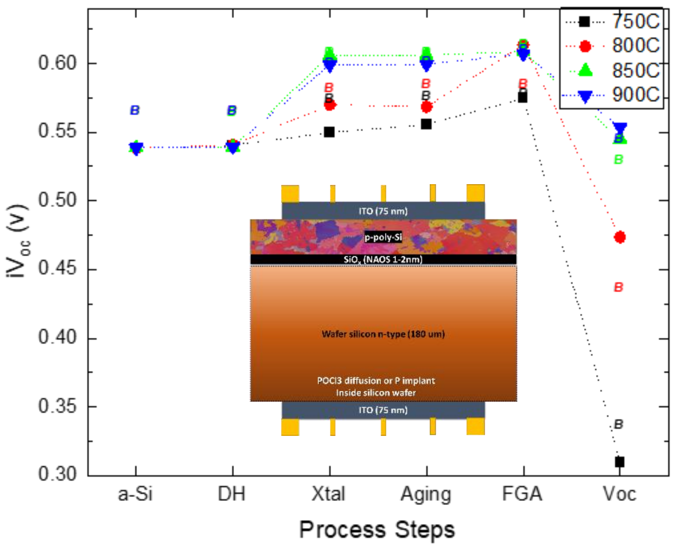

Figure 5.20. The iV$_{oc}$ evolution result:

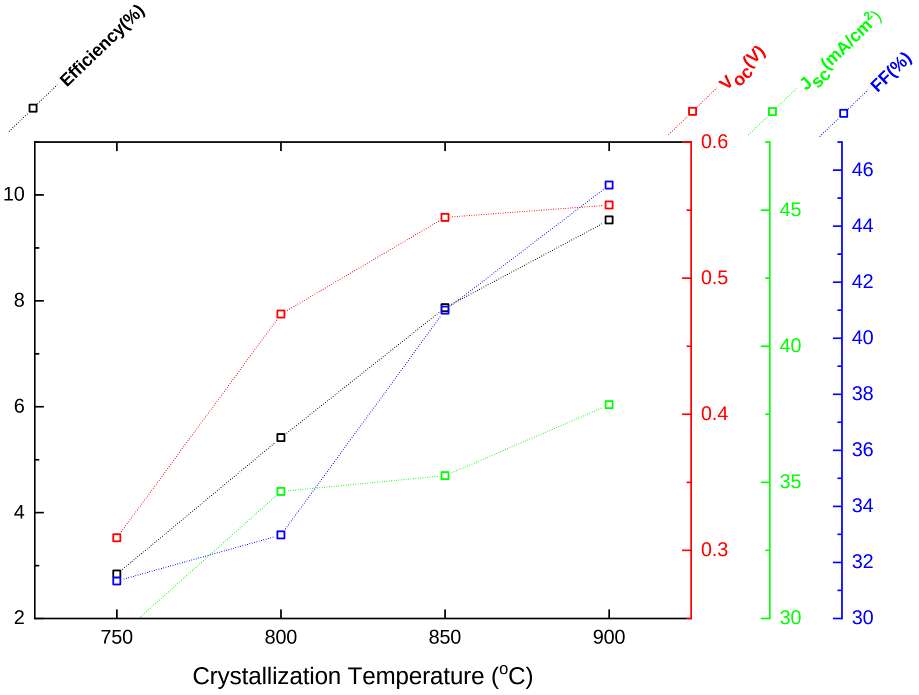

Figure 5.21. Bifacial cells’ efficiency results of front side:

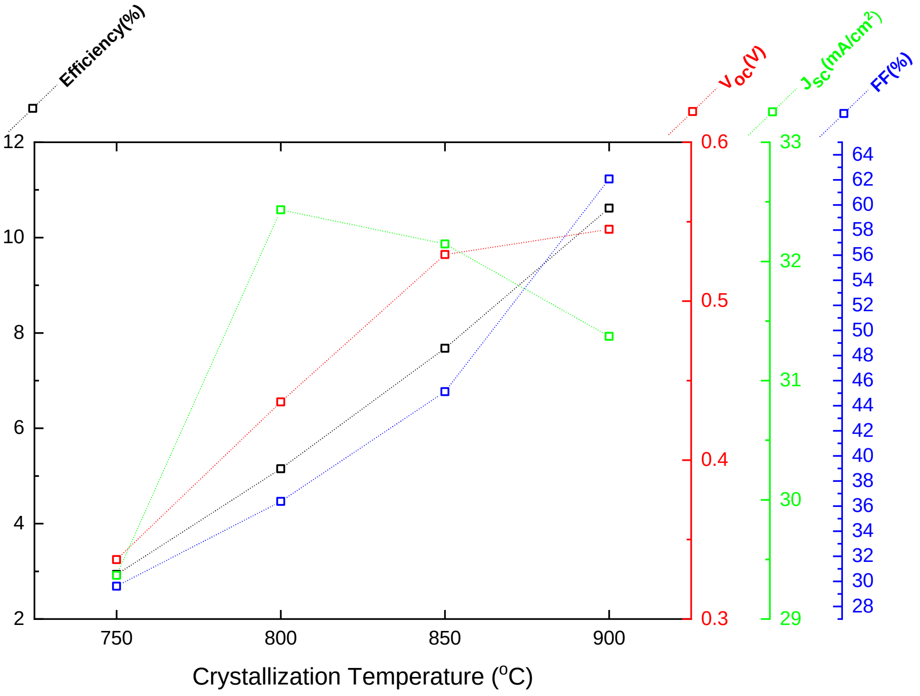

Figure 5.22. Bifacial cells' efficiency results of rear side:

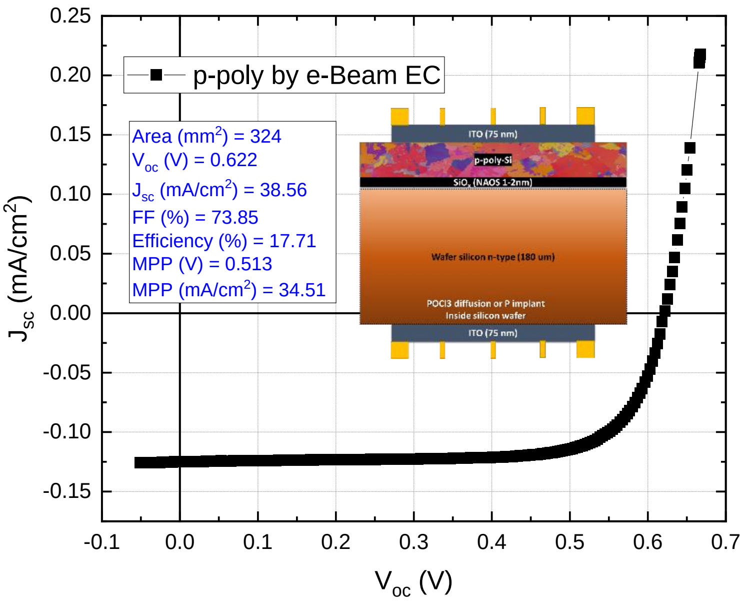

Figure 5.23 The champion cell I-V curve for p-poly-Si emitter by e-Beam EC:

n-poly 50 nm BSF:

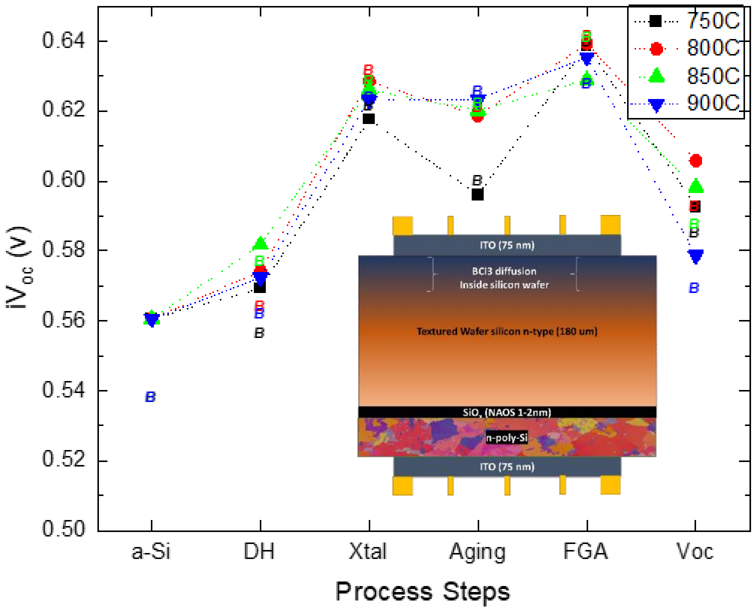

Figure 5.24 The iV_{oc} evolution result:

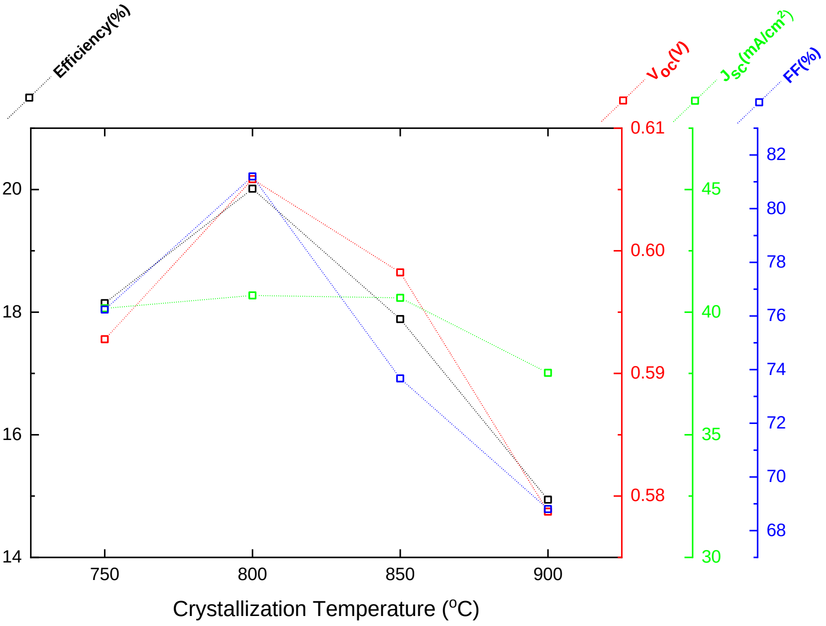

Figure 5.25. Bifacial cells' efficiency results of front side:

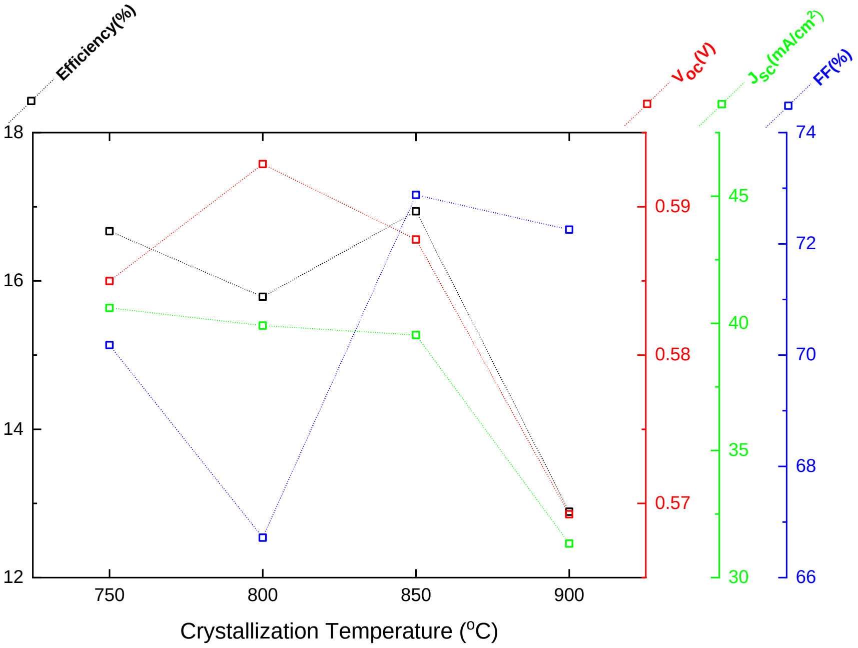

Figure 5.26. Bifacial cells’ efficiency results of rear side:

n-poly 30 nm BSF:

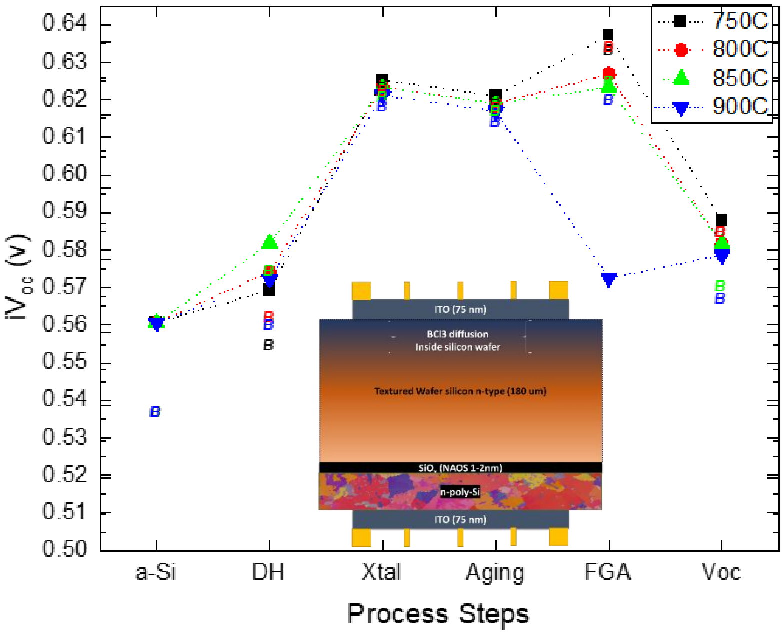

Figure 5.27. The iV_{oc} evolution result:

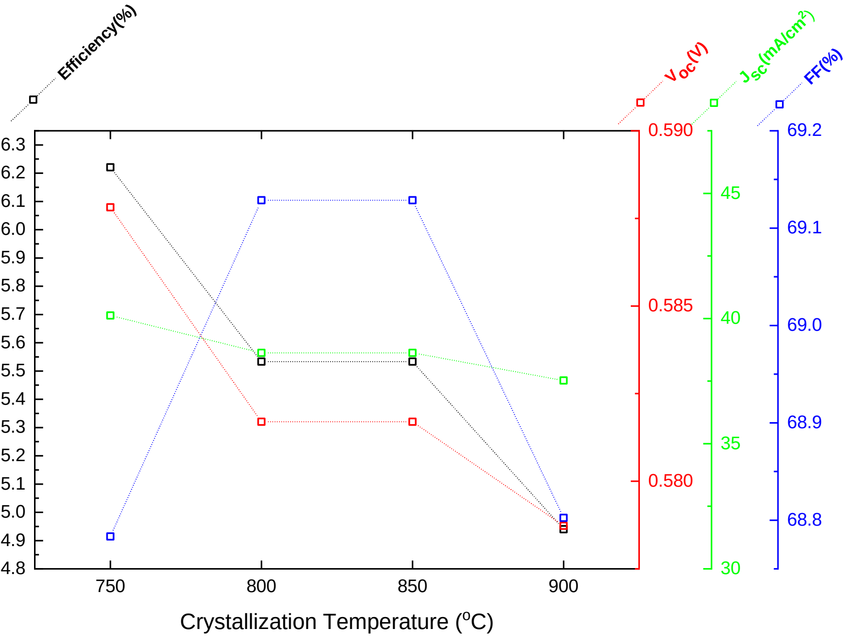

Figure 5.28. Bifacial cells' efficiency results of front side:

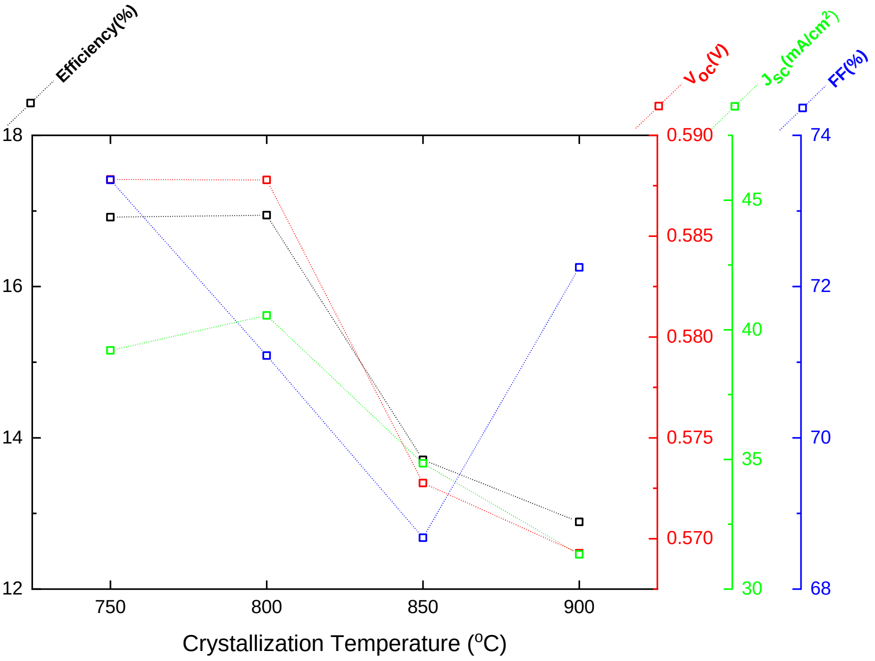

Figure 5.29. Bifacial cells' efficiency results of rear side:

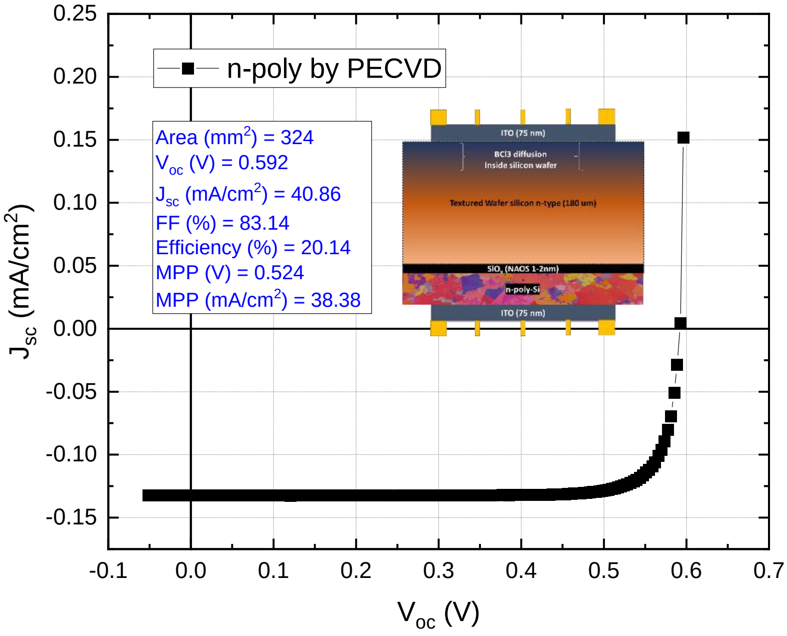

Figure 5.30. The champion cell I-V curve for n-poly-Si BSF by PECVD:

Consequently, we could propose a structure for bifacial double sided TOPCon for future works.

5.4 Conclusion

By lowering the minority carrier recombination velocities at c-Si/metal contact surfaces, carrier selective passivating contacts have made it possible to achieve greater conversion efficiencies. The gamechanger companies of the solar industry are looking at the amazing passivation capabilities of doped polysilicon (poly-Si) layers that are deposited over silicon oxide (SiO_x). Experts in the photovoltaic sector are forecasting that poly-Si/SiO_x structures, also known as TOPCon, will have a prosperous future as the future of the PV industry. Even though CVD technologies such as PECVD and LPCVD are available, it is still feasible to go with a green approach of non-hazardous deposition of a poly-Si layer by using e-beam evaporation equipped with effusion cells. This is one of the ways that this may be accomplished. The production process does not need the use of potentially harmful process gases like PH3 and B2H6 thanks to the e-beam technology. In addition, owing non-hydrogenated boron doping source would be advantageous for the known related defects.

E-beam deposition of p-type a-Si layers was employed to examine passivating contact applications, and low temperature PECVD was used to deposit n-type a-Si layers on the other side of the device. In this study, we evaluate the effect that the temperatures at which boron and phosphorous dopant crystals form have on the activation of doping. This non-hydrogenated layer of p-a-Si is perfect for the low-temperature activation of boron doping since there are no boron-hydrogen complexes present to interfere with the process. In the end, p-poly and n-poly layers that are blister-free form simultaneously on both sides of the cell. The faults in the non-hydrogenated passivating contacts may be healed using further hydrogenation procedures in conjunction with ITO deposition. As a consequence of our research, we are able to build bifacial double-sided TOPCon cells, which achieve an efficiency of 17.7% on the p-poly side and 20.2% on the n-poly side.

REFERENCES

[1] A.E. Becquerel, Recherches sur les effects de la radiation chimique de ia lumiere solaire au moyen des courants electriques, C. R. Acad. Sci. 9 (1839) 145–149.

[2] D.M. Chapin, C.S. Fuller, G.L. Pearson, A new silicon p-n junction photocell for converting solar radiation into electric power, J. Appl. Phys. 25 (1954) 676–677, https://doi.org/10.1063/1.1721711.

[3] S.W. Glunz, R. Preu, D. Biro, Crystalline silicon solar cells-state-of-the-art and future developments, Compr. Renew. Energy Book Chapter (2012), https://doi.org/10.1016/B978-0-08-087872-0.00117-7.

[4] A. Blakers, Development of the PERC solar cell, IEEE J. Photovolt. 9 (3) (2019) 629–635, https://doi.org/10.1109/JPHOTOV.2019.2899460.

[5] J Liu, Y. Yao, S. Xiao, X. Gu, Review of status developments of high-efficiency crystalline silicon solar cells, J. Phys. D Appl. Phys. 51 (2018), https://doi.org/10.1088/1361-6463/aaac6d article id: 123001.

[6] R. Peibst, U. Romer, ¨ Y. Larionova, M. Rien¨acker, A. Merkle, N. Folchert, S. Reiter, M. Turcu, B. Min, J. Krügener, D. Tetzlaff, E. Bugiel, T. Wietler, R. Brendel, Working principle of carrier selective poly-Si/c-Si junctions: is tunnelling the whole story? Solar Energy Mater. Solar Cells 158 (2016) 60–67, https://doi.org/10.1016/j.solmat.2016.05.045.

[7] Yablonovitch, E., Gmitter, T., Swanson, R. M., & Kwark, Y. H. (1985). A 720 mV open circuit voltage SiO x: c-Si: SiO x double heterostructure solar cell. *Applied Physics Letters*, *47*(11), 1211-1213.

[8] F. Feldmann, M. Bivour, C. Reichel, M. Hermle, S.W. Glunz, A passivated rear contact for high-efficiency n-type silicon solar cells enabling high VocS and FF>82%”, in: Proceedings of the 28th European PV Solar Energy Conference and Exhibition, Paris, France, 2013, https://doi.org/10.4229/28thEUPVSEC2013- 2CO.4.4, 30 September –4 October.

[9] F. Feldmann, M. Bivour, C. Reichel, H. Steinkemper, M. Hermle, S.W. Glunz, Tunnel oxide passivated contacts as an alternative to partial rear contacts, Solar Energy Mater. Solar Cells 131 (2014) 46–50, https://doi.org/10.1016/j.solmat.2014.06.015.

[10] D. Adachi, J.L. Hernandez, ´ K. Yamamoto, Impact of carrier recombination on fill factor for large area heterojunction crystalline silicon solar cell with 25.1% efficiency, Appl. Phys. Lett. 107 (2015), https://doi.org/10.1063/1.4937224 article id: 233506.

[11] D.D. Smith, G. Reich, M. Baldrias, M. Reich, N. Boitnott, G. Bunea, Silicon solar cells with total area efficiency above 25%, in: Proceedings of the IEEE 43rd Photovoltaic Specialists Conference (PVSC), 2016, pp. 3351–3355, https://doi.org/10.1109/PVSC.2016.7750287.

[12] J. Nakamura, N. Asano, T. Hieda, C. Okamoto, H. Katayama, K. Nakamura, Development of heterojunction back contact Si solar cells, IEEE J. photovolt. 4 (6) (2014) 1491–1495, https://doi.org/10.1109/JPHOTOV.2014.2358377.

[13] K. Masuko, M. Shigematsu, T. Hashiguchi, D. Fujishima, M. Kai, N. Yoshimura, T. Yamanishi, Achievement of more than 25% conversion efficiency with crystalline silicon heterojunction solar cell, IEEE J. Photovolt. 4 (6) (2014) 1433–1435, https://doi.org/10.1109/JPHOTOV.2014.2352151.

[14] K. Yoshikawa, H. Kawasaki, W. Yoshida, Silicon heterojunction solar cell with interdigitated back contacts for a photoconversion efficiency over 26%, Nat Energy 2 (2017) 17032, https://doi.org/10.1038/nenergy.2017.32, aticle id.

[15] K. Yoshikawa, W. Yoshida, T. Irie, H. Kawasaki, K. Konishi, H. Ishibashi, T. Asatani, D. Adachi, M. Kanematsu, H. Uzu, K. Yamamoto, Exceeding conversion efficiency of 26% by heterojunction interdigitated back contact solar cell with thin film Si technology, Sol. Energy Mater. Sol. Cells 173 (2017) 37–42, https://doi.org/10.1016/j.solmat.2017.06.024.

[16] LONGi's Heterojunction Cell Efficiency Jumps To 26.30% Within A Week 29 (2021). https://taiyangnews.info/technology/26-30-efficiency-for-longis-hjt-solar-cell/.

[17] https://www.prnewswire.com/in/news-releases/longi-solar-sets-new-bifacial mono-perc-solar-cell-world-record-at-24-06-percent-875820879.html, "LONGi Solar sets new bifacial mono-PERC solar cell world record at 24.06 percent", 16 Jan, 2019.

[18] A. Richter, J. Benick, F. Feldmann, A. Fell, M. Hermle, S.W. Glunz, n-Type Si solar cells with passivating electron contact: identifying sources for efficiency limitations by wafer thickness and resistivity variation, Sol. Energy Mater. Sol. Cells 173 (2017) 96–105, https://doi.org/10.1016/j.solmat.2017.05.042.

[19] R. Goslich, 26.1 % record efficiency for p-type crystalline Si solar cells" by ISFH. https://idw-online.de/de/news688784.

[20] R. Peibst, M. Rienacker, ¨ Y. Larionova, N. Folchert, F. Haase, C. Hollemann, S. Wolter, J. Krügener, P. Bayerl, J. Bayer, M. Dzinnik, R.J. Haug, R. Brendel, Towards 28 %-efficient Si single-junction solar cells with better passivating POLO junctions and photonic crystals, Sol. Energy Mater. Sol. Cells 238 (2022), 111560, https://doi.org/10.1016/j.solmat.2021.111560.

[21] High efficiency n-type cell technology: Development and prospects 15 (2021). https://www.infolink-group.com/en/solar/analysis-trends/n-type-high-efficiency-cell-technology-development-and-prospect. September.

[22] International Technology Roadmap for Photovoltaic (ITRPV), Thirteenth Edition, March 2022, https://itrpv.vdma.org/web/itrpv/download.

[23] S.W. Glunz, F. Feldmann, A. Richter, M. Bivour, C. Reichel, H. Steinkemper, J. Benick, M. Hermle, The irresistible charm of a simple current flow pattern- 25% with a solar cell featuring a full-area back contact", in: Proceedings of the 31st European Photovoltaic Solar Energy Conference and Exhibition, Hamburg, 2015, https://doi.org/10.4229/EUPVSEC20152015-2BP.1.1. September2015.

[24] Jolywood unveils 700 W TOPCon PV module 8 October (2021). https://www.pv-magazine.com/2021/10/08/jolywood-unveils-700-mw-topcon-pv-module.

[25] Longi claims 25.19% efficiency for p-type TOPCon solar cell 21 (2021). https://www.pv-magazine.com/2021/07/21/longi-claims-25-19-efficiency-for p-type-topcon-solar-cell/. July.

[26] Longi unveils new 25.19% efficiency panel in p-type TOPCon cell panel 23 (2021). http://agentfactor.net/solar-news-july-23rd-2021/. July.

[27] Shaw, Vincent, The weekend read: Life after PERC .8 May (2021). https://www.pv-magazine.com/2021/05/08/the-weekend-read-life-after-perc/.

[28] Bellini, Emiliano. TOPCon vs PERC – a battle between fast learning curves. 15 February 2022. https://www.pv-magazine.com/2022/02/15/topcon-vs-perc-a-battle-between-fast-learning-curves/.

[29] Kafle, B.S. Goraya, S. Mack, F. Feldmann, S. Nold, J. Rentsch, TOPCon technology options for cost efficient industrial manufacturing, Sol. Energy Mater. Sol. Cells 227 (2021), 111100, https://doi.org/10.1016/j.solmat.2021.111100 article id.

[30] Tuan Le, A., Basnet, R., Yan, D., Chen, W., Nandakumar, N., Duttagupta, S., Seif, J.P., & Hameiri, Z. (2021). Temperature-dependent performance of silicon solar cells with polysilicon passivating contacts. Solar Energy Materials and Solar Cells, 225, 111020.

[31] W. Wu, J. Bao, L. Ma, C. Chen, R. Liu, Z. Qiao, J. Chen, Z. Liu, Development of industrıal n-type bifacıal topcon solar cells and modules, in: Proceedings of the 36th European PV Solar Energy Conference and Exhibition, Marseille, France 9–13, 2019, 10.4229/EUPVSEC20192019-2BP.1.5. September2019.

[32] JinkoSolar, N-type TOPCon: Combating LID and LeTID for all locations, 21 December, (2021), https://www.pv-magazine.com/press-releases/n-type-topcon-combating-lid-and-letid-for-all-locations.

[33] M. Hermle, F. Feldmann, J. Eisenlohr, J. Benick, A. Richter, B. Lee, P. Stradins, A. Rohatgi, S.W. Glunz, Approaching efficiencies above 25% with both sides-contacted silicon solar cells, in: Proceedings of the IEEE 42nd Photovoltaic Specialist Conference (PVSC), New Orleans, LA, 2015, pp. 1–3, https://doi.org/10.1109/PVSC.2015.7356219.

[34] F. Feldmann, M. Simon, M. Bivour, C. Reichel, M. Hermle, S.W. Glunz, Efficient carrier-selective p- and n-contacts for Si solar cells, Solar Energy Mater. Solar Cells 131 (2014) 100–104, https://doi.org/10.1016/j.solmat.2014.05.039.

[35] F. Feldmann, K-U Ritzau, M. Bivour, A. Moldovan, S. Modi, J. Temmler, M. Hermle, S.W. Glunz, High and low work function materials for passivated contacts, in: Proceedings of the 5th International Conference on Silicon Photovoltaics, SiliconPV 2015, Energy Procedia 77, 2015, pp. 263–270, https://doi.org/10.1016/j.egypro.2015.07.037.

[36] K. Tao, S. Jiang, R. Jia, Y. Zhou, P. Zhang, X. Dai, H. Sun, Z. Jin, X. Liu, The impact of indium tin oxide deposition and post annealing on the passivation property of TOPCon solar cells, Sol. Energy 176 (2018) 241–247, ηttps://doi.org/10.1016/j.solener.2018.10.034.

[37] T. Sontheimer, C. Becker, U. Bloeck, S. Gall, B. Rech, Crystallization kinetics in electron-beam evaporated amorphous silicon on ZnO:Al-coated glass for thin film solar cells, Appl. Phys. Lett. 95 (2009) 1–4. doi:10.1063/1.3222917.

[38] D. Song, D. Inns, A. Straub, M.L. Terry, P. Campbell, A.G. Aberle, Solid phase crystallized polycrystalline thin-films on glass from evaporated silicon for photovoltaic applications, Thin Solid Films. 513 (2006) 356–363. doi:10.1016/j.tsf.2006.01.010.

[39] K. Sera, F. Okumura, H. Uchida, S. Itoh, S. Kaneko, K. Hotta, High-Performance TFT's Fabricated by XeCl Excimer Laser Annealing of Hydrogenated Amorphous-Silicon Film, IEEE Trans. Electron Devices. 36 (1989) 2868–2872. doi:10.1109/16.40970.

[40] D.E. Polk, D.S. Boudreaux, Tetrahedrally coordinated random-network structure, Phys. Rev. Lett. 31 (1973) 92–95. doi:10.1103/PhysRevLett.31.92.

[41] S. Roorda, W.C. Sinke, J.M. Poate, D.C. Jacobson, S. Dierker, B.S. Dennis, D.J. Eaglesham, F. Spaepen, P. Fuoss, Structural relaxation and defect annihilation in pure amorphous silicon, Phys. Rev. B. 44 (1991) 3702–3725. doi:10.1103/PhysRevB.44.3702.

[42] A. Sherman, Chemical Vapor Deposition for Microelectronics: Principles, Technology, and Applications, Noyes Publications, Westwood, NJ, USA, 1987.

[43] H.O. Pierson, Handbook of chemical vapor deposition (CVD), principles, technology, and applications, 2nd ed., Noyes Publications, Park Ridge, NJ, USA, 1999.

[44] K. Seshan, Handbook of Thin Film Deposition, 3rd ed., Elsevier, Oxford, UK, 2012.

[45] S.H. Sedani, Fabrication and doping of thin crystalline Si films prepared e-beam evaporation on glass substrate, M.Sc. thesis, Middle East Technical University, 2013.

[46] S. Gall, C. Becker, E. Conrad, P. Dogan, F. Fenske, B. Gorka, K.Y. Lee, B. Rau, F. Ruske, B. Rech, Polycrystalline silicon thin-film solar cells on glass, Sol. Energy Mater. Sol. Cells. 93 (2009) 1004–1008. doi:10.1016/j.solmat.2008.11.029.

[47] M. Karaman, M. Aydın, S.H. Sedani, K. Ertürk, R. Turan, Low temperature crystallization of amorphous silicon by gold nanoparticle, Microelectron. Eng. 108 (2013) 112–115. doi:10.1016/j.mee.2013.02.075.

[48] A. Tankut, M. Karaman, E. Ozkol, S. Canli, R. Turan, Structural properties of a-Si films and their effect on aluminum induced crystallization, AIP Adv. 5 (2015) 1–7. doi:10.1063/1.4933193.

[49] A.A.D.T. Adikaari, S.R.P. Silva, Thickness dependence of properties of excimer laser crystallized nano-polycrystalline silicon, J. Appl. Phys. 97 (2005). doi:10.1063/1.1898444.

[40] R. Song, Y. Liu, Z. Cao, Effect of aluminum supply on aluminum-induced crystallization of amorphous silicon at low temperature, Phys. Status Solidi Curr. Top. Solid State Phys. 6 (2009) 663–668. doi:10.1002/pssc.200880707.

[51] Y. Mishima, T. Yagishita, Investigation of the bubble formation mechanism in a-Si:H films by Fourier-transform infrared microspectroscopy, J. Appl. Phys. 64 (1986) 3972–3974. doi:10.1063/1.341355.

[52] H.-Y. Kim, J.-B. Choi, J.-Y. Lee, Effects of silicon–hydrogen bond characteristics on the crystallization of hydrogenated amorphous silicon films prepared by plasma enhanced chemical vapor deposition, J. Vac. Sci. Technol. A Vacuum, Surfaces, Film. 17 (1999) 3240–3245. doi:10.1116/1.582049.

[53] S.T. Takenaka, M. Kunii, H. Oka, H. Kurihara, High mobility poly si thin film transistors using solid phase crystallized a si films deposited by plasma-enhanced chemical vapor deposition, Jpn. J. Appl. Phys. 29 (1990) 2380–2383. doi:10.1143/JJAP.29.L2380.

[54] N. Fukata, S. Fukuda, S. Sato, K. Ishioka, M. Kitajima, S. Hishita, K. Murakami, Hydrogen-boron complexes in heavily boron-doped silicon treated with high concentration of hydrogen atoms, Phys. B Condens. Matter. 376–377 (2006) 85–88. doi:10.1016/j.physb.2005.12.023.

[55] L. Csepregi, E.F. Kennedy, T.J. Gallagher, J.W. Mayer, T.W. Sigmon, Reordering of amorphous layers of Si implanted with31P,75As, and11B ions, J. Appl. Phys. 48 (1977) 4234–4240. doi:10.1063/1.323408.

[56] A. Lietoila, A. Wakita, T.W. Sigmon, J.F. Gibbons, Epitaxial regrowth of intrinsic,31P-doped and compensated (31P+11B-doped) amorphous Si, J. Appl. Phys. 53 (1982) 4399–4405. doi:10.1063/1.331222.

[57] B.C. Johnson, J.C. McCallum, Dopant-enhanced solid-phase epitaxy in buried amorphous silicon layers, Phys. Rev. B. 76 (2007) 045216. doi:10.1103/PhysRevB.76.045216.

[58] Olson G.L. and Roth J.A., Kinetics of solid phase crystallization in amorphous silicon, Mater. Sci. Reports. 3 (1988) 1–77.

[59] W.E. Hong, J.S. Ro, Kinetics of solid phase crystallization of amorphous silicon analyzed by Raman spectroscopy, J. Appl. Phys. 114 (2013) 073511. doi:10.1063/1.4818949.

[60] B.G. Svensson, M.K. Linnarsson, B. Mohadjeri, M. Petravić, J.S. Williams, SIMS and depth profiling of semiconductor structures, Nucl. Inst. Methods Phys. Res. B. 85 (1994) 363–369. doi:10.1016/0168-583X(94)95845-9.

[61] K. Juraić, D. Gracin, I. Djerdj, A. Lausi, M. Čeh, D. Balzar, Structural analysis of amorphous-nanocrystalline silicon thin films by grazing incidence X-ray diffraction, Nucl. Instruments Methods Phys. Res. Sect. B Beam Interact. with Mater. Atoms. 284 (2012) 78–82. doi:10.1016/j.nimb.2011.07.018.

[62] T. Ulyanenkova, M. Myronov, A. Ulyanenkov, Boron doped cubic silicon probed by high resolution X-ray diffraction, Phys. Status Solidi Curr. Top. Solid State Phys. 12 (2015) 255–258. doi:10.1002/pssc.201400102.

[63] M.J. Caturla, M.D. Johnson, T. Diaz De La Rubia, The fraction of substitutional boron in silicon during ion implantation and thermal annealing, Appl. Phys. Lett. 72 (1998) 2736–2738. doi:10.1063/1.121075.

[64] K. Tsutsui, T. Matsuda, M. Watanabe, C.G. Jin, Y. Sasaki, B. Mizuno, E. Ikenaga, K. Kakushima, P. Ahmet, T. Maruizumi, H. Nohira, T. Hattori, H. Iwai, Activated boron and its concentration profiles in heavily doped Si studied by soft x-ray photoelectron spectroscopy and Hall measurements, J. Appl. Phys. 104 (2008) 093709. doi:10.1063/1.3014033.

[65] X.J. Hao, E.C. Cho, C. Flynn, Y.S. Shen, S.C. Park, G. Conibeer, M.A. Green, Synthesis and characterization of boron-doped Si quantum dots for all-Si

quantum dot tandem solar cells, Sol. Energy Mater. Sol. Cells. 93 (2009) 273–279. doi:10.1016/j.solmat.2008.10.017.

[66] J.M. Westra, R.A.C.M.M. van Swaaij, P. Šutta, K. Sharma, M. Creatore, M. Zeman, Study of the effect of boron doping on the solid phase crystallisation of hydrogenated amorphous silicon films, Thin Solid Films. 568 (2014) 38–43. doi:10.1016/j.tsf.2014.07.040.

[67] M. Karaman, Ö. Tüzün Özmen, S.H. Sedani, E. Özkol, R. Turan, Effects of glass substrate coated by different-content buffer layer on the quality of poly-Si thin films, Phys. Status Solidi Appl. Mater. Sci. 213 (2016) 3142–3149. doi:10.1002/pssa.201600197.

[68] A. Michael, A. Kazuo, Y.W. Xu, C.Y. Kwok, T. Puzzer, S. Varlamov, Characterization of UHV E-beam evaporated low-stress thick silicon film for MEMS application, Procedia Eng. 47 (2012) 690–693. doi:10.1016/j.proeng.2012.09.241.

[69] C.H. Chao, K.W. Weng, H.L. Cheng, C.H. Chan, S.Y. Lien, Boron induced recrystallization of amorphous silicon film by a rapid thermal process, Thin Solid Films. 518 (2010) 7480–7482. doi:10.1016/j.tsf.2010.05.028.

[70] R. Bisaro, J. Magario, K. Zellama, S. Squelard, P. Germain, J.F. Morhange, Solid-phase crystallization kinetics in doped a-Si chemical-vapor-deposition films, Phys. Rev. B. 31 (1985) 3568–3575. DOI: 10.1103/PhysRevB.31.3568.

[71] I. DeWolf, Raman Spectroscopy: About Chips and Stress, Spectrosc. Eur. 15 (2003) 6–13.

[72] A. Kumar, F. Law, G.K. Dalapati, G.S. Subramanian, P.I. Widenborg, H.R. Tan, A.G. Aberle, Synthesis and characterization of large-grain solid-phase crystallized polycrystalline silicon thin films, J. Vac. Sci. Technol. A Vacuum, Surfaces, Film. 32 (2014) 061509. doi:10.1116/1.4897298.

[73] T. Kaneko, K. Onisawa, M. Wakagi, Y. Kita, T. Minemura, Crystalline Fraction of Microcrystalline Silicon Films Prepared by Plasma-Enhanced Chemical Vapor Deposition Using Pulsed Silane Flow, Jpn. J. Appl. Phys. 32 (1993) 4907–4911. doi:10.1143/JJAP.32.4907.

[74] J. Yamauchi, Y. Yoshimoto, Y. Suwa, X-ray photoelectron spectroscopy analysis of boron defects in silicon crystal: A first-principles study, J. Appl. Phys. 119 (2016). doi:10.1063/1.4948572.

[75] A. Moldovan, F. Feldmann, G. Krugel, M. Zimmer, J. Rentsch, M. Hermle, A Roth Folsch, ¨ K. Kaufmann, C. Hagendorf, Simple cleaning and conditioning of silicon surfaces with UV/ozone sources, in: Proceedings of the 4th International Conference on Silicon Photovoltaics, SiliconPV 2014,

Energy Procedia 55, 2014, pp. 834–844, https://doi.org/10.1016/j.egypro.2014.08.067.

[76] B. Steinhauser, J.I. Polzin, F. Feldmann, M. Hermle, S.W. Glunz, Excellent surface passivation quality on crystalline silicon using industrial-scale direct-plasma TOPCon deposition technology, Sol. RRL (2018), 1800068, https://doi.org/10.1002/solr.201800068

[77] J.I Polzin, F. Feldmann, B. Steinhauser, M. Hermle, S. Glunz, Realization of TOPCon using industrial scale PECVD equipment, in: Proceedings of the AIP Conference Proceedings1999, 2018, 040018, https://doi.org/10.1063/1.5049281

[78] D. Yan, A. Cuevas, S.P. Phang, Y. Wan, D. Macdonald, 23% efficient p-type crystalline silicon solar cells with hole-selective passivating contacts based on physical vapor deposition of doped silicon films, Appl. Phys. Lett. 113 (6) (2018), 061603, https://doi.org/10.1063/1.5037610.

[79] L. Nasebandt, S. Hübner, B. Min, C. Hollemann, T. Dippell, P. Wohlfart, R. Peibst, R Brendel, Fired-only passivating poly-Si on oxide contacts with dc-sputtered insitu phosphorous-doped silicon layers", in: Proceedings of the 37th European Photovoltaic Solar Energy Conference and Exhibition, 2020, pp. 184–187.

[80] S. Masuda, K. Gotoh, I. Takahashi, K. Nakamura, Y. Ohshita, N. Usami, Impact of boron incorporation on properties of silicon solar cells employing p-type polycrystalline silicon grown by aluminum-induced crystallization, Jpn. J. Appl. Phys. 57 (2018), https://doi.org/10.7567/JJAP.57.08RB12, 08RB12.

[81] G.C. Wilkes, A.D. Upadhyaya, A. Rohatgi, M.C. Gupta, Laser crystallization and dopant activation of a-Si:H carrier-selective layer in TOPCon Si solar cells, IEEE J. Photovolt. 10 (5) (2020) 1283–1289, https://doi.org/10.1109/JPHOTOV.2020.3006273.

[82] Q. Li, K. Tao, Y. Sun, R. Jia, S.M. Wang, Z. Jin, X.Y. Liu, Replacing the amorphous silicon thin layer with microcrystalline silicon thin layer in TOPCon solar cells, Solar Energy 135 (2016) 487–492, https://doi.org/10.1016/j. solener.2016.06.012.

[83] F. Feldmann, M. Bivour, C. Reichel, H. Steinkemper, M. Hermle, S.W. Glunz, Tunnel oxide passivated contacts as an alternative to partial rear contacts, Solar Energy Mater. Solar Cells 131 (2014) 46–50, https://doi.org/10.1016/j. solmat.2014.06.015.

[84] A. Rohatgi, B. Rounsaville, Y.W. Ok, A.M. Tam, F. Zimbardi, A.D. Upadhyaya, Y. Tao, K. Madani, A. Richter, J. Benick, M. Hermle, Fabrication and modeling of high-efficiency front junction N-type silicon solar cells with tunnel oxide passivating back contact, IEEE J. Photovolt. 7 (5) (2017) 1236–1243, https://doi. org/10.1109/JPHOTOV.2017.2715720.

[85] D.K. Ghosh, S. Bose, G. Das, S. Acharyya, A. Nandi, S. Mukhopadhyay, A. Sengupta, Fundamentals, present status and future perspective of TOPCon solar cells: A comprehensive review, Surfaces and Interfaces. 30 (2022), 101917, https://doi.org/10.1016/j.surfin.2022.101917.

[86] M. Fehr, P. Simon, T. Sontheimer, C. Leendertz, B. Gorka, A. Schnegg, B. Rech, and K. Lips, “Influence of deep defects on device performance of thin-film poly-crystalline silicon solar cells”, Applied Physics Letters, vol.101, pp. 123904, 2012.

CURRICULUM VITAE

Surname, Name: Sedani, Salar Habibpur

EDUCATION

Degree	**Institution**	**Year of Graduation**
MS	METU Science and Technology Policy Studies	2019
MS	METU Micro and Nanotechnology	2013
BS	Urmia University Solid-state Physics	2009
High School	NODET Oroumieh Branch, Oroumieh	2003

FOREIGN LANGUAGES

Advanced English, Turkish, Persian, Azerbayjani Beginner French, Arabic, German

PUBLICATIONS

1. Donercark E., Sedani S.H., Kabaçelik I, Salimi A., Turan R." Interface and material properties of wide band gap a-SiCx: H thin films for solar cell applications", Renewable Energy, 183, 781-790 (2022)

2. Sedani S.H., Yasar O.F., Karaman M., Turan R,. " Effects of boron doping on solid phase crystallization of in situ doped amorphous Silicon thin films prepared by electron beam evaporation", Thin Solid Films 694, 137639 (2020)

3. Ozmen O.T., Karaman M., Sedani S.H., Sagban H.M., Turan R,. " Solid phase epitaxial thickening of boron and phosphorus doped polycrystalline silicon thin films formed by aluminium induced crystallization technique on glass substrate", Thin Solid Films 689, 137451 (2019)

4. Ozmen O.T., Sedani S.H., Karaman M., Goksen K., Turan R,. " Farklı üretim parametrelerinin katı faz kristalizasyon (SPC) tekniği kullanılarak üretilen polikristal silisyum ince filmlerin kalitesi üzerine etkileri", Politeknik Dergisi 22 (2), 469-475 (2019)

5. Karaman M., Ozmen O.T., Sedani S.H., Ozkol E., Turan R,. " Effects of glass substrate coated by different-content buffer layer on the quality of poly-Si thin films", physica status solidi (a) 213 (12), 3142-3149 (2016)

6.Gunduz D.C., Tankut A., Sedani S.H., Karaman M., Turan R,. " Crystallization and phase separation mechanism of silicon oxide thin films fabricated via e-beam evaporation of silicon monoxide", TÜBİTAK DOĞA Dergisi, 12(3), 121-125 (2015)

7. Karaman M., Aydin M., Sedani S.H., Erturk K., Turan R,. " Low temperature crystallization of amorphous silicon by gold nanoparticle", Microelectronic engineering 108, 112-115 (2013)

Swimming, Cycling, Playing Violin and Accordion, Road trip